Design and Optimization of Effective Segmented Thermoelectric Generator for Waste Heat Recovery

Pham, Hoang Ngan

Publication date:
2015

Document Version
Publisher's PDF, also known as Version of record

Design and Optimization of Effective Segmented Thermoelectric Generator for Waste Heat Recovery

Ph.D. Thesis

by

Phạm Hoàng Ngân

Principle Supervisor: Prof. Nini Pryds

Co-supervisors: Dr. Ngô Văn Nông

Prof. Søren Linderoth

Department of Energy Conversion and Storage

Technical University of Denmark

Roskilde, Denmark

July 2015

Abstract

Energy safety is a vital issue of the global future. Together with developing renewable and eco-friendly energy sources, recovering waste energy is no less of an important issue. It is estimated that 60% of energy converted in most of today's energy processes nowadays is waste, mainly in the form of heat. Using thermoelectric generators, which convert heat into electricity, is a promising way to recover waste energy. However, the efficiency of thermal-to-electricity converters needs to be improved in order to be widely applied in practice. Despite the fact that significant amount of efforts have been focused on material development, realizing high efficient thermoelectric generators from such well-developed materials is still limited. Moreover, no single thermoelectric material could withstand the wide temperature range required to boost efficiency of TEGs. By segmentation of different TE materials which operate optimally in each temperature range, this study aims at developing high performance segmented TEGs for medium-high (450 – 850 K) temperature application. The research is focused on the challenges in joining and minimizing the contact resistances between different TE materials and with metal electrode.

One-dimensional numerical modeling was employed to design and predict the efficiency of segmented materials built up from most of today's state-of-the-art thermoelectric materials. Combinations of materials that would deliver the highest conversion efficiency in different temperature ranges of 300 – 700, and 900 – 1100 K are considered. The obtained results reveals that segmented thermoelectric generator comprising of $Bi_{0.6}Sb_{1.4}Te_3$/$Ba_8Au_{5.3}Ge_{40.7}$/PbTe-SrTe/SiGe as *p*-leg and either segmented Bi_2Te_3/PbTe/SiGe or Bi_2Te_3/$Ba_{0.08}La_{0.05}Yb_{0.04}Co_4Sb_{12}$/$La_3Te_4$ as *n*-leg working in 300 – 1100 K temperature range could achieve a maximum efficiency of 18.2 %. In lower working temperature ranges of 300 – 700 and 300 – 900 K, the maximum efficiencies are 13.5 and 16.6 %, respectively for segmented TEGs of *p*-leg$Bi_{0.6}Sb_{1.4}Te_3$/TAGS ($(AgSbTe)_{0.15}(GeTe)_{0.85}$) with *n*-leg Bi_2Te_3/PbTe and *p*-leg $Bi_{0.6}Sb_{1.4}Te_3$/$Ba_8Au_{5.3}Ge_{40.7}$/PbTe-SrTe with *n*-leg Bi_2Te_3/PbTe/SiGe. The results could provide a guideline to develop high efficiency segmented thermoelectric generators. Based on these theoretical results, segmentation of half-Heusler alloys and Bi_2Te_3 materials was selected for further study.

Firstly, the joining between thermoelectric *p*- and *n*-type half-Heusler (HH) alloys and silver electrode at hot side was developed. A fast-hot pressing method was introduced to directly join the HH materials with silver interconnecting layer. The method was also compared with the conventional joining method where a third material is used as filler. Microstructures and interfacial chemical evolution at the joining interfaces were investigated using scanning electron microscopy (SEM) and energy dispersive spectroscopy (EDS). The transport properties of the joint, including thermopower across the interfaces and contact resistance as a function of temperature were studied. With fast hot pressing method, the contact resistance between HH alloys and Ag-electrode could be

significantly reduced by about 50 %. Moreover, by avoiding a third filler material, the method limits the formation of new phases at contact interface which might degrade the overall thermoelectric properties. This work is a crucial step to make segmented HH/BiTe TEG.

Then, *p*- and *n*- type segmented legs of bismuth tellurides and half-Heusler alloys were built and characterized. Segmentation of bismuth tellurides to half-Heusler/Ag was processed at temperature 493 K, pressure 30 MPa in vacuum using $Ag_{10}Sn_{90}$ solder as filler. Interface microstructural evolution and thermoelectric properties of segmented legs were then investigated. The contact resistance of the join parts as a function of temperature was measured from room temperature to 473 K. Numerical modeling was used to evaluate the influence of measured contact resistances on the final power generating properties of the obtained segmented legs and their unicouple. Under working temperature from 323 to 873 K, the obtained *p*-segmented legs could deliver a power density of 0.3 Wcm^{-2} and maximum voltage of 115 mV. With the same condition, the power density and maximum voltage generated by *n*-segmented leg were 0.25 Wcm^{-2} and 102 mV. These values are significantly smaller than calculation data. The reason is possibly due to the contact between BiTe and electrode at the cold end, thus improvement of the cold side contact was made. At temperature gradient of 498 K, the maximum power density of the improved *n*-segmented leg was 0.8 Wcm^{-2}, giving a maximum efficiency of 4.5%.

Referat (abstract in Danish)

Energisikkerhed er et afgørende problem i den globale fremtid. Sammen med udviklingen af vedvarende og miljøvenlige energikilder er genvindingen af overskudsenergi ikke et mindre vigtigt spørgsmål. Estimeringer viser, at 60 % af den energi, der omdannes i de fleste energiprocesser i dag, er spildt hovedsagelig i form af varme. Termoelektriske generatorer, som omdanner varme til elektricitet, er en lovende teknologi til at genvinde denne overskudsenergi. Effektiviteten af teknologier til at omdanne varme til elektricitet skal dog forbedres for at blive almindeligt anvendt i praksis. På trods af at en betydelig mængde forskning har været fokuseret på at udvikle materialer, er realiseringen af højeffektive termoelektriske generatorer fra sådanne materialer stadig begrænset. Desuden har ingen enkelte termoelektriske materialer endnu formået at fungere optimalt i det brede temperaturområde, der kræves for at øge effektiviteten af termoelektriske generatorer. Ved at segmentere forskellige termoelektriske materialer, der opererer optimalt i hvert sit temperaturområde, sigter dette studie på at udvikle højt-ydende, segmenterede termoelektriske generatorer til anvendelser ved medium til høje temperaturer (450 – 850 K). Forskningen er fokuseret på udfordringerne i at sammenføje og minimere kontaktmodstanden mellem forskellige termoelektriske materialer og mellem en metalelektrode og termoelektriske materialer.

En 1-dimensional numerisk model er blevet anvendt til at designe og forudsige effektiviteten af segmenterede termoelektriske generatorer, der er opbygget af de bedste termoelektriske materialer. Her betragtes kombinationer af materialer, som vil levere den højeste effektivitet i temperaturintervallerne 300 – 700 K og 900 – 1100 K. Resultaterne viser, at segmenterede termoelektrisk generatorer bestående af $Bi_{0.6}Sb_{1.4}Te_3/Ba_8Au_{5.3}Ge_{40.7}$/PbTe-SrTe/SiGe som *p*-type ben og enten segmenteret Bi_2Te_3/PbTe/SiGe eller $Bi_2Te_3/Ba_{0.08}La_{0.05}Yb_{0.04}Co_4Sb_{12}/La_3Te_4$ som *n*-type ben kan opnå en maksimal effektivitet på 18.2 % i en temperaturgradient fra 300 K til 1100 K. Ved lavere temperaturer på 300 – 700 og 300 – 900 K er de maksimale effektiviteter 13.5 og 16.6 % fra henholdsvis segmenterede termoelektriske generatorer af *p*-benet $Bi_{0.6}Sb_{1.4}Te_3$/TAGS $((AgSbTe)_{0.15}(GeTe)_{0.85})$ kombineret med *n*-benet Bi_2Te_3/PbTe og *p*-benet $Bi_{0.6}Sb_{1.4}Te_3/Ba_8Au_{5.3}Ge_{40.7}$/PbTe-SrTe sammen med *n*-benet Bi_2Te_3/PbTe/SiGe. Resultaterne giver en rettesnor for at udvikle højeffektive, segmenterede termoelektriske generatorer. Baseret på disse teoretiske resultater blev segmenteringen af halv-Heusler legeringer og Bi_2Te_3 materialer udvalgt for de videre studier.

Først blev sammenføjning mellem termoelektrisk *p*- og *n*-type halv-Heusler (HH) legeringer og elektroder af sølv udviklet til den varme side af den termoelektriske generator. Hurtig varmpresning blev introduceret til at sammenføje HH materialerne direkte med sølvelektroderne. Metoden blev

sammenlignet med konventionelle metoder, hvor et tredje materiale anvendes til at sammenføje de to materialer. Mikrostrukturen og den kemiske opbygning på tværs af grænsefladerne blev undersøgt med scanningselektronmikroskopi (SEM) og energispredning-spektroskopi (EDS). Transportegenskaberne af de sammenføjede materialer, herunder termopoweren og kontaktmodstanden over grænsefladerne, blev undersøgt som funktion af temperaturen. Ved hjælp af varmpresningen kunne kontaktmodstanden mellem HH legeringerne og sølvelektroden reduceres betydeligt med ca. 50%. Ved desuden at undgå et tredje fyldmateriale begrænses dannelsen af nye faser ved kontaktfladen, som kan degradere de samlede termoelektriske egenskaber. Dette arbejde er et afgørende skridt mod at segmentere HH/BiTe termoelektriske generatorer.

Efterfølgende blev *p*- og *n*-type segmenteret ben af BiTe og halv-Heusler legeringer bygget og karakteriseret. Segmentering af BiTe med halv-Heusler/sølv blev skabt ved en temperatur på 493 K med et tryk på 30 MPa i vakuum ved anvendelse af $Ag_{10}Sn_{90}$ loddemetal som fyldstof. Mikrostrukturen og de termoelektriske egenskaber af de segmenterede ben blev derefter undersøgt. Kontaktmodstanden af de sammenføjede dele blev målt som funktion af temperaturen fra stuetemperatur til 473 K. Numerisk modellering blev anvendt til at vurdere indflydelsen af de målte kontaktmodstande på de effektproducerende egenskaber af både segmenterede ben og unikoblere dannet af disse ben. Ved temperaturer mellem 323 og 873 K kunne de *p*-segmenterede ben levere en effekttæthed på 0.3 Wcm^{-2} og en maksimal spænding på 115 mV. Under de samme betingelser gav det *n*-segmenterede ben en effekttæthed og maksimal spænding på 0.25 Wcm^{-2} og 102 mV. Disse værdier er signifikant mindre end de beregnede data. Årsagen er formentlig kontakten mellem BiTe og elektroden på den kolde side, og denne blev derfor forbedret. Ved at påtrykke en temperaturgradient på 498 K blev den maksimale effekttæthed for det forbedrede *n*-segmenteret ben 0.8 Wcm^{-2}, hvilket giver en maksimal virkningsgrad på 4.5%.

Acknowledgement

These last three years of being a PhD student in my group have been challenging, enriching and have broadened my world perspective. My supervisors Professor Nini Pryds, Doctor Ngo Van Nong and Professor Søren Linderoth have made the completion of this dissertation possible. They have supported me not only in my work but also in my life in Denmark being so many miles from my home and country. Nini is a great advisor, who always energized me with his truly dynamic working spirit. I have been impressed by his curiosity for knowledge, the way he brings up questions and from this I have learned how to study a scientific problem to the very basic of it. Nong is more than a supervisor. He gave me very insightful discussions, valuable advice and support when I needed help in my work. I have learned a lot from his strong background on material science and expertise on thermoelectrics. I have been inspired by his tremendous love for work. His commitment to the highest scientific standards gave me more challenges and was a motivation for me to always try harder. He is sometimes like my brother. I am greatly grateful to his advisorship and friendship. I thank Søren for bringing new viewpoint and perspectives for us when we dealt with a research problem. His advice and comments were always valuable and interesting guideline.

For the work in Chapter 3, the authors acknowledge the support from Copenhagen Cleantech Cluster in the project 48062 X-CCC and the OTE Power Project.

Regarding the work in Chapter 4, the authors thank the support from Copenhagen Cleantech Cluster (in the project 48062 X-CCC) and the Programme Commisssion on Energy and Environment (EnMi), which is part of the Danish Council for Strategic Research (Contract No. 10-093971), for sponsoring the research of the OTE-Power Project. We thank Professor Bo Brummerstedt Iversen for provding us access to the potentional Seebeck microprobe Panco, which is sponsored by Danish National Research Foundation (DNRF93). Benjamin Balke gratefully acknowledges the financial support by the DFG Priority Program 1386 “Nanostructured Thermoelectric Materials” under proposal BA 4171/2-2.

In regards to the numerical calculation model, I appreciate the help from Ali Sarhadi and Rasmus Bjørk.

I am indebted to Kurt Engelbrecht, Dennis Valbjørn Christensen and my friend Rick Jory for helping me with checking English in the thesis. Many thanks to Kurt for spending his time for me regardless of him being busy. I am grateful to Dennis and Rick for their encouragements and for always saying yes when I needed their help.

I would like to deeply acknowledge Le Thanh Hung, who has helped me considerably with his experience and skills in laboratory work. I admire his extremely hard working life style and his strong attitude at work. Having a chance to work with him is a great opportunity.

I would like to thank Li Han for his kind accompany and advice throughout my work and my study. He has always available for my questions and concerns, cheering me up and giving me encouragement. He is a great colleague.

I greatly appreciate the time spent with all the past and present members of our Thermoelectric group (NingYu Wu, Tim Holgate, Ali Sarhadi, Rasmus Bjørk, Kaspar Kristen Nielsen, and so on) for their good collaboration, fruitful discussions and moreover, their great friendship.

I am sincerely grateful to all the helpful and friendly technicians at the Department of Energy Conversion and Storage: Jørgen Geyti, Ebtisam Adellahi, Gitte Christiansen, Mike Wichmann, Lars Lorentzen and many many more people for helping me set up experiments, process my samples, train me on how to use laboratory equipments or simply giving me smiles and friendly discussion.

The thesis also could not be able to be completed without the help from my good friends Vu Thi Thuy Minh and Nguyen Dinh Khuong, who provided me a family-like living atmosphere during the last month of my thesis. I thank their little daughter Minh Ngoc for always giving me laughs and joyful childlike moments. I am also truly blessed to know Nong's family, Hung's family and all of my other Vietnamese friends. They are indeed thoughtful and caring people.

I am grateful to Johannes Steen Bang's family for giving me and my family exceptional love, care and encouragement. I always remember the loving and cozy atmosphere we all have had together.

I also thank my close friends Dieu Thu, Ha Le, Dung, Bich, Binh Minh, Rick. They are not living in Denmark, but I know we always think of and are always there for each other, just like our old times spent together. Everything changes with time yet our friendship never does.

Above all, I am deeply appreciative of the eternal love and care from my parents. They are the reason for me to be able to overcome all of the hard times I have been through and to keep on going. I am so blessed to have my fiancé Tran Thien Tuan beside me. He has travelled half the world from Australia to Europe mainly for being with me and taking great care of me during my thesis writing. Always I remember the feeling when all my tiredness and hopelessness disappeared only by hearing voices from mommy, daddy, sister and him. Each of you are everything I have.

List of publications

Peer-review papers

1. ***Towards high efficiency segmented thermoelectric unicouples***, Pham Hoang Ngan, Dennis Valbjørn Christensen , Gerald Jeffrey Snyder, Le Thanh Hung, Søren Linderoth, Ngo Van Nong, and Nini Pryds, Physica status solidi (a), Volume 211, Issue 1, pages 9 – 17, January 2014.
2. ***On the challenges of reducing contact resistances in half-Heusler alloys-based thermoelectric generators***, Pham Hoang Ngan, Ngo Van Nong, Le Thanh Hung, Benjamin Balke, Li Han, Ellen Marie Jensen Hedegaard, Søren Linderoth, and Nini Pryds, Journal of Electronic materials, Volume 45, Issue 1, pages 594 - 601, January 2016.
3. ***Segmented thermoelectric oxide-based module***, Le Thanh Hung, Ngo Van Nong, G. Jeffrey Snyder, Benjamin Balke, Li Han, Rasmus Bjørk, Pham Hoang Ngan, Tim C. Holgate, Søren Linderoth, and Nini Pryds, Energy Technology (2014), DOI: 10.1002/ente.201500176.
4. ***Fabrication and characterization of n-type segmented leg of half-Heusler alloy and Bismuth telluride,*** Le Thanh Hung, Pham Hoang Ngan, Ngo Van Nong, and Nini Pryds, manuscript in preparation.

Conference papers

1. ***High-temperature Oxide Thermoelectric Modules with p-type $Ca_3Co_4O_9$*** and n-type Al-doped ZnO Legs, Le Thanh Hung, Ngo Van Nong, Pham Hoang Ngan, Dan Eriksen, Li Han, Søren Linderoth, and Nini Pryds, Presented at: 31st International & 10th European Conference on Thermoelectrics, 2012, Aalborg.
2. ***Fabrication and performance of high temperature segmented thermoelectric oxide-based module,*** Le Thanh Hung, Ngo Van Nong, Pham Hoang Ngan, Li Han, Tim Holgate, Søren Linderoth, and Nini Pryds, Proceedings of the 32nd International Conference on Thermoelectrics, 2013.
3. ***Preparation and characterization of segmented p-type $Ti_{0.3}Zr_{0.35}Hf_{0.35}CoSb_{0.8}Sn_{0.2}$/ $Ca_3Co_4O_9$***, Le Thanh Hung, Li Han, Eugen Stamate, Pham Hoang Ngan, Benjamin Balke, Søren Linderoth, Ngo Van Nong, and Nini Pryds, presented at: 2013 MRS Fall Meeting & Exhibit, 2013, Boston, MA
4. ***Characterization of the contact between Bi_2Te_3-based materials and lead-free solder alloy under thermal cycling***, Ngo Van Nong, Le Thanh Hung, Li Han, Hoang Ngan

Pham, and Nini Pryds, 34th International & 13th European Conference on Thermoelectrics, 2015, Dresden.

Table of Contents

List of Figures

List of Tables

List of Symbols

Symbol	Definition	Unit
A	Seebeck coefficient	μVK^{-1}
π	Peltier coefficient	V
β	Thomson coefficient	μVK^{-1}
ΔV	Generated voltage	V
ΔT	Applied temperature difference	K
q	Heat current	W
I	Electrical current	A
z	Figure of merit	K^{-1}
σ	Electrical conductivity	$\Omega^{-1}m^{-1}$
κ	Thermal conductivity	$Wm^{-1}K^{-1}$
ρ	Electrical resistivity	Ω
T_h	Hot side temperature	K
T_c	Cold side temperature	K
η	Energy conversion efficiency	%
V	Thermoelectric voltage	mV
I	Thermoelectric current	A
P	Thermoelectric power	W
P_{max},	Maximum power	W (or mW)
I_{max}	Maximum current	A
V_{max}	Maximum voltage	mV
R_c	Contact resistance	Ωm^2
R *or* R_{total}	Total resistance of TE element/TEG, is the total of resistance of TE material and contact resistance	Ω
R_{load}	External load resistance	Ω
A	Area	mm^2
$_n$ *(subsrcipt)*	*n*-type	-
$_p$ *(subsrcipt)*	*p*-type	-
L or l	Length	mm
d	diameter	mm
$I_{opt\text{-}material}$	Optimum electrical current of TE material	A
$I_{opt\text{-}segmented}$	Optimum electrical current of segmented TE element	A
Q	Heat flow in the system	W

Q_{in}, Q_{out}	Heat absorbed and rejected by a TEG	W
Q_{loss}	Heat loss	W
ΔQ	Amount of heat rejected/absorbed	W
u	Relative current density (or reduced current density)	V^{-1}
η_{TE}	Thermoelectric efficiency	%
$max\eta_{TE}$	Maximum efficiency	%
s	Compatibility factor	V^{-1}
ϕ	Thermoelectric voltage	V or mV
J	Current density	Acm^{-2}
$R_{measured}$	Measured resistance	Ω
ASR_C	Area specific contact resistance	Ωm^2
δ	Ratio between contact resistance to the total resistance	-

1. Chapter 1 - Introduction

In this chapter, a general introduction to thermoelectricity including the background of thermoelectric (TE) effects, overview on TE materials and TE generators (TEG) are presented. Issues regarding effective design of TEG and critical factors influencing TEG's performance are introduced. Then, an overview of energy status and the potentials of thermoelectricity are discussed. This chapter ends with the outline of the thesis.

1.1 Thermoelectric effects

Dating back to 1823, Thomas Johann Seebeck observed deflection of a compass needle when it was placed near to a setup that consisted of two connected dissimilar conductors and one of the connected ends was heated. He then related this effect to thermomagnetism. It was H.C. Ørsted, who suggested later that the nature of this effect was not thermomagnetic but rather involved a thermoelectric current [1]. This effect shows that on the application of a temperature gradient across two ends of a conductor (semiconductor or metal), a voltage is created. The generated voltage originates from the diffusion of the majority charge in the materials, i.e. electrons or holes, from the hot side to the cold side creating a potential difference [1]. If these are connected to an external load, there will be electrical current running in the system (Figure 1-1 a). The proportionality ratio between the voltage difference and the temperature difference is the Seebeck coefficient α, also called thermopower, defined by the amount of voltage gradient generated per one unit of temperature gradient.

$$\alpha = \frac{\Delta V}{\Delta T} \qquad (1.1)$$

(ΔV is the generated voltage and ΔT is the applied temperature difference.)

Later, in 1834, C. Peltier observed that when an electrical current was passed through two connected dissimilar materials, heat could be generated or removed at the junctions as shown in Figure 1-1 b. The energy carried by the charge depends on the Fermi levels of the contact materials. When electrons pass from one material to another material with a different Fermi energy level, they need to absorb/release energy. The energy absorbed/liberated is the difference between the two Fermi energies and is manifest itself in the form of heat [2], [3].

The Peltier effect can be described as the relation between the heat current q and the electrical current I, where the proportionality constant is Peltier coefficient π:

$$q = \pi I \qquad (1.2)$$

The third important effect in thermoelectricity was described by William Thompson (Lord Kelvin) in 1851. He found that the heat absorbed or liberated from a material is dependent on both the electric current and the temperature gradient across its two ends. The Thomson coefficient is described as: β, with $\beta = \frac{\Delta Q}{I \Delta T}$ [4]. (ΔQ is the amount of heat absorbed/rejected and I is the current.)

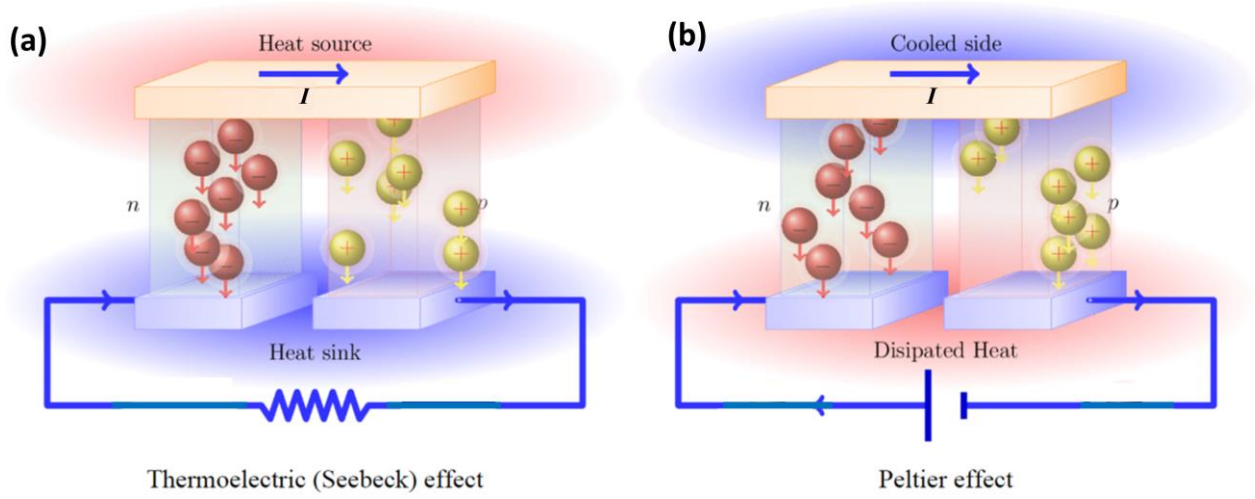

Figure 1-1 Basics of thermoelectrics: Seebeck effect (a) and Peltier effect (b) [5]

The units of the TE parameters are given in the List of Symbols.

1.2 Thermoelectric materials

1.2.1 Thermoelectric figure of merit

The performance of a TE material is evaluated by its Figure of Merit (z), defined as [1], [2], [6]:

$$z = \frac{\alpha^2 \sigma}{\kappa} \qquad (1.3)$$

Here, α is the Seebeck coefficient, σ is the electrical conductivity and κ is the thermal conductivity. A good TE material is expected to have high thermopower (Seebeck coefficient) to generate high electrical potential under thermal gradient, high electrical conductivity to facilitate the movement of electrical carriers and low thermal conductivity to maintain the temperature difference along the TE element. However, the Seebeck coefficient, electrical conductivity and thermal conductivity are all interdependent of each other, e.g. the electrical conductivity is proportional to thermal conductivity via the Wiedemann–Franz law [2], [6]. On the other hand, high electrical conductivity usually requires high carrier concentration and carrier mobility, which negatively affect the Seebeck coefficient [2], [6], [7]. For example, metals typically have electrical conductivity above 2500 Ω^{-}

$^{1}cm^{-1}$, but their thermal conductivities are also high, above 1.8 $Wm^{-1}K^{-1}$ and their Seebeck coefficients are typically lower than 10 μVK^{-1} [7]. The opposite situation exists for insulators, with Seebeck coefficients (> 300 μVK^{-1}) yet small electrical and thermal conductivities (< 0.2 $Wm^{-1}K^{-1}$) [7]. The compromise between these properties is optimum in the case of semiconductors. The optimization of z is complicated. However, based on detailed analysis of these thermoelectric properties, new ideas, e.g. nanostructuring, modifying energy band structure, etc. to independently modify α, σ and κ to obtain the optimized z are possible [7], [8]. Progress on the development of TE materials is given in the coming section.

1.2.2 Thermoelectric material development progress

The progress of developing and enhancing zT of TE materials is illustrated in Figure 1-2. Based on theoretical predictions to optimize zT, in the 1960s, Goldsmid et al. obtained thermoelectric bismuth tellurides with zT of 0.6 for *p*-type and 0.7 for *n*-type at 300 K [9]. Since then, many other types of materials with profound thermoelectric properties have been found and studied [10]. Success in enhancing the figure of merit zT above 1 for TE materials has been increasingly reported. Some typical TE materials attracting modern research are: lead tellurides alloys PbTe (zT = 1.5 at 773 K or 1.8 at 850 K) [11], [12], lead selenide alloys PbSe (zT = 1.5 at 642 K) [13], skutterudites (zT = 1.26 at 850 K [14] and 1.7 at 850 K [15]), half-Heuslers (zT = 1.2 at 983 K) [16]–[18], Zintl (zT = 1.2 at 1100 K) [19], [20] and silicon germanium SiGe (zT = 1.3 at 1173 K) alloys [21]. Nevertheless, besides the theoretical challenges to achieve high zT, practical challenges such as mechanical endurance and thermal stability of TE materials and TE devices are also major concerns to bring TE into practical applications [22].

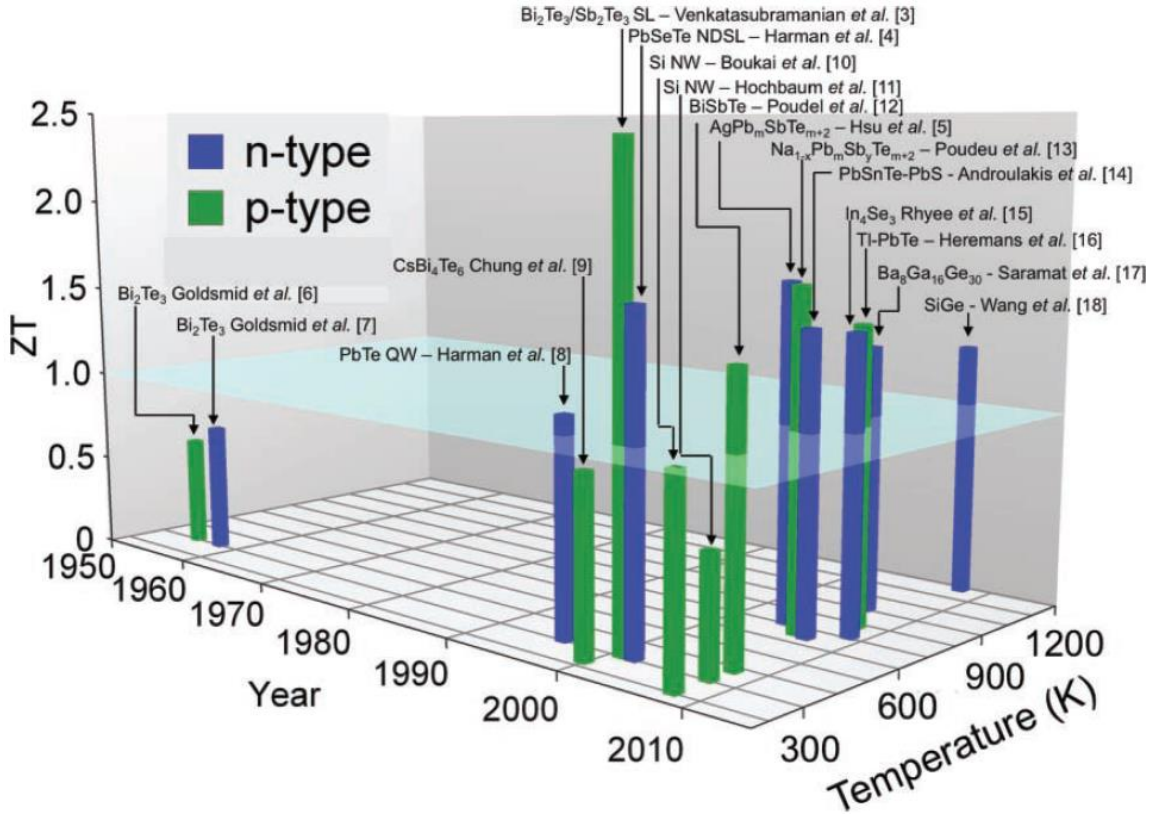

Figure 1-2 Development of TE materials: increase in varieties and figure of merits [10]

1.3 Thermoelectric generators

1.3.1 Basics of thermoelectric generators

A basic thermoelectric generator (TEG) contains a pair of *p*- and *n*-type thermoelements (or thermoelectric legs) connected electrically in series and thermally in parallel (Figure 1-3). The two elements are electrically connected usually through a conducting electrode. One end of the *p*- and *n*-type thermoelements is in contact with a heat source with temperature at T_h and the other end is exposed to a heat sink at temperature T_c. Under such a temperature gradient, the connected *p*- and *n*-type thermoelements generate electrical voltage, current and thus power when they are connected to an external load. In practice, multiple pairs of *p*- and *n*-legs are connected to increase the total outputs (Figure 1-3 b). Efficiency calculation of a TEG composed of multiple *p*-*n* pairs can be simplified to efficiently calculate of a single *p*-*n* pair. Assuming there is negligible heat loss and contact resistance, the thermoelectric outputs of a TEG can be calculated as the follows [1]:

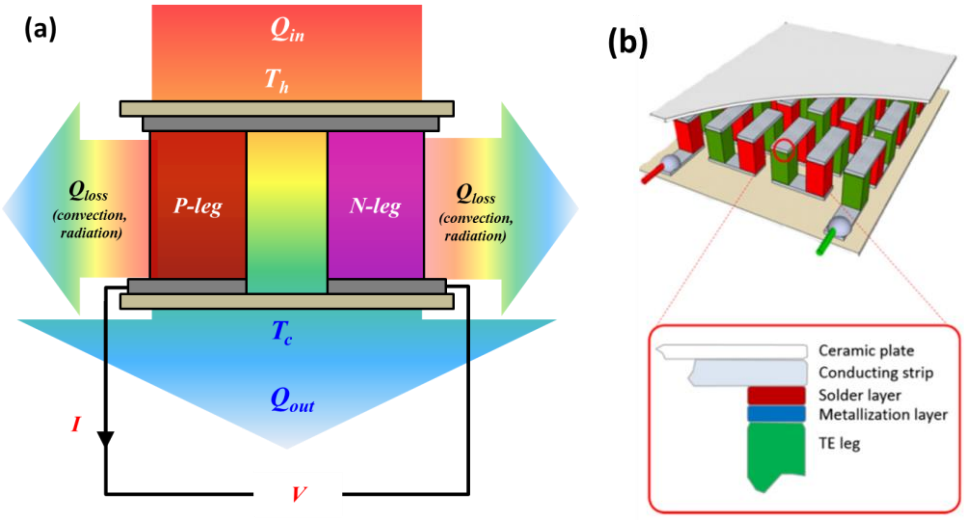

Figure 1-3 (**a**) Schematic principle of a TEG. (**b**) Schema of a typical TEG in practice [22].

The maximum energy conversion efficiency of the TEG is determined by its working temperature span and material performance:

$$\eta_{max} = \frac{T_h - T_c}{T_h} \frac{\sqrt{1+Z_M\bar{T}} - 1}{\sqrt{1+Z_M\bar{T}} + \frac{T_c}{T_h}} \qquad (1.4)$$

Where $\bar{T}$ is the average temperature: $\bar{T} = \frac{T_h - T_c}{2}$

With $\frac{T_h - T_c}{T_h}$ is Carnot efficiency η_c

Z_M is the average figure of merit of the TEG:

$$Z_M = \frac{(\alpha_p - \alpha_n)^2}{K.R} \qquad (1.5)$$

where K, α, and R: thermal conductance, thermopower and resistance of the TEG, respectively. Given that A is the total cross sectional area of p- (A_p) and n- (A_n) legs the values of K, R, and α are calculated as follows:

$$K = \kappa_p \frac{A_p}{l_p} + \kappa_n \frac{A_n}{l_n} \qquad (1.6)$$

$$R = \rho_p \frac{l_p}{A_p} + \rho_n \frac{l_n}{A_n} \qquad (1.7)$$

$$\alpha = |\alpha_p| + |\alpha_n| \qquad (1.8)$$

The TE voltage V, the current I and the power P generated are:

$$V = \alpha\, \Delta T \tag{1.9}$$

$$I = \frac{V}{R + R_{load}} \tag{1.10}$$

$$P = VI = \frac{(\alpha\, \Delta T)^2}{R + R_{load}} \tag{1.11}$$

It is worthwhile to note that in these calculations, the TE properties of the materials, which are often temperature-dependent, are averaged over the considered temperature range and therefore they are treated as temperature independent. This average approximation thus does not give results as accurate as when the temperature dependencies of TE materials are counted. Nevertheless, it is a good and robust procedure to evaluate the upper limit of the module performance. In order to have more precise calculation of expected TE outputs, a numerical model is used and is described in the Section 1.4.1 below.

1.3.2 Segmented and cascaded thermoelectric generators

From the definition of a TEG's efficiency (equation *1.4*), it is clear that the total conversion efficiency is determined not only by its figure of merit of the materials but also by its overall working temperature span. However, TE materials usually perform well only within a certain narrow temperature range. Thus, utilizing different TE materials whose optimum working temperature ranges are successively distributed increases the figure of merit of the whole TEG and is a promising direction. To realize the concept, two approaches have been developed: **segmentation** and **cascade**. The concepts of these approaches are illustrated in Figure 1-4. In the segmentation structure, each *p*- and *n*-leg is constructed from at least two different *p*- and *n*-materials. Materials in a leg are physically joined together electrically and thermally in series. In the cascaded structure (also called multistage structure), there are at least two TEGs that are stacked on top of each other. The TEGs are connected electrically in parallel and thermally in series. *p*- and *n*-legs of each TEG are made from single TE material.

A segmented leg requires that the compatibility between its constituent materials is matched to ensure the improvement of efficiency by segmentation. Details of how to develop an efficient combination are discussed in Section 1.4.1. As for the cascaded TEG, the efficiency is tremendously susceptible to the quality of connections between stages. The efficiency gained by cascading might easily be surpassed by the inter-stage thermal losses, which is difficult to control as it require a great deal of cautions during manufacturing. For instance, in order to guarantee good thermal contact, highly flat surfaces of substrates of each TE stage is required. Fabrication of a cascading system is far more complicated than that of a segmented system [6]. Thus, segmentation so far seems to be more preferred and thus is the focus of much TEG development research [23]–[30].

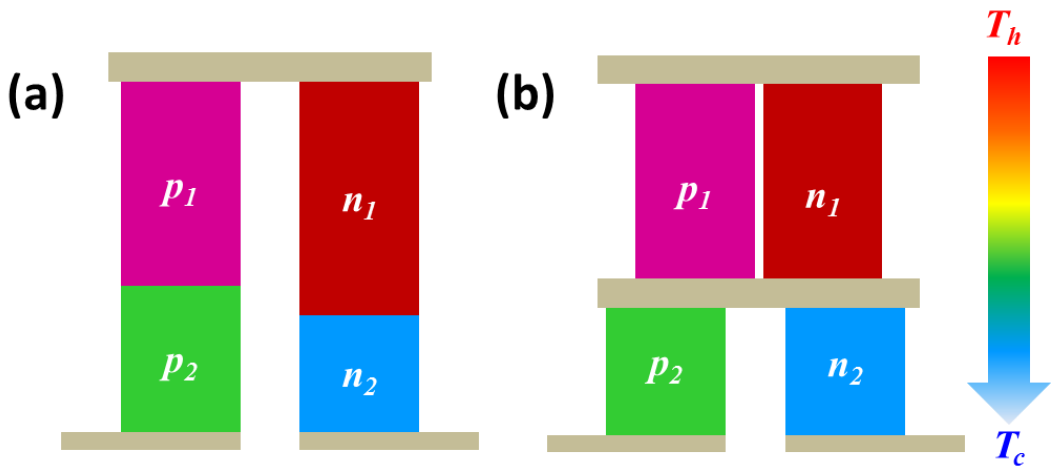

Figure 1-4 Schematic principles of typical segmented (**b**) and cascaded (**c**) TE generators. There can be more than 2 stages for each configuration.

1.4 Segmented TEG development

1.4.1 Segmented TEG design

The efficiency benefit rewards by segmentation of TE materials is critically dependent on material selection [6], [31]. Given a certain temperature gradient, the highest theoretical efficiency that determined by figure of merits zT of TE materials can only be achieved if the optimum electrical current of TE materials $I_{opt\text{-}material}$ are maintained during operation. Due to differences in electrical and thermal properties of the materials, $I_{opt\text{-}material}$ values of different materials are different. When they are connected together as a TE element, there is a current $I_{opt\text{-}segmented}$ that gives the highest efficiency for the whole segmented leg. $I_{opt\text{-}segmented}$ is often different from $I_{opt\text{-}material}$, means that the materials might not work with their highest potentials. When the discrepancy is significant, segmentation of materials could result in the decrease of the total efficiency compared to that of each TE material. Details of the calculations and examples are presented below.

To build efficient segmented legs, the selection of the TE materials has to be such that they are compatible with each other. The theory to find the optimum working conditions is known as the compatibility factor approach. Details of the model are provided in Chapter 9, *Thermoelectric Handbook: Macro to Nano* [6] by Jeffrey G. Snyder. The assumption of this model is that the system is thermally isolated i.e. no heat loss. Furthermore, influences of contact resistances are not included but can be integrated.

Consider a TE element composed of one material, working under power generation mode, with a temperature gradient created by temperature at the hot side T_h and that of the cold side T_c. The flows

of heat and electricity in the leg are governed by the heat equation and the law of energy conservation. For that reason, we have:

Electrical voltage *V* is determined by the Seebeck and Ohmic effects:

$$V = \alpha \nabla T - \rho T \tag{1.12}$$

The corresponding power, *P*, generated by the TE element:

$$P = VJ \tag{1.13}$$

where *J* is the electrical current density.

The heat flow in the system is the result of the Fourier law, and the heat produced by TE Peltier effect:

$$Q = \alpha T J + \kappa \nabla T \tag{1.14}$$

And the resulting heat equation is the combination of Thomson and Joule effects:

$$\nabla(\kappa \nabla T) = -T \frac{d\alpha}{dT} J \nabla T - \rho J^2 \tag{1.15}$$

To simplify the electrical and thermal effects, a variable, *u* (V^{-1}), is defined as the ratio of the current density and the heat flow:

$$u = \frac{J}{\kappa \nabla T} \tag{1.16}$$

Based on the definition of *u*, it is worthwhile to note that *u* is a function of both internal material properties *ρ, α* and *κ* and external applied conditions: temperature gradient and load resistance.

Substitute *u* into equations *1.13*, *1.14* and *1.15*, we obtain:

$$P = \kappa(\nabla T)^2 \times u(\alpha - u\rho\kappa) \quad (1.17)$$

$$Q = \kappa\nabla T(\alpha u T + 1) \quad (1.18)$$

$$And \ \nabla\left(\frac{J}{u}\right) = -T\frac{d\alpha}{dT}J\nabla T - \rho J^2 \quad (1.19)$$

$$Or \ \nabla\left(\frac{1}{u}\right) = -T\frac{d\alpha}{dT}\nabla T - \rho J \quad (1.20)$$

Assuming the heat flow in 1D, from the hot end to the cold end, *u* is also a function of distance *x* from the hot end (or the cold end) we obtain the following differential equation:

$$\nabla\left(\frac{1}{u}\right) = -\frac{1}{u^2}\frac{du}{dx} = -\frac{1}{u^2}\frac{du}{dT}\nabla T \quad (1.21)$$

The heat equation thus can be expressed as:

$$\frac{1}{u^2}\frac{du}{dT} = T\frac{d\alpha}{dT} + \rho u\kappa \quad (1.22)$$

which is equivalent to

$$\frac{du}{dT} = u^2 T\frac{d\alpha}{dT} + u^3\rho\kappa \quad (1.23)$$

The value of *u* can be found by solving equation *1.23*. However, this differential equation does not have an analytical solution. Thus, it requires solving the equation numerically to find *u*, or optimum condition to get the highest efficiency determined by *zT*.

The total energy conversion efficiency can be determined by the following relation:

$$\eta = \frac{Pdx}{Q} = \frac{P\,dT}{Q\,\nabla T} = \frac{dT}{T}\frac{u(\alpha - u\rho\kappa)}{u\alpha + \frac{1}{T}} \quad (1.24)$$

Note that $\frac{dT}{T}$ is the Carnot efficiency and the second fraction represents the efficiency which is dependent on the TE materials (similar to equation 1.4). For a given constant temperature span, maximizing the total efficiency is equivalent to maximizing the thermoelectric efficiency. The thermoelectric efficiency η_{TE} is termed the *reduced efficiency*. From the definition of the figure of merit, $z = \frac{\alpha^2}{\rho k}$, the reduced efficiency can be expressed as:

$$\eta_{TE} = \frac{u\alpha - u^2(\frac{\alpha^2}{z})}{u\alpha + \frac{1}{T}} = \frac{u\alpha\,(1-\frac{u\alpha}{z})}{u\alpha\,(1+\frac{1}{u\alpha T})} \quad (1.25)$$

$$\eta_{TE} = \frac{1-\frac{u\alpha}{z}}{1+\frac{1}{u\alpha T}} \quad (1.26)$$

Maximizing η_{TE} ($\frac{d\eta_{TE}}{du} = 0$)

$$\Leftrightarrow \frac{\alpha}{z}\left(1+\frac{1}{u\alpha T}\right) = \frac{1}{u^2\alpha T}\,(1-\frac{u\alpha}{z}) \quad (1.27)$$

$$\Leftrightarrow T(u\alpha)^2 + 2(u\alpha) - z = 0 \quad (1.28)$$

$$\Leftrightarrow u = \frac{\sqrt{1+zT}-1}{\alpha T} \quad (1.29)$$

The value of *u* that maximizes η_{TE} is called the compatibility factor *s*.

$$s = \frac{\sqrt{1+zT}-1}{\alpha T} \quad (1.30)$$

Inserting equation *1.29* into *1.26* gives the maximum efficiency η_{TE}:

$$max\,\eta_{TE} = \frac{\sqrt{1+zT}-1}{\sqrt{1+zT}+1} \quad (1.31)$$

In practice, *u* is an indirect and inclusive factor and represents:

- External factors: temperatures, electrical load and geometry (cross sectional area, length of the TE element)
- Internal factors: electrical resistivity, thermal conductivity and Seebeck coefficient of TE materials.

Meanwhile, *s* is merely dependent on the TE material's properties, i.e., the internal factors.

In a system where $u \neq s$, the obtained energy conversion efficiency is less than that could be given by the full potential of the TE material. The larger the difference between *u* and *s*, the less is η_{TE}. In a segmented system, *u* should be tuned in such a way that it is as close as possible to *s* for all the TE materials in the segment. The change of electrical current, equivalently, the relative current density *u* running in a working TE element, is usually less than the change of the materials' compatibility factors. Therefore, a primary condition to address the requirement is that the TE materials should possess as similar compatibility factors *s* as possible. This is shown in Figure 1-5. Given a segmented leg consists of two TE materials p/n_1 and p/n_2 with compatibility factors s_1 and

s_2, respectively. The optimization of relative current density u to maximize the total leg's efficiency should be done in a way that minimize the differences between u, s_1 and s_2 are optimized to maximize the total leg's efficiency. From the optimized u, the other TE output parameters then can be determined (Table 1-1).

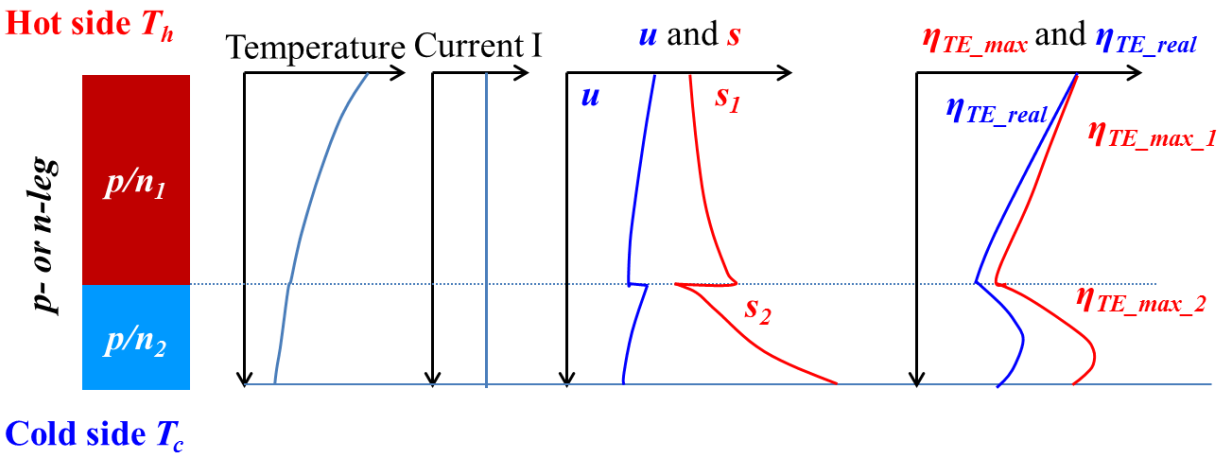

Figure 1-5 Compatibility approach applied on a segmented structure. The reduced current density is selected to optimize the efficiency of the segmented leg structure. The larger the difference between u and s, the larger the discrepancy between the obtained efficiency and the maximum efficiency given by zT. The larger the difference between s_1 and s_2, the less possible it is to utilize the best out of each TE material.

Table 1-1 Actual energy conversion efficiency and other TE output parameters of a segmented leg and unicouple determined by compatibility approach, with optimized working condition included

TE outputs	1 TE segmented leg	1 TE segmented unicouple
Efficiency	$\eta = 1 - \frac{\alpha_c T_c + \frac{1}{u_c}}{\alpha_h T_h + \frac{1}{u_h}}$	$\eta = 1 - \frac{\alpha_{p,c} T_c + \frac{1}{u_{p,c}} - \alpha_{n,c} T_c - \frac{1}{u_{n,c}}}{\alpha_{p,h} T_h + \frac{1}{u_{p,h}} - \alpha_{n,h} T_h - \frac{1}{u_{n,h}}}$
Voltage	$V = V_h - V_c =$ $V = \left(\alpha_h T_h + \frac{1}{u_h}\right) - (\alpha_c T_c + \frac{1}{u_c})$	$V = \Delta V_p - \Delta V_n =$ $\left[\left(\alpha_{p,h} T_h + \frac{1}{u_{p,h}}\right) - \left(\alpha_{p,c} T_c + \frac{1}{u_{p,c}}\right)\right] - \left[\left(\alpha_{n,h} T_h + \frac{1}{u_{n,h}}\right) - (\alpha_{n,c} T_c + \frac{1}{u_{n,c}})\right]$

Current	$I = JA$ $J = \frac{1}{l}\int_{T_c}^{T_h} ukdT$ l: length of the TE leg	$I = J_p A_p = -J_n A_n$ $J_{p,n} = \frac{1}{l}\int_{T_c}^{T_h} u_{p,n} k_{p,n} dT$ Given A_p or A_n, I then can be calculated.
Power density	$P = VI = \frac{1}{l} \times \Delta\phi \int_{T_c}^{T_h} kudT$	$P = I(V_p - V_n)$ $= \frac{1}{l} \times \left[\Delta\phi_p \int_{T_c}^{T_h} k_p u_p dT - \Delta\phi_n \int_{T_c}^{T_h} k_n u_n dT\right]$

With this model's concept, a segmented generator composed of one p-leg $Bi_{0.4}Te_{1.6}Te_3/Zn_4Sb_3/CeFe_4Sb_{14}$ and one *n*-leg $Bi_2Te_3/CoSb_3$ [32] has been demonstrated with a maximum efficiency of 15 %. The concept also laid the fundamental for further models that analyze TEG's operation and enhance TEG's efficiency based on material grading [33]–[36].

1.4.2 Segmented TEG fabrication

A common vital technical challenge for the fabrication of a non-segmented TEG is the contact resistance between TE materials and the electrodes. In the fabrication of a segmented TEG, besides the contact with the electrode, the creation of good contact between the TE materials is highly important. A good contact should address the following requirements:

- Good adhesion between materials.
- The contact resistance formed at the junction is as small as possible so that the electrical and thermal currents run in TEGs are not severely influenced [37] and consequently the overall efficiency is maintained.
- The bond between the materials is chemically stable under conditions that are similar to the operating condition in real applications. Inter-diffusion between adjacent materials that might cause detrimental change in TE properties of materials should be prohibited. Oxidation of materials used for joining is also an obstacle that needs to be circumvented.

In order to meet the quality standard, in each particular joining case, a process including the selection of joining methods and joining materials should be considered.

Joining methods

Materials with different chemical and physical properties require correspondingly different joining methods and procedures. In the typical cases of joining TE materials, it is critical that the processing temperature during joining is higher than the highest working temperature expected for the legs but lower than the melting / phase change temperature of the materials [38]. Depending on the particular case, a third material, also called filler material, might be used to make a good connection.

These are the two main joining concepts to join different materials: diffusion bonding and brazing or soldering.

- ***Diffusion bonding***

Diffusion bonding is a method to achieve bonds between two materials by facilitating their elements inter-diffusion into each other. The inter-diffusions occur due to the following conditions [38]–[40]:

(1) Adequate pressure to press the surfaces of the joining pieces (usually flat) together to ensure an intimately contact between them. The applied pressure should be high enough to form necessary localized deformations at the interface between the joining materials, yet not too high to inhibit possible deformation of the joining bulks.

(2) Elevated temperature at the joining area to assist the inter-diffusion of parent materials. Diffusion bonding usually requires high processing temperatures, usually up to 50 - 80% of the lowest melting temperature among the parent materials.

(3) Appropriate ambient atmosphere (such as inert gas, vacuum, etc.) to prevent undesired oxidation or reduction of material on the joining surface.

There are several hypotheses on the mechanism of diffusion bonding and the understanding of the method is still not fully established [41]. For example, one approach is “film hypothesis”. The hypothesis assumes that two clean surfaces when pressed together to the closeness in the range of atomic forces would tend to obtain the same properties by forming a strong bond at their contact surface. Thus, by bringing two surfaces close enough then pressing them to deform and disperse their surface contaminated layers, as a consequence expose necessary clean material layers, a strong bond can be formed. Another hypothesis is “re-crystallization”, which describes the bond formation as the relocation of atoms of joining materials at their interfaces when they are in atomic-scale proximity and under high temperature and pressure, the newly relocated atoms recrystallize and connect the parent materials [41]. Nevertheless, a general agreement is that two clean surfaces once

being brought together at the atomic closeness and under appropriate temperature would form bonds [39].

- ***Brazing / soldering***

Brazing and soldering is also a popular joining method where bonding is made by the melting of a third material inserted between the pieces needed to be joined. Processes requiring temperatures lower than 723 K is called soldering, while brazing refers to processes with temperature above 723 K [42], [43]. Brazing and soldering method, similar to diffusing bonding, usually needs to be done in a protective atmosphere due to the risk of oxidation.

Figure 1-6 shows a chart describing and comparing the two joining methods. A, B are subject materials to be joined and C is the filler material utilized for making the bond. Compared to diffusion bonding, brazing/soldering method has the benefit of lower processing temperatures. However, the brazing/soldering method might have a drawback of introducing more interphase between A and B due to interdiffusion reactions of the present materials.

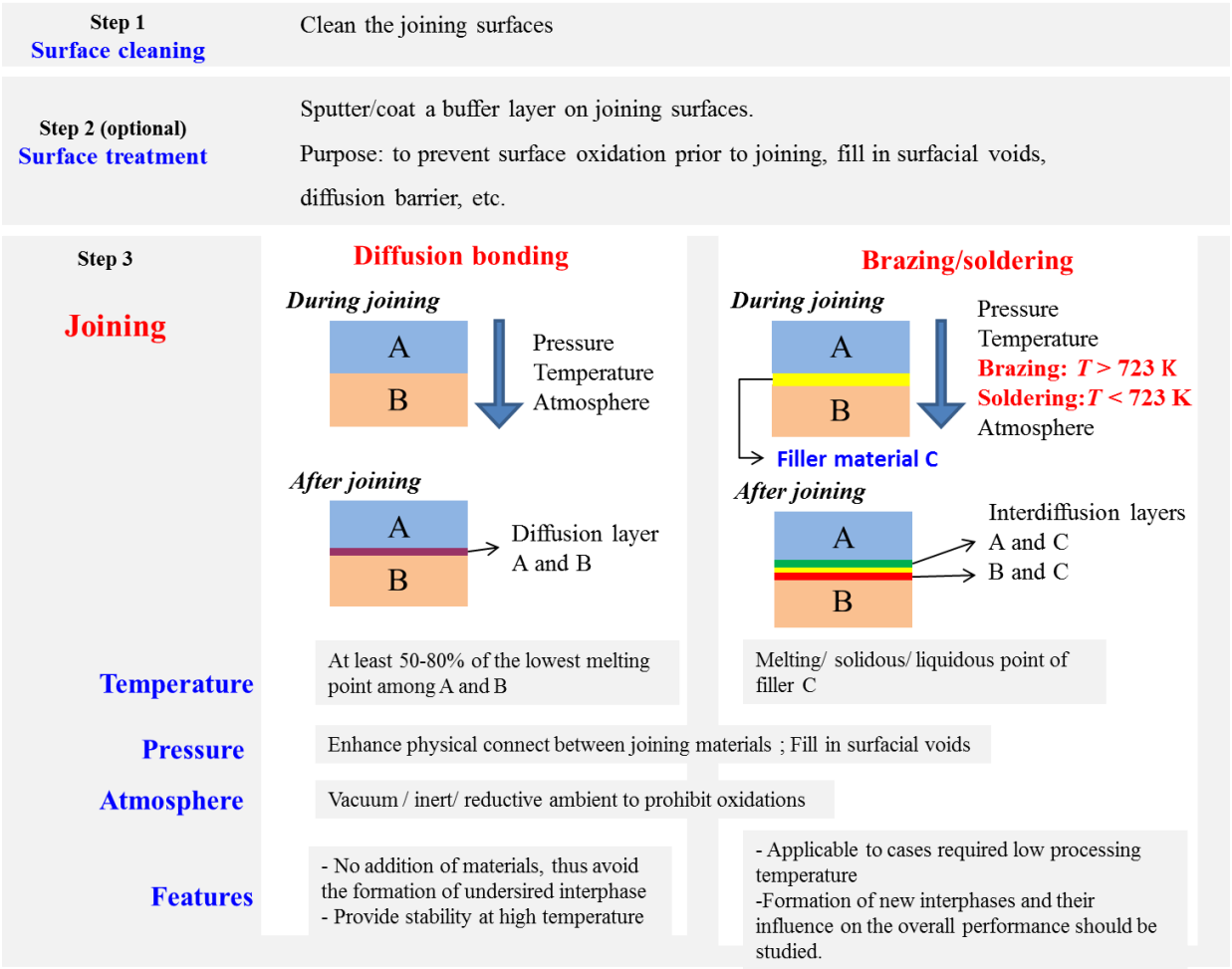

Figure 1-6 Schematic joining steps in diffusion bonding and brazing/soldering methods and comparison between them.

Joining material selection

Based on the requirements of a qualified contact in the fabrication of segmented TEG [44]–[50], it is commonly agreed that material selected for joining should possess the following features:

- The coefficient of thermal expansion (CTE) of the joining material should match those of the TE materials. Any possible mismatch between them should be tolerable so that the joint can be maintained under operation. A high mismatch of CTE between materials increases the probability that severe the problems of delamination or debonding after a thermal cycle can occur. The problem of CTE mismatch, however in some cases can be released if at least one material has high elasticity [48], [51].
- Especially for joining processes using the brazing/soldering method, the selected third material (or the selected filler material) should not form any undesired interphases with TE

materials that might degrade the TE performance of the phase. Diffusion of the filler into the TE during operation which reduce the performance reliability needs to be avoided [52].

- Processing temperatures should be within the tolerance temperature range of TE materials. Temperature applied on TE materials during the joining process can be considered as a heat treatment, which might negatively affect the performance of the TE materials.
- The joining material should be itself chemically stable (i.e. no oxidation or reduction under the working conditions of TEG).

1.4.3 Overview of segmented TEGs and their relevant fabrication techniques

As a consequence of flourishing research encompassing issues from material development to device fabrication, prototypes of TEG continuously evolves. An overview on the thermoelectric performance of non-segmented and segmented TEGs is presented in Table 1-2 below. Additional details on joining techniques and stability tests of the mentioned TEG are given in Table 1-3. Development of non-segmented TEG has made significant achievements in efficiency. For example, the TEG composed of half-Heusler $Hf_{0.3}Zr_{0.7}CoSn_{0.3}Sb_{0.7}$ and $Hf_{0.6}Zr_{0.4}NiSn_{0.995}Sb_{0.005}$ possesses the conversion efficiency 8.7% with a hot side temperature T_h = 970 K and temperature gradient of 948 K [53]. Skutterudites-based TEG has the efficiency of 9.1% under 325 – 868 K working temperature ($NdFe_{3.5}Co_{0.5}Sb_{12}$ and $Yb_{0.35}Co_4Sb_{12}$) [54]. Segmentation has significantly improved the record efficiency of TEG. Under working temperature range of 296 – 961 K, 13.8% is the efficiency of segmented TEG with *p*-leg $Bi_{0.4}Sb_{1.6}Te_3$/ $CeFe_{3.5}Co_{0.5}Sb_{12}$ and *n*-leg $Bi_2Te_{2.95}Se_{0.05}$ / $CoSb_3$ [55]. A 3-stage segmentation of *p*-type BiTe/ TAGS/ $Hf_xZr_yTi_z$-NiSbSn and *n*-type BiTe/ PbTe/ $Hf_xZr_yTi_z$-CoSbSn gave the an efficiency of 11.8% under working condition of 293 – 935 K [56]. It is optimistic that the goal of 15 % efficiency is going to be reached.

Table 1-2 Recent development of non-segmented (1.4.3.1) and segmented TEG (1.4.3.2)

(For definition of symbols, see the List of Symbols)

1.4.3.1 Non-segmented TEG								
Materials	Dimension (mm^3) (*d*: diameter)	ΔT (K)	TE Outputs (per 1 TE element)					R_c/ R_{total} ratio
			η (%)	Power density (Wcm^{-2})	P_{max} (mW)	I_{max} (A)	V_{max} (mV)	
p- $Fe_2VAl_{0.9}Si_{0.1}$ *n*- $Fe_2V_{0.9}Ti_{0.1}Al$ [57]	4.5 x 4.5 x 4.2	T_h = 573 T_c = 293	0.35	-	66.7	12	421	0.19
p- $Fe_2VAl_{0.9}Si_{0.1}$ *n*- $Fe_2V_{0.9}Ti_{0.1}Al$ [58]	*d* = 5 *l* = 5	ΔT = 280	-	133	52.2	9.8	22.2	0.007

p-$Fe_2V_{0.84}Ti_{0.16}Al_{0.97}Sb_{0.03}$ *n*- $Fe_3VAl_{0.9}Si_{0.07}Sb_{0.03}$ [53]	4.5 x 4.5 x 4.2	T_h = 573 T_c = 293	-	342	138.9	15	32.2	-
p- $Hf_{0.3}Zr_{0.7}CoSn_{0.3}Sb_{0.7}$ *n*- $Hf_{0.6}Zr_{0.4}NiSn_{0.995}Sb_{0.005}$ [53]	-	T_h = 970 ΔT = 930	8.7	-	380	-	-	-
n- $Ti_{0.33}Zr_{0.33}Hf_{0.33}NiSn$ [59]	-	ΔT = 565	-	275	11	-	-	-
p- $Fe_2VAl_{0.9}Si_{0.1}$ *n*- $Fe_2V_{0.9}Ti_{0.1}Al$ [60]	2 x 2 x 3	T_h = 673 T_c = 373	1.4	700	116.7	952.8	0.015	-
p- $Ce_{0.45}Co_{2.5}Fe_{1.5}Sb_{12}$ *n*- $Yb_{0.25}Co_4Sb_{12}/Yb_2O_3$ [61]	d = 5 l = 10	T_h = 810 ΔT = 490	6.4	70	3.1	0.105	0.23	-
p-$In_{0.25}Co_3Fe_1Sb_{12}$ *n*-$In_{0.25}Co_{3.95}Ni_{0.05}Sb_{12}$ [62]	d = 10 l = 10	T_h = 871 T_c = 329 ΔT = 543	1	0.5	0.782	25	140	0.53
p- $La_{0.7}Ba_{0.1}Ga_{0.1}Ti_{0.1}Fe_3Co_1Sb_{12}$ *n*- $Yb_{0.3}Ca_{0.1}Al_{0.1}Ga_{0.1}In_{0.1}Co_{3.75}Fe_{0.25}Sb_{12}$ [63]	5 x 5 x 7.6	T_h = 873 T_c = 323 ΔT = 550	8	-	1000	25	150	-
p-$Ce_xFe_3CoSb_{12}$ *n*- $Yb_xCo_4Sb_{12}$ [64]	1.7 x 1.7 x 2	T_h = 665 T_c = 293 ΔT = 372	-	-	17.5	~1	55.56	-
p-$Mn_{0.28}Fe_{1.52}Co_{2.48}Sb_{12}$ *n*- $Yb_{0.09}Ba_{0.09}La_{0.05}Co_4Sb_{12}$ [65]	4 x 4 x 4	T_c = 288 or 353 ΔT = 500	-	-	250	-	87.5	R_c~30 × 10^{-10} Ωm^2
p- $NdFe_{3.5}Co_{0.5}Sb_{12}$ *n*- $Yb_{0.35}Co_4Sb_{12}$ [54]	2 x 2 x 4.7	T_h = 823 T_c = 343	9.1	-	400	~10	-	*p*-leg: 0.03 *n*-leg: 0.022
p- $La_{0.7}Ba_{0.1}Ga_{0.1}Ti_{0.1}Fe_3CoSb_{12}$ *n*- $Yb_{0.3}Ca_{0.1}Al_{0.1}Ga_{0.1}In_{0.1}Co_{3.75}Fe_{0.25}Sb_{12}$ [66]	5 x 5 x 7	T_h = 873 T_c = 303	8	-	1063	-	-	-
p- PbTe *n*- $(AgSbTe_2)_{0.15}(GeTe)_{0.85}$ [46]	d = 7.5 l = 8	T_h = 773 ΔT = 683.	6	-	1150	17	130	0.035

p-LAST (PbSbAgTe) *n*-LASTT (PbSbAgSnTe) [67]	5 x 5 x 7	T_c = 315 ΔT = 888	-	-	472	8.6	220	0.39
p-$MnSi_{1.73}$ *n*-$Fe_{0.95}Co_{0.05}Si_2$ [68]	-	T_c = 373 ΔT = 600	2.7	-	-	-	-	-
p-$Fe_{0.9}Mn_{0.1}Si_2$ *n*-$Fe_{0.94}Co_{0.06}Si_2$ [69]	10 x 25 x 10	ΔT = 500	-	1.83	0.047	140	-	-
n- Sb-doped Mg_2Si [70]	4 x 4 x 10	ΔT = 500	-	-	121	5	80	0.38
n- Sb-doped Mg_2Si [71]	4 x 4 x 10	T_h = 873 T_c = 342 ΔT = 531	-	-	121.1	-	49.6	0.39
p-$Ca_{2.7}Bi_{0.3}Co_4O_9$ *n*-$Ca_{0.92}La_{0.08}MnO_3$ [72]	3 x 3	T_h = 773, ΔT = 390	-	0.041	7.94	-	112.5	-
p-$Ca_{2.7}Bi_{0.3}Co_4O_9$ *n*-$CaMn_{0.98}Mo_{0.02}O_3$ [73]	5 x 5 x 4.5	T_h = 897 ΔT = 565	-	0.0425	21.25	-	125	-
p-$Ca_{2.7}Bi_{0.3}Co_4O_9$ *n*-$CaMn_{0.98}Mo_{0.02}O_3$ [74]	5 x 5 x 4.5	T_h = 1273 ΔT = 975	-	-	42.5	-	87.5	0.085
p-$Ca_3Co_4O_9$ *n*-$Zn_{0.98}Al_{0.02}O$ [75]	4 x 4 x 8	T_h = 1173 ΔT = 700	0.37	200	64	-	167.5	-

1.4.3.2 Segmented TEG

Materials	Dimension (mm^3)	ΔT (K)	Output (per 1 TE element)					R_c/ R_{total} ratio
			η (%)	*Power density* (Wcm^{-2})	P_{max} (*mW*)	I_{max} (*A*)	V_{max} (*mV*)	
p-leg*:* $Bi_{0.4}Sb_{1.6}Te_3$ /$CeFe_{3.5}Co_{0.5}Sb_{12}$ *n*-leg*:* Bi_2Te_3 /$CoSb_3$ [76]	*p*-leg: 13.5 (mm^2) *n*-leg: 15.9 (mm^2) l =14.5	T_h = 973 T_c = 300 ΔT = 673	5.5	1.14	300	7.3	180	0.022
p-leg*:* $Bi_{0.4}Sb_{1.6}Te_3$ /$CeFe_{3.5}Co_{0.5}Sb_{12}$ *n*-leg*:* $Bi_2Te_{2.95}Se_{0.05}$ /$CoSb_3$ [55]	d ~ 8 l = 18	T_h = 961 T_c = 296	13.8	-	1640	-	240	-
p-leg*:* Bi_2Te_3 /ErAs:$(InGaAs)_{0,8}(InAlAs)_{0,2}$ *n-leg:*	-	T_h = 600 T_c = 300	-	-	43.3	78.7	-	-

Bi_2Te_3 /ErAs:InGaAs [77]								
p-leg*:* BiTe /TAGS/ $Hf_xZr_yTi_z$-NiSbSn *n*-leg*:* BiTe/PbTe/ $Hf_xZr_yTi_z$-CoSbSn [56]	3 x 3	T_h = 933 T_c = 293	11.8	-	425	18.5	-	-
p-leg*:* $Bi_xSb_{2-x}Te_3$ /$Ag_{0.9}Pb_9Sn_9Sb_{0.6}Te_{20}$ *n*-leg*:* $Bi_2Te_{3-x}Se_x$ /$Ag_{0.86}Pb_{19+x}SbTe_{20}$ [78]	1.4 x 1.4 x 4	T_h = 674 T_c = 368	6.56	-	1.824	-	-	-
n-leg*:* Bi_2Te_3:Se/ $CoSb_3$:In or $CoSb_3$:Te [79]	0.785 (mm^2)	T_h = 673 T_c = 288	9.3	1.49	1160	60	-	-
p-leg*:* BiTe/ Mg_2Si:Bi *n*-leg BiTe/ HMS [80]	4×4×5	ΔT = 771	5	-	240	6.8	150	0.005
p-leg*:* $Bi_{0.4}Sb_{1.6}Te_3$ /Zn_4Sb_3 /$CeFe_4Sb_{12}$ *n*-leg Bi_2Te_3/$CoSb_3$ [32]	-	T_h = 923 T_c = 300	-	-	520	-	210	-
p-leg*:* $Ti_{0.3}Zr_{0.35}Hf_{0.35}CoSb_{0.8}Sn_{0.2}$ / $Ca_3Co_4O_9$ *n*-leg $Zn_{0.98}Al_{0.02}O$ [75]	4 x 4 x 8	T_h = 1073 T_c = 444	1.16	0.650	207.3	-	190	-
p-leg*:* $Ti_{0.3}Zr_{0.35}Hf_{0.35}CoSb_{0.8}Sn_{0.2}$ / $Ca_{2.8}Lu_{0.15}Ag_{0.05}Co_4O_{9+\delta}$ [75]	*l* = 6 mm	T_h = 1173 T_c = 300	5	2.25	160	-	-	0.08

Table 1-3 Joining technique and stability test of recent TEGs.

Material	Joining technique	TE performance stability test	Test environment	Ref
p- $Fe_2VAl_{0.9}Si_{0.1}$ *n*- $Fe_2V_{0.9}Ti_{0.1}Al$	Electrode: Cu Cu electrode was pressed into TE material and heated upto 1200 K for 1-2 mins by feeding current (SPS) under pressure 20 MPa.	-	Air	[57]
p- $Fe_2VAl_{0.9}Si_{0.1}$ *n*- $Fe_2V_{0.9}Ti_{0.1}Al$	Same as above	Tested on running motorcycle, upto 2000 km	Air	[58]
p- $Fe_2V_{0.84}Ti_{0.16}Al_{0.97}Sb_{0.03}$ *n*- $Fe_3VAl_{0.9}Si_{0.07}Sb_{0.03}$	Same as above	-	Air	[53]
n-leg only $Ti_{0.33}Zr_{0.33}Hf_{0.33}NiSn$	Ag paste	-	-	[59]
p- $Fe_2VAl_{0.9}Si_{0.1}$ *n*- $Fe_2V_{0.9}Ti_{0.1}Al$	-	T_h = 330 to 573 K After 3000 cycles (1500 hours): Resistance of TEG unchanged. But power decrease gradually, due to the decrease of voltage.	Air	[60]
p-$Ce_{0.45}Co_{2.5}Fe_{1.5}Sb_{12}$ *n*-$Yb_{0.25}Co_4Sb_{12}/Yb_2O_3$	Hot side electrode: Mo-Cu, using solder foil Ag-Cu; joined by using SPS, 1023 K under 10-20 MPa Cold side electrode: Cu, using conventional Sn-based solder.	After 5 cycles: no deterioration in output power observed	Vacuum	[61]
p-$In_{0.25}Co_3Fe_1Sb_{12}$ *n*-$In_{0.25}Co_{3.95}Ni_{0.05}Sb_{12}$	Mo-Cu electrode, join with Ti as an interlayer.	1000 hours at 725K. No degradation detected.	-	[62]
p-$Ce_xFe_3CoSb_{12}$ *n*-$Yb_xCo_4Sb_{12}$	Electrode: Co-Fe-Ni based alloy. Co-Fe-Ni based alloys were used as diffusion barrier material.	100 heating/cooling cycles: no change	-	[63]
p-$Mn_{0.28}Fe_{1.52}Co_{2.48}Sb_{12}$ *n*-$Yb_{0.09}Ba_{0.09}La_{0.05}Co_4Sb_{12}$	Metal diffusion barrier used. Joining by high temperature brazing method.	Total resistance has no noticeable change after 30 cycles. Soaking test: (keep temp at 748 K): ASR_C increase 20% after 200 hours	-	[65]
p-$NdFe_{3.5}Co_{0.5}Sb_{12}$ *n*-$Yb_{0.35}Co_4Sb_{12}$	Electrode for n-type: $CoSi_2$, Electrode for p-type: Co_2Si. Joining done simultaneously with hot pressing of TE powder, with electrode foils on top	-	Vacuum	[54]

p-$La_{0.7}Ba_{0.1}Ga_{0.1}Ti_{0.1}Fe_3CoSb_{12}$ *n*-$Yb_{0.3}Ca_{0.1}Al_{0.1}Ga_{0.1}In_{0.1}Co_{3.75}Fe_{0.25}Sb_{12}$	Co-Ni-family metal alloy was used between TE element and electrodes	500 cycles in total. After the 450th cycle: power degraded 9.5 % from 29.5 to 26.7 W. Resistance increase 210% to 227 mΩ.	-	[66]
p- PbTe *n*-$(AgSbTe_2)_{0.15}(GeTe)_{0.85}$	-	Worked constantly 8 months without performance degradation	Air	[46]
p-LAST (PbSbAgTe) *n*-LASTT (PbSbAgSnTe)	Electrode: Cu/Brazing alloy (premabraze 616)/Stainless steel 316 TE element joint to electrode by using Sn/Te exothermic bonding wafer	-	Air	[67]
p-$MnSi_{1.73}$ *n*-$Fe_{0.95}Co_{0.05}Si_2$	Hot side electrode: $TiSi_2$. Solder: Ti-activated silver. Cold side electrode: Fe plated with Ni. Solder chosen based on the properties of $FeSi_2$. Solder A603, contains Zinc (90 wt.%), Al (5 wt.%), Cu (5 wt%).	-	Vacuum	[68]
$Fe_{0.9}Mn_{0.1}Si_2$ $Fe_{0.94}Co_{0.06}Si_2$	Electrode: Pt sheet	-	Vacuum	[69]
n-leg: Sb-doped Mg_2Si,	Electrode: Ni. Ag-based brazing alloy	-	-	[70], [71]
p-$Ca_{2.7}Bi_{0.3}Co_4O_9$ *n*-$Ca_{0.92}La_{0.08}MnO_3$	Electrode: Pt wire. Pt paste was used	-	Air	[72]
p-$Ca_{2.7}Bi_{0.3}Co_4O_9$ *n*-$CaMn_{0.98}Mo_{0.02}O_3$	Electrode: Ag. Ag paste containing oxide powder was used	Durability tested by heating-cooling cycles. Damages observed in TE n-legs.	-	[73]
p-$Ca_{2.7}Bi_{0.3}Co_4O_9$ *n*-$CaMn_{0.98}Mo_{0.02}O_3$	Electrode: Ag, Ag paste containing oxide powder was used.	10 cycles with T_h = 723 K. No power degradation observed.	Air	[74]
p-$Ca_3Co_4O_9$ *n*-$Zn_{0.98}Al_{0.02}O$	Electrode: Ag, Brazing material: Ag	-	Air	[75]
p-leg: $Ti_{0.3}Zr_{0.35}Hf_{0.35}CoSb_{0.8}Sn_{0.2}$ / $Ca_{2.8}Lu_{0.15}Ag_{0.05}Co_4O_{9+\delta}$	Electrode: Ag, Brazing material: Ag Brazing joining process was conducted in a vacuum using the SPS under 20 MPa at 973 K for 10 minutes.	T_h and T_c were kept at 1153 and 397 K. The maximum power remained almost constant up to 336 hours.	Air	[75]

1.4.4 Factors affecting the performance of TEG

1.4.4.1 Material-related factors

Under practical working conditions, (for example, in running vehicles, high temperature furnaces or incinerator) there are numerous factors that influence the performance of a TEG. Some typical ones are continuous cycling of heating/cooling processes, severe ambient atmosphere, mechanical stress and vibrations, etc. [22].

Stability of TE materials

Some TE materials are not stable at a certain temperature range, for example they can be oxidized or change their nominal compositions due to sublimation of highly volatile components [6], [30], [81], [82]. For example, zinc tri-antimonide Zn_4Sb_3 has a very high figure of merit, zT = 1.3 at 670 K [83], [84], but this material is unstable due to cracks and Zn whiskers occurring at the cold end of the material under large temperature gradients [85]. Problems regarding poor thermal stability have been reported in *p*-type lead tellurides PbTe [22], [86] and TAGS [87]. Besides, PbTe contains scared element that becomes source of toxicity during service [22], [86]. TAGS is an example of material with high zT of 2 but suffers the phase - unstability problem at a temperature range of 673 K, the performance of TAGS-based TEG is thus not stable at that temperature [87]. Mg_2Si oxidizes at mid-high temperatures, above 723 K [88] and requires an oxidation-protecting layer (for instance, $FeSi_2$) to be able to function in regular air condition [89]. Bismuth tellurides - based materials are the best TE materials at temperatures below 523 K, their figure of merits of zT are over 1 [29], [90], however it undergoes degradation by sublimation, oxidation, and reactions at temperatures above 523 K. Therefore, a protective atmosphere or protection barrier layer is required to minimize this degradation. Another example is the skutterudites $CoSb_3$, with zT of ~1 at 873 K, also suffers from oxidation and sublimation problems and requires effort to protect it (such as using aerogel encapsulation) [65], [91]–[95].

The information on sublimation rate of some selected TE materials is given in Table 1-4. The allowable limit of sublimation is a 5% reduction in cross sectional area after 10-year in operation, that is ~ 1×10^{-7} g cm^{-2} h^{-1} [22]. It seems to be challenging that many TE materials that can operate at high temperature range contain elements with a sublimation rate higher than this limit. Development of a high performance and stable TE material is thus practically necessary.

Table 1-4 Sublimation rate of selected materials [22]

Material	**Temperature (K)**	**Sublimation rate (g cm^{-2} h^{-1})**
TAGS	773	~1
PbTe	773	~9.4×10^{-2}
n-Skutterudites	873 973	5.16×10^{-3} 2.15×10^{-2}
p-Skutterudites	873 973	4.12×10^{-4} 2.7×10^{-3}
SiGe	1273	4.8×10^{-5}
$La_{3-x}Te_x$	1273	8×10^{-3}
$Yb_{14}MnSb_{11}$	1273	1×10^{-3}

Mechanical endurance and strength of TE materials, stability of contacts

As a stepping stone towards applications, there have been an increasing number of studies on the mechanical properties of TE materials to improve these [22], [96]. From a practical point of view, mechanical properties of TE materials are of high importance in order to circumvent possible failure of TE devices during operation [22], [96]–[100]. In service, TEGs can undergo mechanical stress, vibration (especially in vehicles), stress due to thermal shock and thermal cycles (originate from mismatches in thermal expansion coefficients) especially at high temperatures, etc. [98], [100]–[105]. A typical example is bismuth tellurides compounds, whose crystal structure consists of layers of –Bi–Te–Bi–Te–Bi– with strong covalent-ionic bonds, but these layers are loosely bonded together by van der Waal force [2]. Thus, along the direction of van der Waal bonds, the material is highly prone to delamination and crack formation during processing [22]. Lead tellurides require careful handling because their surface is susceptible to crashes [22]. This is due to the fact that heavy doping is a common way to obtain high performance *p*-type PbTe. The method results in distortion of PbTe crystal structure and has a negative effect on the material's hardness [106]. Therefore materials with lower *zT* but better mechanical endurance (such as half-Heusler [6], [22]) and processing methods can be attractive for utilization in a TEG, although sometimes at the cost of reducing the TE performances [22]. The list of mechanical properties for some typical available TE materials is provided in Table 1-5.

Beyond the scale of material, the influence of mechanical properties on the TEG's output performance is studied by Sarhadi et al. [96]. They concluded that increasing the lengths of TE legs results in high mechanical reliability and efficiency of the TEG, yet the legs should not be too long to maintain a decent power output. Besides, increasing the widths of the TE legs results in improving the output thermopower, but the widths should be small enough to keep the thermal stress on the TEG and at the contacts low.

Table 1-5 Mechanical properties: Young modulus, fracture strength, hardness, and toughness of some typical TE materials

Materials	Young's modulus E (GPa)	Poisson's ratio	Fracture strength (MPa)	Hardness (GPa)	Toughness (MPa $m^{0.5}$)	Coefficient of thermal expansion (10^{-6} K^{-1})	Thermal shock resistance (Wm^{-1})
Bi_2Te_3	32	-	62	0.62	1.1	-	-
$Bi_2Te_{2.7}Se_{0.3}$	52	-	-	2	-	14-16	-
$Bi_{0.4}Sb_{1.6}Te_3$	46	0.25	-	1	-	16-18	-
PbTe	27.7	0.22	50	0.39-0.43	0.35	20	77
PbSe	36.9	-	-	0.58	-	-	-
PbS	39.3	-	-	0.71-0.91	-	-	-
Zn_4Sb_3	71.7	0.26	56.6	2.1	0.8	-	-
$Ca_3Co_4O_9$	84	-	320	2.5	2.8	8-18	-
$CoSb_3$	148	-	-	6	-	-	-
$Yb_{0.35}Co_4Sb_{12}$	164	0.2	111	8	1.7	11	227
$Ce_{0.45}Nd_{0.45}Fe_{3.5}Co_{0.5}Sb_{12}$	154	-	-	6	-	-	-
Mg_2Si	117	0.18	5.6	1.3	-	-	-
Half-Heusler	225	-	-	13	-	-	-
$Si_{0.8}Ge_{0.2}$	143	0.23	-	14.5	0.98-1.03	-	-

1.4.5 Contact resistance

1.4.5.1 Thermal and electrical contact resistance

A major challenge in the fabrication of TEG is how to make contacts between TE material and the other parts of the TEG with minimum contact resistances. In general, whenever two materials are connected to each other, there will be a "contact resistance" at the interface, both electrically and thermally (illustrated in Figure 1-7). Low contact resistances are essential for high TEG performance [1], [107]. Inadequate contact resistances can easily drown out the benefits given by TE material properties and therefore efforts to reduce contact resistances are considered to be of the same importance as efforts to enhance TE materials' performances [107].

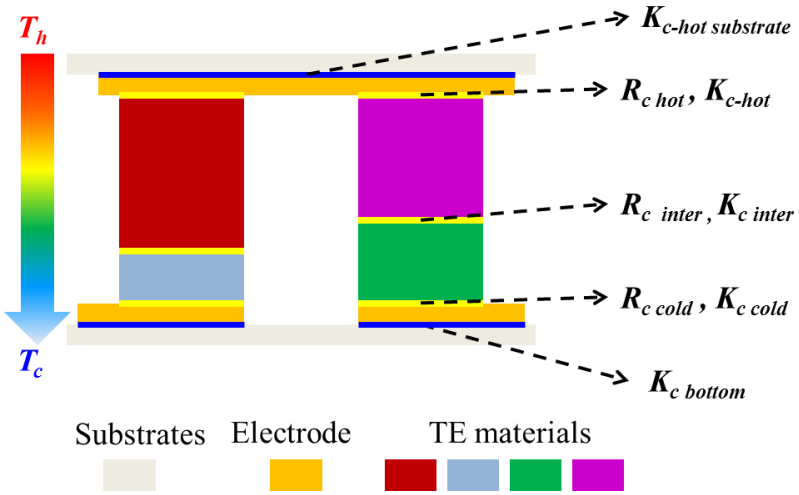

Figure 1-7 Sources of contact resistance in a TEG

Effects of thermal contact resistance

Thermal contact resistance K_c affects the transport of heat from one material to the other and introduces heat loss at the contact interfaces. In a TEG, K_c exists at all interfaces, e.g. interfaces between substrates-electrodes, electrodes-TE materials and between the TE materials themselves. In the cases where the thermal resistance is not adequately designed the overall output voltage of the generator decreases. For the energy conversion efficiency goal of 20%, it is required that the thermal contact resistance should not be more than 20% of the total leg thermal resistance, given that all the other contact resistances are neglected [107].

Effects of electrical contact resistance

Electrical contact resistance (R_c) sources e.g. from metal electrodes-TE materials and the TE materials interfaces have a direct impact on the generated current. A high R_c value could tremendously decrease the electrical current generated and introduces local heating, which in turn

reduces the temperature gradient along the TE element and in the end reduces the output voltage. The influence of R_c on the overall performance of a TEG is dependent on the constituent TE and electrode materials, as well as geometries of the TEG. Thus, detailed analysis of the effect of the total electrical contact resistance R_c on the output performance of a TEG is often conducted [1][107]. Figure 1-8 gives an estimation of the influence of contact resistance on the overall energy conversion efficiency of a TEG. Quantitative evaluation of the detrimental influence of contact resistance on the overall efficiency of a TEG suggests that the efficiency of the TEG decreases by 10% for each 10% contribution of contact resistance to the TEG's total resistance [1]. Another estimation provides a limit that the portion of electrical contact resistance in the TEG's total resistance should be less than 30% so that the degradation of efficiency would be no more than 20% [107].

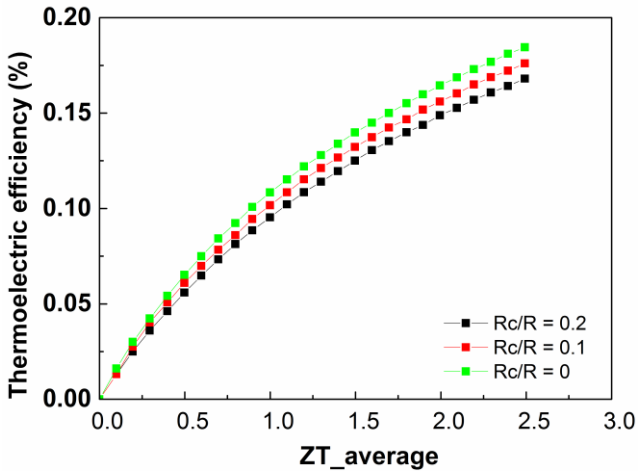

Figure 1-8 The influence of contact resistance on maximum obtainable efficiency of a TEG. (*R* is the total leg resistance, including R_c) [1]

As previously discussed, contact resistance of a TEG has a crucial role in realizing the full potential of TE materials which the TEG is composed. Therefore, techniques to determine the electrical contact resistances need to be developed and used.

1.4.5.2 Principles of contact resistance measurement

Consider a joint structure between material A and B. The resistance produced by A/B junction is called R_C (Figure 1-9 a). Often, the junction between A and B is so thin that measurement of bulk resistance cannot be applied directly and thus needs to be done indirectly. By applying the two resistance probes on materials A and B, a measured resistance is obtained:

$$R_{measured} = R_A + R_C + R_B = \rho_A \frac{l_A}{A_A} + \rho_C \frac{l_C}{A_C} + \rho_B \frac{l_B}{A_B} \qquad (1.32)$$

where ρ is the electrical resistivity; l is the length and A is the cross sectional area , subscripts A, B denote material A, B, and C is the contact.

$$A_A = A_B = A_C = Area \tag{1.33}$$

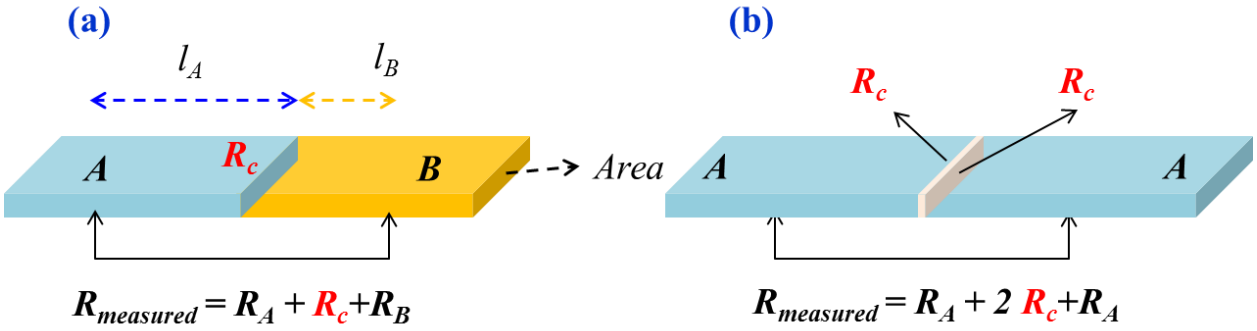

Figure 1-9 Illustrative basics of the contact resistance measurement

Provided that ρ_A, ρ_B: known from separate measurements and l_A, A_A and l_B, A_B can be measured, we can determine R_C from:

$$R_C = R_{measured} - R_A - R_B \tag{1.34}$$

Since it is very difficult to accurately determine the values of l_C, or the thickness of the interlayer between A and B due to possible inter-diffusion, the value of the product $\rho_C l_C$ is used instead. The product $\rho_C l_C$ is defined as area specific contact resistance ASR_C and is used as the standard for comparison of contact resistances in different systems.

$$ASR_C = \frac{R_{measured} - R_A - R_B}{A} \tag{1.35}$$

In practice, a popular configuration for the measurement of contact resistance is described in Figure 1-9 b, where two materials are joined in a sandwich A/B/A structure. Scanning probe and transmission line – based techniques which will be described below are the two commonly used methods to measure the contact resistance of an A/B/A sandwich structure.

1.4.5.3 Scanning probe technique

In this technique, the resistance measurement is done with one probe fixed and the other probe is moved gradually across the junction between two materials (Figure 1-10). Within the region of one material, the resistance measured increases linearly and forms a line by plotting the measured values versus moving distance. Until the moving probe crosses the point of contact, the plotted line is shifted by an amount of R_C [48], [108]–[110]. The precision of the measurement is influenced by the probe size and the closeness of the scanning probe to the junction. A small probe size reduces the parasitic resistance at the probe itself and the sample. The closeness the probe from the junction, in addition, diminishes the possible fluctuation of resistance due to the TE material's inhomogeneity.

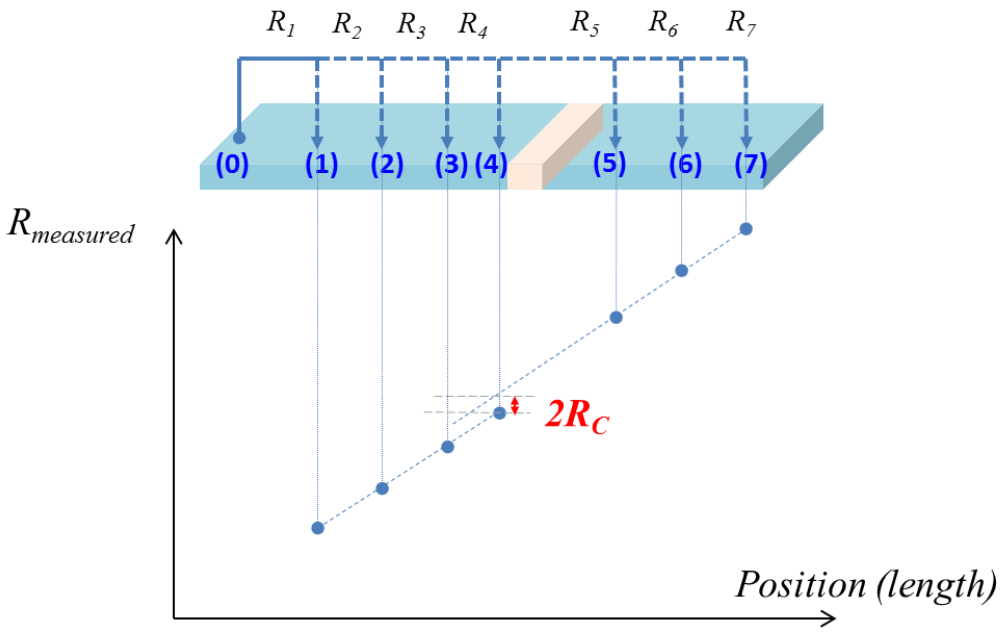

Figure 1-10 Contact resistance measurement: scanning probe method

1.4.5.4 Transmission line- based technique

This technique is based on the principle of the method to measure the resistance between a semiconductor plate and the attached metal electrode in transmission line production [50], [91]. In principle, the resistance measured across a junction between two materials can be formulated as:

$$R_{measured}\,(l, A) = R_{materials}\,(l, A) + 2\,R_c = \rho\frac{l}{A} + 2R_C \qquad (1.36)$$

$R_{measured}\,(l, A)$ is a linear function of length (or distance between probes) and cross sectional area, with the intercept with y-axis representing the contact resistance $2R_C$. Thus, by keeping either l or A constant and varying the other value, it is possible to plot $R_{measured}$ slope and extrapolate it to get the intercept with y-axis, or R_C. The principle of the technique is visualized in Figure 1-11.

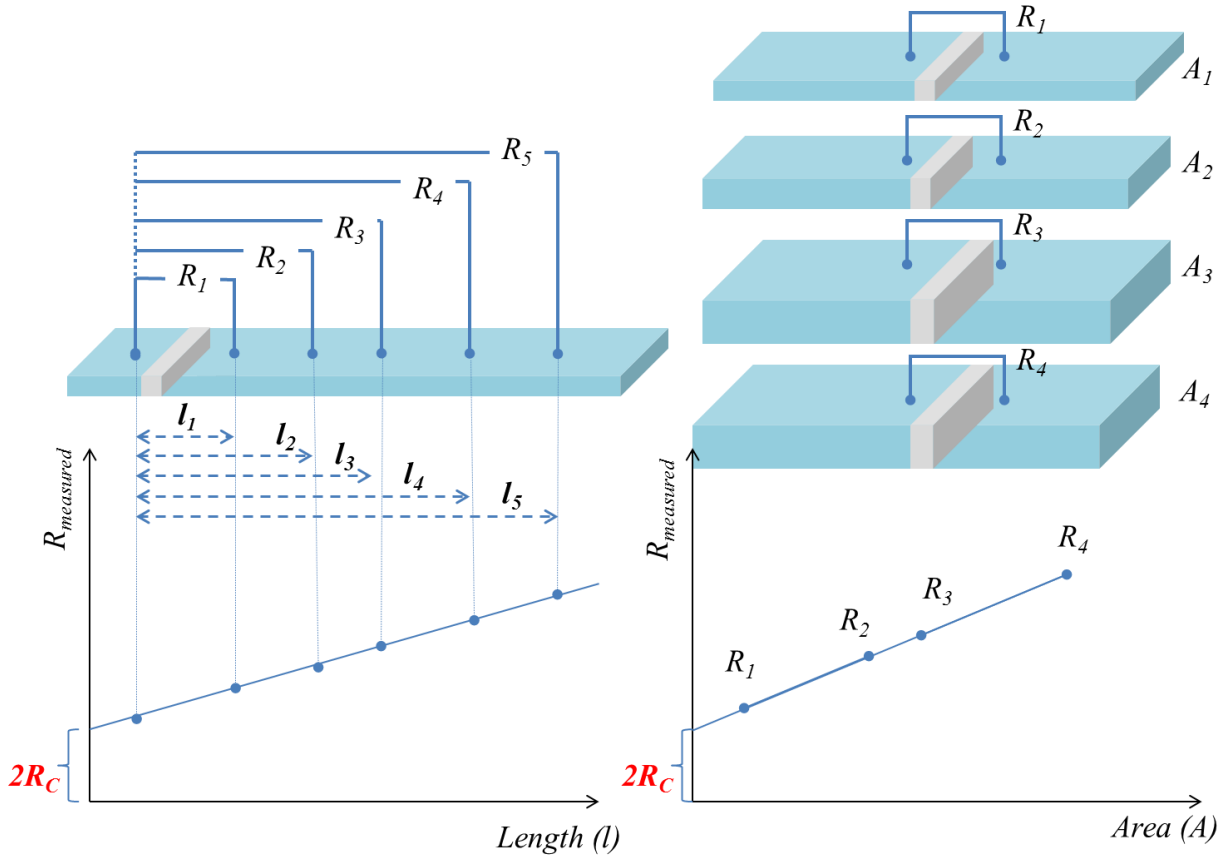

Figure 1-11 Contact resistance measurement: transmission line-based method. (a) Vary length. (b) Vary cross sectional area.

1.5 Overview of Energy status and waste heat recovery technologies

1.5.1 Energy demand and sources

Energy is the driving force of life. The total world energy consumption in 2015 is expected to be 168×10^{12} kWh and it will increase 10 times, to 1691×10^{12} kWh just in the next 20 years [111]. Various resources have been exploited to address the tremendously increasing need for energy. These sources can be classified as renewable and nonrenewable ones. Nonrenewable resources including coal, oil, and natural gas take the vast fraction of the total energy's supply [112]. The renewable resources including solar, wind, geothermal, tidal energy and biomass, just to name a few, and these take the moderate share of ~10 % [112]. The detailed contributions of the main energy sources to supply the global energy demand in 2011 and the outlook in 2040 is shown in Figure 1-12. The shares are: coal 20 – 19 %, oil 37 – 31 %, gas 26 – 28 %, nuclear 8 – 9 %, biofuels 4 – 7 %, and other renewables 2 – 3 %. It is evident that the contributions of renewable energy sources are still modest and those of nonrenewable sources are still dominant. However, it is

forecasted that with the current energy consumption rate, the remaining source of nonrenewable energy will be depleted in 40 years [112], [113]. In this problematic context, the development of renewable energy is expected to increase and to become the leading source of energy for a sustainable future [112].

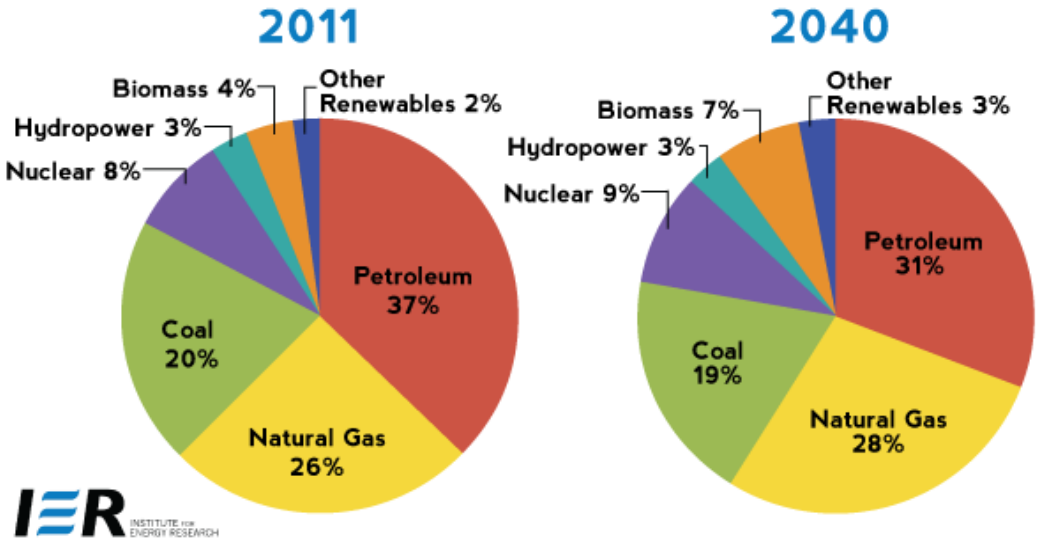

Figure 1-12 Fuel shares of world total primary energy supply in 2011 and outlook to 2040 (%) [114]

1.5.2 Waste heat recovery and the prospects of thermoelectricity

Most energy efficient consumption processes such as industrial refining or manufacturing furnaces, liquid/gas conducts, combustion engines, and transport vehicles, utilize only 60% of the energy [113], [115], [116]. This means that a considerable amount of energy is wasted, i.e. 40%. The energy waste is mainly in the form of heat [113]. An example showing pathways of energy generated from a typical combustion engine is shown in Figure 1-13. The usable energy sources take only 25% of the total applied energy, meanwhile a fraction of 30 % is lost to cooling systems, 5 % is friction and parasitic losses, and particularly a significant amount of 40 % is lost as waste heat. According to reference [117], based on their temperature, waste heat sources can be classified into three types: low-temperature range: below ~ 505 K, medium-temperature range: ~ 505 – 723 K and high-temperature range: above ~ 723 K. Collecting and converting this waste heat to usable energy is believed to provide a new promising avenue to the global energy saving strategies.

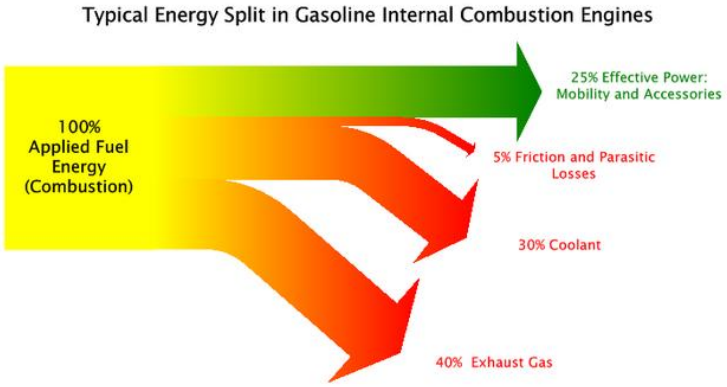

Figure 1-13 Typical paths of energy generated in a fueled combustion engine vehicles [118]

Over the years, there have been various technologies developed to convert waste heat into usable energy. Based on their mechanism, they can be categorized into heat-to-heat and heat-to-electricity recovery techniques [117]. Heat-to-heat recovery techniques have been demonstrated in industry while heat-to-electricity techniques so far have not been installed in practice. Table 1-6 provides more details and the application range of the methods.

Table 1-6 Waste heat recovery technologies and their application temperature range [117]

Waste heat recovery method		**Application temperature range**	**Typical applications**
Heat exchangers (transfer heat from gas exhausted to gas input)	Heat recuperator	Medium to high	Annealing ovens, furnaces, gas incinerators, etc.
	Regenerator	Medium to high	Especially applicable in waste heat sources contaminated with reactive or harsh agents.
	Regenerate/recuperative burners	Medium to high	Hot water boiling systems (in households or industry), hot liquid heating systems, etc.
Load preheating (Use waste heat from	-	Medium to high	Preheat feeding water for boiling, or systems that

a system to preheat the entering load).			preheating entering load is possible.
Generating power via mechanical work	Steam Rankine cycle	Medium to high	Power generation from solar, geothermal, and waste heat sources
	Techniques similar to Rankine cycle methods, but working fluid are either organic or mixture of ammonia and water	Low	
Direct heat to electricity conversion devices	Thermoelectric generation	Medium to high	Waste heat recovery in transport vehicles, industrials or domestic furnaces. (Not yet demonstrated in industry)
	Piezoelectric power generation	Low	Applied in systems where oscillatory expansion of exhausted gas can be reused to create a voltage output. (Not yet demonstrated in industry)
	Thermionic generation	High temperature (1273 K)	Industrial furnaces with temperature of exhausts above 1273 K. (Not yet demonstrated in industry)

Although heat-to-heat recovery techniques have been applied successfully in practice, their major drawback is the requirement of a concentrated heat sources (such as at the exteriors of high temperature heating furnaces) [113]. In situations of dilute waste heat sources in medium-high temperature range, such as in automobiles, exhausted gas or fluid, etc., thermoelectrics becomes a

highly suitable technique [23], [113], [117]. For the medium temperature range (~ 505 – 723 K), possible applications can be stream boiler exhausts, furnaces, exhaust system of transport vehicles, etc. At higher temperatures, thermoelectric generators can be used for example in metal manufacturing furnaces, etc. [111], [119]. For the low temperature range (below ~ 505 K), thermoelectric generators can collect waste heat for instance from cooling water systems of machines, equipments, household ovens, electronic devices, etc.

Compared to other renewable energy technologies, thermoelectrics possess numerous advantages:

- Thermoelectric generators are solid-state devices, free of complicating moving parts and noise-free.
- They are highly reliable, with no requirement of maintenance.
- They operate without secondary waste such as emissions of greenhouse gases [120].

1.5.3 Costs of renewable energy sources

The energy conversion efficiency of a TEG is expected to be about 10 – 15 % with the average materials' figure of merit of about 1 [113]. This value is not among the highest energy generation efficiency as compared to other processes, for example, fuel cell 50-70 %, hydro (80 – 90 %) and wind (30 – 50 %). However, TE have a competitive cost of $ 3 - 4 per W, comparable to that of conventional fossil fuels-based energy processes' $ 3 per W [119], and less than some typical renewable energy processes, for instance solar energy and geothermal. Solar energy requires approximately $ 8 per Watt for installation and the electricity cost is 25 - 40 cent per kW-hr [116]. The cost of geothermal is $ 3-4 per W. In addition, thermoelectrics become more promising with the possibility to bring down the material costs per watt in TEGs even further by 10 fold when contacting systems and optimum device design is applied and developed [121].

1.6 Thesis outline

The scope of this thesis is to design and optimize an effective thermoelectric generator (TEG) by the segmentation approach. Numerical modeling based on the compatibility factor approach was used to efficiently select materials, design segmented legs and TEGs, and predict their performance. Based on the numerical modeling result, segmentation of half-Heusler thermoelectric materials and bismuth tellurides was chosen. The research is then focused on solving the issues regarding joining, such as contact resistances and interfacial diffusion/reaction between these two different TE materials and between them with metal electrodes, which is a benchmark to realize an effective segmented TEG. This thesis is organized with six chapters, as follows.

First of all, the basic theoretical concepts of thermoelectrics including the theoretical model used to design an effective segmented TEG are provided in Chapter 1. Practical knowledge on

development of TE materials and fabricating TEGs are also provided. Then, a short overview of the global energy problem and the potential of thermoelectric power generation as alternative technology for waste heat recovery are presented.

Chapter 2 provides details of typical experimental techniques used in this thesis to synthesize TE materials, fabricate and characterize TE elements, which are the components to build up a completed TEG. The included techniques are: arc melting, spark plasma sintering, joining methods to make the electrode and join TE materials to fabricate segmented TE leg, Seebeck microprobe scanning and contact resistance measurement of interface after joining to evaluate the joining processes.

As the first step in this thesis work, Chapter 3 presents the theoretical study to design high efficiency segmented TEGs using a numerical modeling method. Different material combinations with their improved conversion efficiency are suggested. The results are the guideline to efficiency-beneficial selection of material combinations for segmentation. In the temperature range between room temperature and 900 K, the calculated results show that half-Heusler and bismuth tellurides are promising for segmented TEG with a maximum efficiency of 11.5%.

After selecting half-Heusler and bismuth tellurides to develop segmented TEG, the next step is fabrication of the hot side electrode. In chapter 4, an innovative joining method by fast hot pressing was applied to directly join *p*- and *n*-type TE material half-Heusler with silver as the hot side electrode. Interfacial microstructure evolution and the electrical contact resistance were investigated and the obtained results are presented and discussed.

Then, in Chapter 5, the challenging issue regarding joining *p*- and *n*-types TE Bismuth tellurides with half-Heusler is addressed. This is a crucial step toward the development of high performance segmented TEG with bismuth tellurides at the cold side and half-Heusler at the hot side. A process to join the two TE materials is introduced and then microstructures and the transport properties of the joining parts are characterized. The obtained segmented legs were subject the TE performance test with T_h at 873 and T_c at 323 K. The tested data were compared with theoretical prediction using numerical modeling. From the comparison, the influences of the obtained contact resistance to the total power output of the segmented legs are evaluated and discussed.

Last but not least, chapter 6 summaries the concluding remarks of the thesis in its entirely. Outlooks for future improvement of the current work are also provided.

2 Chapter 2 - Experimental methods

The experimental procedure from materials synthesis (half-Heusler alloys) to devices processing is shown in Figure 2-1. In this chapter only the experimental fabrication and characterization methods used in this study to fabricate and tested the TE legs such as Arc melting, Spark Plasma Sintering - SPS, joining, contact resistance measurement, and TEG characterization are described in details. General processes and characterization methods such as high energy ball milling, scanning electron microscopy and energy dispersive spectroscopy SEM - EDS, thermoelectric properties measurement ULVAC-ZEM 3, thermal conductivity measurement (laser flash LFA 475), etc. will not be included in this chapter, but can be found in any text book dealing with experimental techniques.

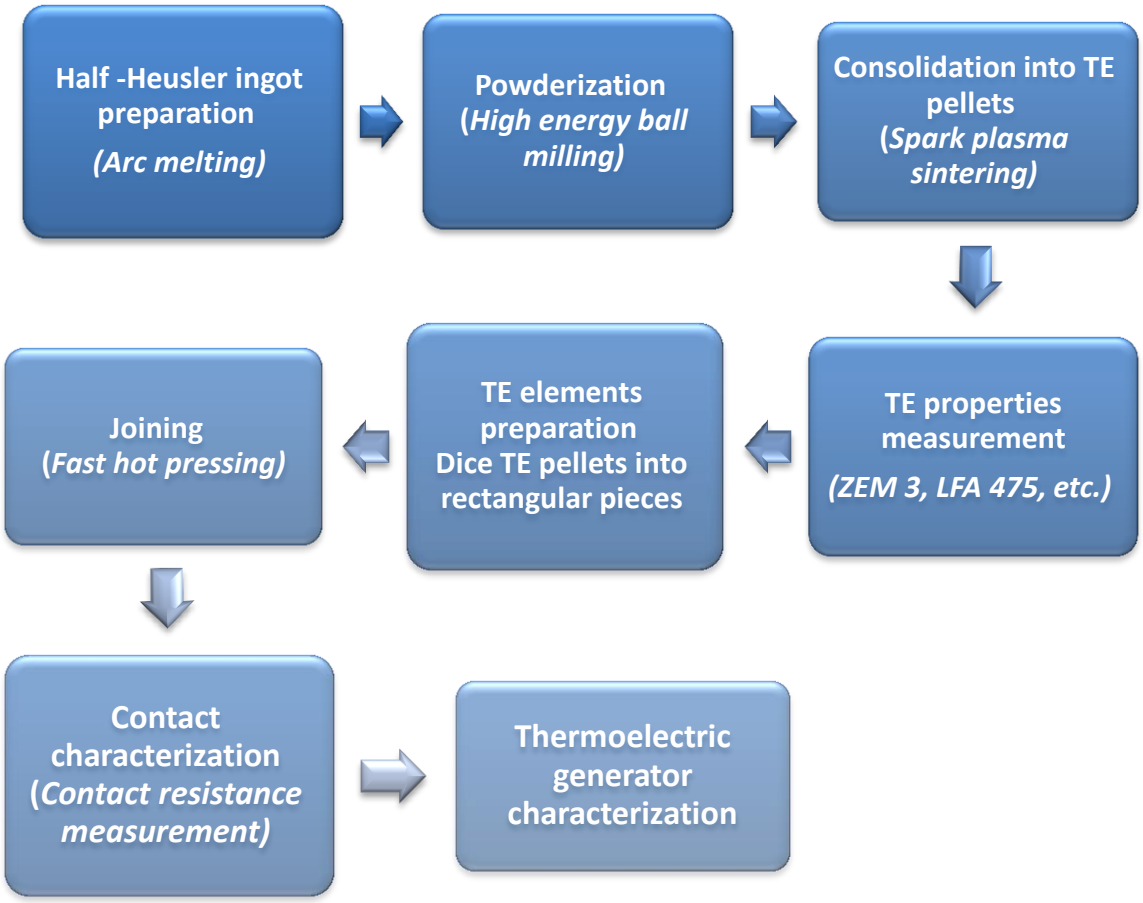

Figure 2-1 Procedure to fabricate thermoelectric generators

2.1 Material and device processing

2.1.1 Arc melting process

Arc melting is a conventional method to synthesize metallic alloys, in particular, from a mixture of pure element. An electrical arc is discharged from a tungsten tip towards the metal mixture and the heat produced in the materials melts them then turns them into a mixture of molten elements. When the mixture is cooled down, they become a united alloy afterwards, when the mixture is cooled down. The discharge of electrical arc is created by ionization of the highly pure Argon atmosphere in the arc melting chamber [122].

In this work, an arc melter Edmund Bühler [123] was used to prepare half-Heusler alloys samples. A schematic of the equipment is shown in Figure 2-2. A current of at least ~75 A is needed to melt the metal elements and this can be adjusted to ensure the melting of the elements. 99.9999% pure Argon gas applied in the melting process was at the pressure of 0.4 barr. The metal mixture was flipped and remelted several times in order to ensure a good homogeneity of elements. Stoichiometric mixture of Hf, Zr, Co, Sn, Sb for *p*-type samples and Hf, Zr, Ni, Sn, Sb for *n*-type samples were weighted in a portion of 8 grams to load into the arc melting Cu crucible. All the metal elements have the purity of at least 99.5%. In the process, water cooling is needed to avoid heating and melting of the Cu substrate. The nominal compositions of $Hf_{0.5}Zr_{0.5}CoSn_{0.2}Sn_{0.8}$ and $Hf_{0.5}Zr_{0.5}NiSn_{0.998}Sb_{0.002}$ are respectively for *p*-type and *n*-type half-Heusler alloys and determined by weighing the elements to the correct weight. The shape of the final samples after the arc melting is dependent on the shape of the Cu crucibles. In these experiments, the samples after arc melting had a button-like shape.

Figure 2-2 The Edmund Bühler arc melting system

2.1.2 Spark plasma sintering

Spark plasma sintering is a pressure-assisted pulse current sintering process to consolidate material from powder form to bulk form while still preserving their beneficial micro/nanostructures. The basic principle of the technique is to use a high current and high pressure to apply on packed material powder. A low voltage, high energy spark pulse current momentarily generates spark plasma at high localized temperatures, from several to ten thousand Kelvin between the particles resulting in optimum thermal and electrolytic diffusion. At the same time, high pressure applied onto the powder mixture presses the particles together and consolidates them. The consolidation course can be done in vacuum or in desired atmosphere [124].

The principle of the method is illustrated in Figure 2-3 [124]. TE material in the form of powder is loaded into a tube-shape graphite die. A layer of graphite paper is used to separate the powder from direct contact with the graphite die. Then, two graphite punches are placed on both ends of the powder mixture. The whole packed structure is placed between two electrodes in the SPS chamber. Electrical current is controllably run from an electrode, through the graphite die packed with material powder, to the other electrode. Through the electrodes, pressure was also controllably applied.

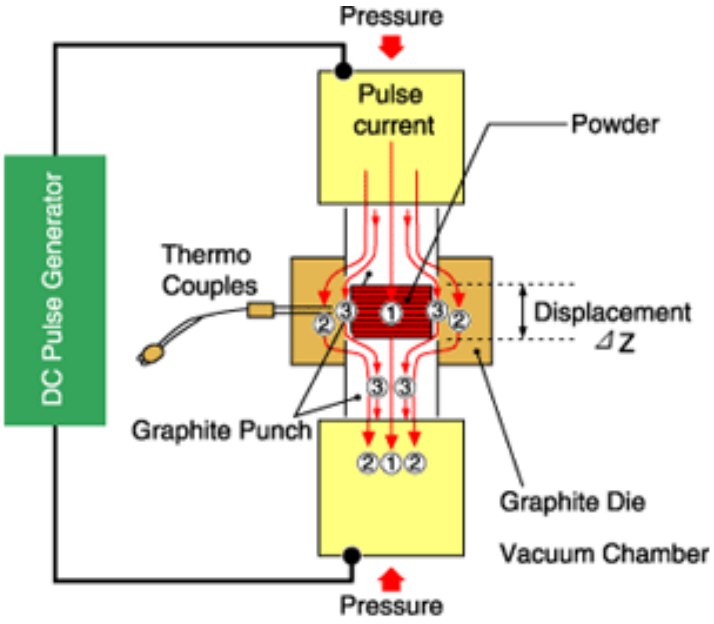

Figure 2-3 Principle of the spark plasma sintering [124]

In this work, the SPS unit of Dr. Sinter 515S (Syntex Inc., Japan) was used with a 3.3 ms - long pulsed direct current regulated by an on-off settings with the on-off ratio of 12:2. Photo of the system is shown in Figure 2-4.

Figure 2-4 Photo of the SPS units of Dr Sinter 515S (Syntex Inc., Japan) during sintering

2.1.3 Fast hot-pressing

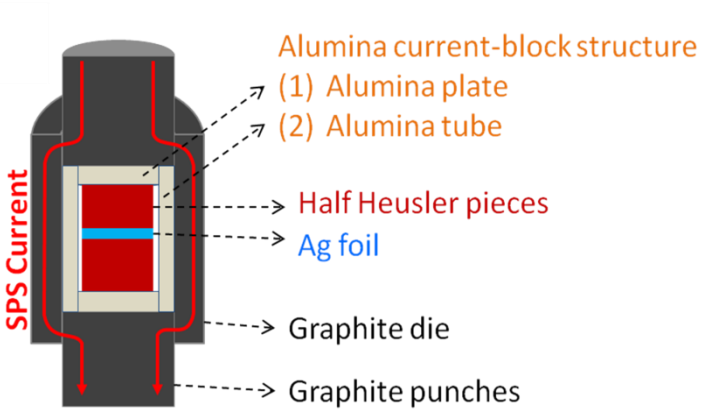

Figure 2-5 Fast hot pressing method modified from conventional Spark Plasma Sintering

Fast hot pressing method is a modified ordinary SPS method. In this method, the joining samples were electrically insulated with graphite die and punches by an alumina structure. This allows blocking the SPS current going through the TE materials but rather through the graphite die (see

Figure 2-5 yet maintaining the fast temperature ramping rate inherited in the SPS method. This robust temperature ramping process facilitates the preservation of performance of TE materials. Since the half-Heusler alloys are expected to be used in applications with high hot side temperatures up to 973 K, joining materials must be sustainable under these conditions. At the same time, the processing temperature of the materials should be maintained below 1073 K to avoid detrimental changes in the TE properties, e.g. Sb, Sn sublimations or material oxidation. Bulk half-Heusler was joined directly to Ag foil by applying a pressure of 40 MPa, at temperature of 1053 K and under vacuum.

Surface cleaning: TE bulk materials obtained from the SPS were cut into rectangular pieces with desired dimensions. Before the joining step, it is crucial that the surface to be joined is prepared and cleaned. First, the joining pieces were polished to remove residues from the previous cutting process. The polishing also provides adequate surface flatness to proceed joining. Then, the polished pieces were cleaned by ultrasonificating for 2 minutes in solutions of acetone, iso-propanol and de-ionized water. The final cleaning step was the exposure of joining surfaces to a rapid frozen CO_2 flow to freeze and blow away all the residues on the joining surface left after the ultrasonification.

2.2 Material and device characterization

2.2.1 Electrical contact resistance measurement

In this work, the characterization of contact resistance (R_c) between TE materials and metal electrode was done by a home-built system. The principle of the measurement is based on the transmission line technique discussed in Chapter 1. The schematic illustration of the equipment is given in Figure 2- 6. A bar-shaped sample with structure of TE material / joining material / TE material is fixed between two Ag electrodes, through which electrical current is passed. Six 50-µm-diameter Ag probes are attached onto the sample, crossing the contact interface in order to measure the voltage drop along the sample. The measured voltages are converted to electrical resistance R_i according to the equation $R_i = V_i/I$. By plotting R_i vs l_i, (i: 1, 2, 3, …) which is the corresponding distance between probes and extrapolate the intercept with y-axis, the contact resistance is determined (as explained in Chapter 1). l_i is measured by using an optical microscope with integrated ruler. The measurement is repeated with the current I reversed to compensate for the thermoelectric effect (if this happens).

The whole structure is put into a tube furnace with controllable temperature up to 973 K, the limit melting point of Ag probes. The ambient atmosphere was Nitrogen gas. Other desired ambient environment can also be applied.

The contact resistance between hot side electrode and TE half-Heusler material has been obtained with sample's temperature ranging from room temperature up to 773 K with the step of 323 K.

For the half-Heusler and bismuth tellurides segmented samples, the contact resistance has been measured with increasing temperature up to 473 K, the melting limit of the joining material.

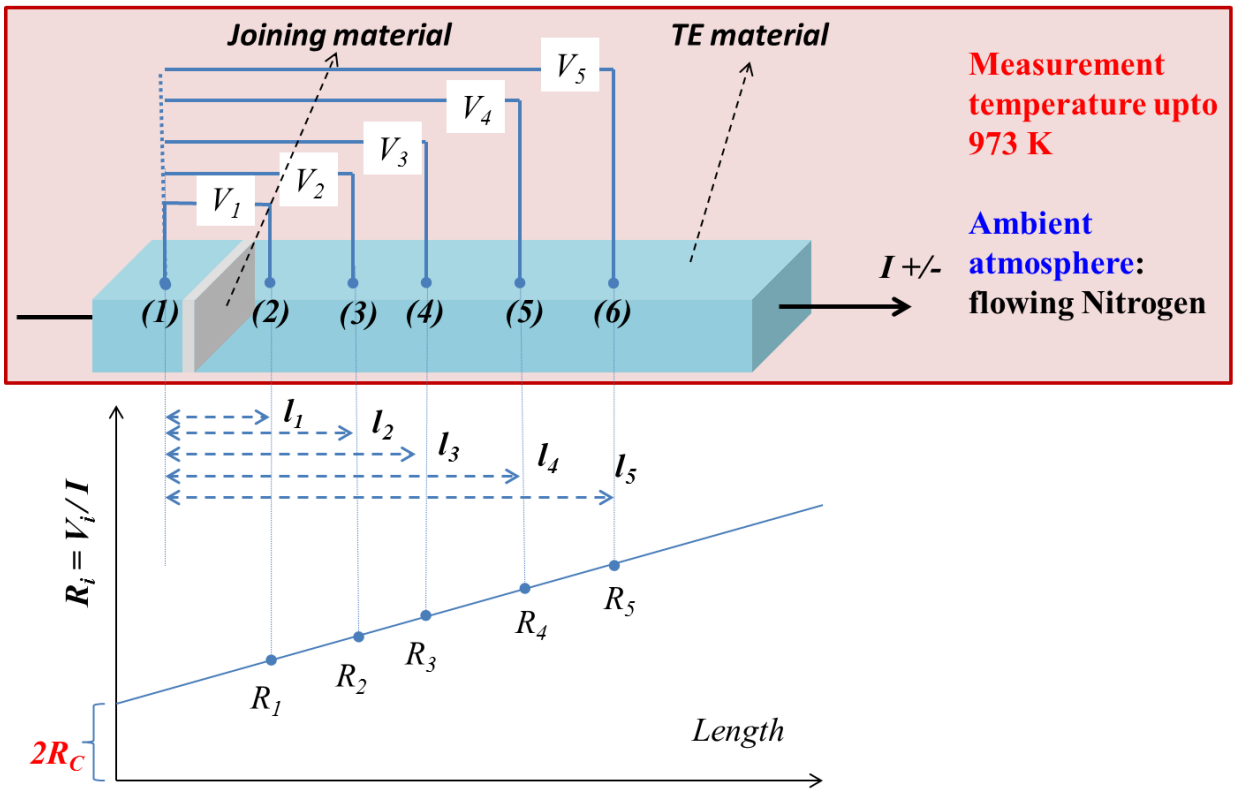

Figure 2-6 Schematic structure of self-made equipment to measure contact resistance as a function of temperature.

2.2.2 Seebeck scanning measurement

In order to track the changes of the thermopower at the junction of the joints, Seebeck scanning equipment (Panco) was used. The principle of the method is described in Figure 2-7. The measurement was done in air at room temperature. The resolution of the tracking step was 50 μm.

The probe consists of two thermocouples: Cu-Cu, whose one end sits at the probe's tip and the other end is in contact with sample, and CuNi-CuNi with one end connect to the side of the probe and the other end also in contact with the sample. During the measurement, the CuNi-CuNi and Cu-Cu wires at the probe's tip is heated to a temperature T_1, locally heating the sample area in contact with the tip. The other ends of the thermocouples sense the same temperature T_0. The setup is

equivalent to the configuration of two thermocouples: CuNi wire with the sample, and Cu wire with the sample. Due to the Seebeck effect, the temperature gradient T_1-T_0 on two ends of CuNi-CuNi and Cu-Cu appears an electrical voltage V_2 and V_1 respectively. These potentials are determined by the known Seebeck coefficients of CuNi (α_{CuNi}) and Cu (α_{Cu}), and the unknown Seebeck coefficient of the sample (α_{sample}):

$$V_1 = (\alpha_{sample} - S_{Cu})(T_1 - T_0)$$

$$V_2 = (\alpha_{sample} - \alpha_{CuNi})(T_1 - T_0)$$

Combining the equations for V_1 and V_2:

$$\alpha_{sample} = \frac{V_1}{V_2 - V_1}(\alpha_{Cu} - \alpha_{CuNi}) + \alpha_{Cu}$$

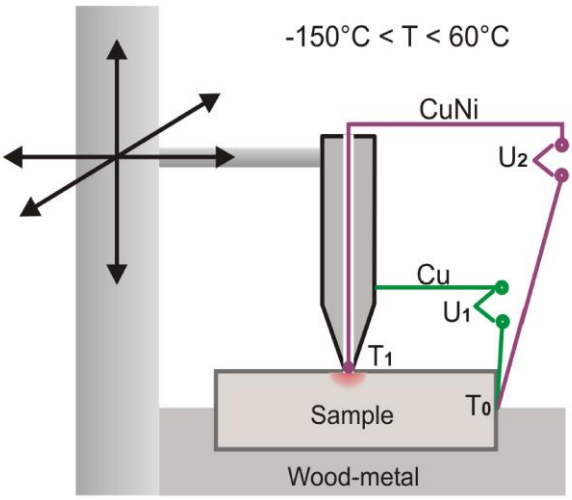

Figure 2-7 Schematic principle of Potential Seebeck Microscope (by Panco GmbH) [125]

The probe can move along x- and y- axes on the sample's surface to conduct the measurement, and thus a 2D profile of Seebeck coefficient is obtainable.

2.2.3 Thermoelectric generator tester

The thermoelectric performance of fabricated thermoelectric generators, including output voltage, current and power, has been measured by a test system built in-house. A schematic description of the principle of the test system is described in Figure 2-8 (a) and a photo of it is provided in Figure 2-8 (b). In principle, the system consists of two parts: a temperature controller to create temperature gradient and an electrical controller to measure the thermoelectric characteristics of the in-test TEG. The heat applied at hot side is programmable and produced by a SiN-based heater. The cold side temperature is maintained by running water with controllable temperature.

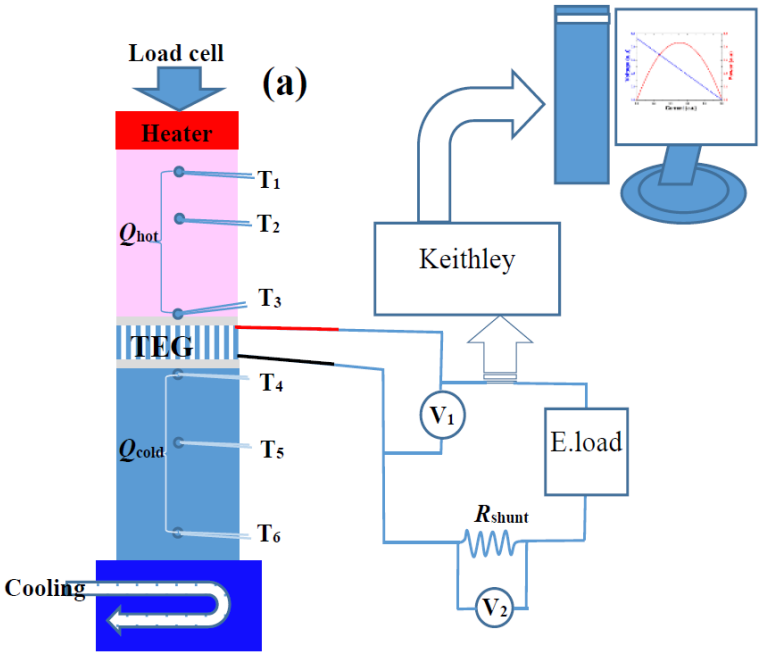

Figure 2-8 (a) Schematic principle of the thermoelectric generator tester [126]

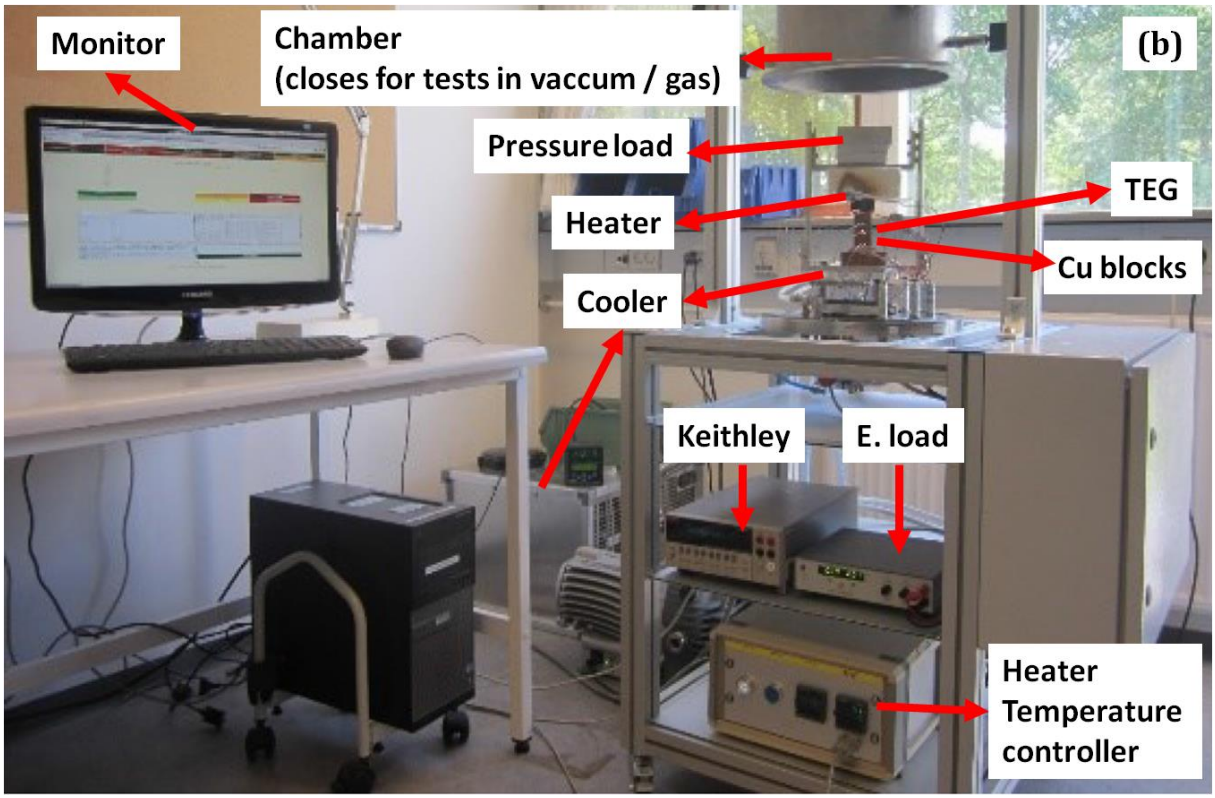

Figure 2-8 Photo of the TEG thermoelectric output test system [126]

The TEG is settled on top of the cooling stage and under the heater. A certain pressure is applied to the system in order to a keep good thermal contact between the heater, the thermoelectric generator and the cooler. Under a temperature gradient, the TEG generates an electrical voltage. The TEG is connected in series with an external load (R_{shunt}) and an electronic load (E.load) which control the current run in the whole circuit. The output current-voltage characteristic behavior of the TEG is obtained by sweeping the current from the E.load through the entire circuit and measurement of the corresponding voltage V_2 from the TEG. The range of the sweeping current is 0-15 A, with a minimum step of 1 mA. The value of the sweeping current is determined based on the measured voltage V_2 drop on R_{shunt}. It is possible to test the TEG in various environments: air, vacuum or certain gases (for example, Ar or Nitrogen). The tester has been calibrated by measuring a commercial thermoelectric module G2-40-0329 by Tellurex Corporation.

3 Chapter 3 - Towards high efficiency segmented thermoelectric unicouples

Abstract

Segmentation of thermoelectric (TE) materials is a widely used solution to improve the efficiency of thermoelectric generators over a wide working temperature range. However, the improvement can only be obtained with appropriate material selections. In this chapter, we provide an overview of the theoretical efficiency of the best-performing TEG consisting of one *p*- and *n*-legs, or unicouples, designed from segmenting the state-of-the-art TE materials. The efficiencies are evaluated using a 1D numerical model which includes all thermoelectric effects, heat conduction, Joule effects and temperature dependent material properties, but neglects contact resistance and heat losses. The calculations are performed for a fixed cold side temperature of 300 K and different hot side temperatures of 700 K, 900 K and 1100 K. We confirm that without taking into account the compatibility of TE materials, segmentation can even decrease the total efficiency. Choosing the TE materials carefully, one is, however, rewarded by a significant improvement in the total efficiency.

The work discussed in this chapter is published in Pham Hoang Ngan, Dennis Valbjørn Christensen , Gerald Jeffrey Snyder, Le Thanh Hung, Søren Linderoth, Ngo Van Nong and Nini Pryds, Physica status solidi (a), Volume 211, Issue 1, pages 9 – 17, January 2014

3.1 Introduction

As a short reminder from Chapter 1, the flourishing development of studies on thermoelectric materials have resulted in a large varieties of materials with figure of merit $zT = \alpha^2 T/\rho\kappa$ (with α, κ, and ρ being the Seebeck coefficient, thermal conductivity and electrical resistivity, respectively) exceeding 1, such as bismuth tellurides [6], [127], [128], skutterudites [15], [54], [129], Zintl phases [130]–[135], lead tellurides [136]–[138], silicon germanium [139], [140], zinc antimony [141], copper selenide [142], Cu-Se derivatives [143]–[146], $(AgSbTe)_{0.15}(GeTe)_{0.85}$ (TAGS) [87], $AgPb_mSbTe_{2+m}$ (LAST) [147], lanthanum telluride [148] and $CuGaTe_2$ [149]. Together with the development of high performance TE materials, TE device fabrication is also a growing area [150]. To achieve high thermal-to-electrical energy conversion efficiencies, it is desirable to operate thermoelectric generator devices over large temperature spans and to maximize the thermoelectric performance of the materials. However, no single thermoelectric material possesses a high performance over large temperature intervals. Therefore, it is necessary to combine different materials, which operate optimally in different temperature ranges. This can be achieved by, for example, cascaded or segmented generators where the *p*- and *n*-legs are formed from different materials joined in series [29], [32], [151], [152].

A cascaded system consists of different stages with each stage comprised of *p*- and *n*-legs made from single *p*- and *n*-type TE materials. The stages have their own independent electrical circuit. As a consequence, the optimum load resistance for each stage can be achieved individually, however, with the cost of both needing to do several load resistance optimizations and suffering from extra heat losses through the additional wires connecting each stage. In a segmented system, each *p*- and *n*- leg is subdivided into segments made from different materials. Unlike cascaded systems, segmented systems use only a single electrical circuit, but here a high figure of merit *z* is not the only prime importance. Selecting compatible materials for combination is also a critical issue for the optimal performance.

An example of an ineffective segmentation is the combination of TAGS with SiGe which – despite a high figure of merit of each material - results in a decrease of the overall efficiency (9.89%) when segmented as compared to a non-segmented leg of TAGS (10.45%). Despite the importance of the material compatibility and that the necessary theoretical framework has already been developed [6], [25], [153], so far the compatibility factors of only these materials have been reported: TAGS, *p*- and *n*- PbTe, SnTe, $CeFe_4Sb_{12}$, $CoSb_3$, La_2Te_3, *p*- and *n*- SiGe [154]. In this work, we broaden the materials of consideration, show how to select materials for high performing segmented systems and evaluate how efficient the best segmented TE elements and unicouples are expected to be. The evaluation of efficiency was carried out using a 1D numerical method and the materials used in this study are state-of-the-art TE materials reported in the literature.

3.2 Calculation model

The efficiency of segmented and non-segmented TE elements is calculated using the 1D model described in detail by J. Snyder [6] and in Chapter 1. The calculation model is valid for both non-segmented and segmented legs if – for the latter – the material properties are changed from one material to another at a certain interface temperature (T_i) where the segments meet. Here, equations used for efficiency computation is briefly mentioned again.

From the reduced current densities evaluated at the cold and hot side temperatures, $u_c = u(T=T_c)$ and $u_h = u(T=T_h)$, the efficiency of a single segmented or non-segmented leg η_{leg} can be found:

$$\eta_{leg} = 1 - \frac{\alpha_c T_c + \frac{1}{u_c}}{\alpha_h T_h + \frac{1}{u_h}} \qquad (3.1)$$

The value of u_h is a free parameter varied in the model to get the highest efficiency. In practice, u_h is varied by changing the load resistance. When an *n*-type leg and a *p*-type leg are connected electrically in series and thermally in parallel to form a unicouple, the efficiency $\eta_{unicouple}$ is calculated by

$$\eta_{unicouple} = 1 - \frac{\alpha_{p,c} T_c + \frac{1}{u_{p,c}} - \alpha_{n,c} T_c - \frac{1}{u_{n,c}}}{\alpha_{p,h} T_h + \frac{1}{u_{p,h}} - \alpha_{n,h} T_h - \frac{1}{u_{n,h}}} \qquad (3.2)$$

For the optimal case where $u(T) = s(T)$ at all temperatures, the maximum efficiency for a single leg ($\eta_{u=s}$) is calculated:

$$\eta_{u=s} = 1 - exp\left(-\int_{T_c}^{T_h} \frac{\sqrt{1+zT}-1}{\sqrt{1+zT}+1} \times \frac{1}{T} dT\right) \qquad (3.3)$$

3.3 Results and discussions

3.3.1 Compatibility factor: proof-of-concept

The features of the calculation model are described in Figure 3-1, which consider an example of a segmented leg consisting of $Bi_{0.6}Sb_{1.4}Te_3$, $Ba_8Au_{5.3}Ge_{40.7}$ and $MnSi_2$ that is subjected to T_c = 300 K and T_h = 900 K. Figure 3- 1a demonstrates an example of the temperature profiles of optimum relative current density $u_{\text{segmented}}$ (equation *1.23*) and efficiency η_{leg} (equation *3.1*) along the segmented leg. η_{leg} builds up along the $Bi_{0.6}Sb_{1.4}Te_3$ and $Ba_8Au_{5.3}Ge_{40.7}$ segments, and starts to decrease from $MnSi_2$ part. Comparing the almost constant relative current density with the widely varying compatibility factors of each segment (see Figure 3-1a) reveals that each segment operates far from their individual optimal conditions even though the whole segmented leg has been

optimized for efficiency. This results in a total efficiency of the entire leg (η_{leg} = 12.9%), which is much lower than the maximum obtainable efficiency ($\eta_{u=s}$ = 18.3%). The difference between the actual efficiency and the maximum obtainable efficiency diverges mainly in $Bi_{0.6}Sb_{1.4}Te_3$ and $MnSi_2$. In particular, the decrease in the overall efficiency by adding the $MnSi_2$ segment confirms the importance of choosing compatible materials as even replacing the incompatible $MnSi_2$ with a passive material (thermal insulator) will result in a better performance. Figure 3- 1b explains more details about the incompatibility of the three materials. The optimum relative current density for each segment – when working as a single material leg – is 5.7, 4.6 and 1.2 V^{-1} for $Bi_{0.6}Sb_{1.4}Te_3$, $Ba_8Au_{5.3}Ge_{40.7}$ and $MnSi_2$, respectively. Putting them into a segmented leg, with the cold and hot end fixed at 300 and 900 K, the segmented leg as a whole reaches its highest efficiency at u_h = 3.01 V^{-1}. From the profile of optimized $u_{segmented}$ along the leg (Figure 3- 1a), this corresponds to the u_h of 2.61, 2.59 and 3.01 V^{-1} for the $Bi_{0.6}Sb_{1.4}Te_3$, $Ba_8Au_{5.3}Ge_{40.7}$ and $MnSi_2$ segments, respectively. At these reduced current densities, the efficiencies are 7.77% for the $Bi_{0.6}Sb_{1.4}Te_3$ segment, 6.16% for $Ba_8Au_{5.3}Ge_{40.7}$ and -0.65% for $MnSi_2$. That is, albeit the $Bi_{0.6}Sb_{1.4}Te_3$ and $Ba_8Au_{5.3}Ge_{40.7}$ segments are not working at their optimal conditions, they both contribute to a positive efficiency, while the $MnSi_2$ segment consumes power in order to achieve the required current density in the segment.

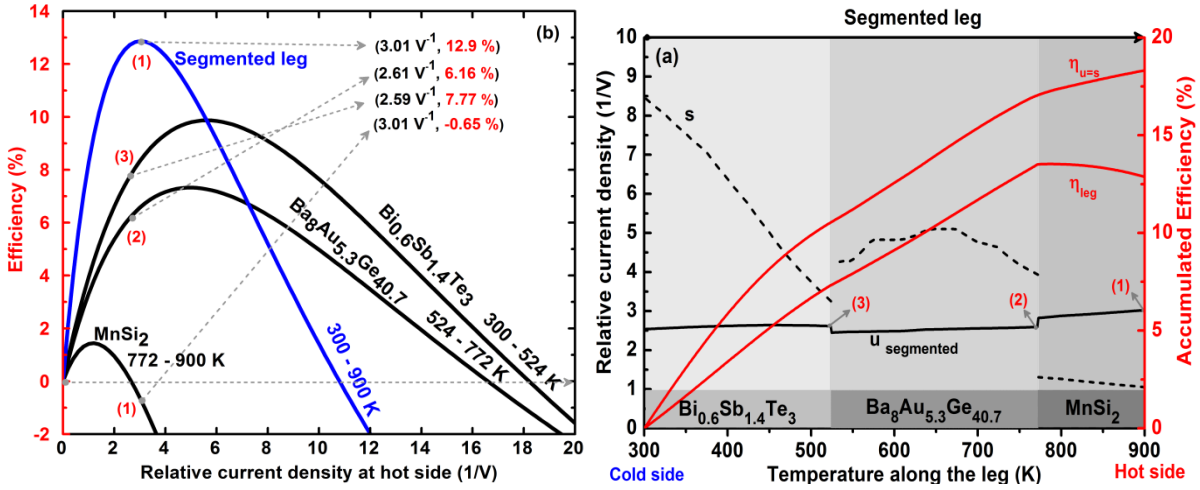

Figure 3-1 **a** *p*-type $Bi_{0.6}Sb_{1.4}Te_3$, $Ba_8Au_{5.3}Ge_{40.7}$ and $MnSi_2$ are segmented into a leg and subjected to a temperature span from 300 K (cold end) to 900 K (hot end). The relative current density $u_{segmented}$ giving the highest efficiency for the fixed 300 – 900 K temperature span is plotted through the leg together with the corresponding accumulated efficiency η_{leg}. The accumulated efficiency at any temperature T' is found from equation *1.23* by replacing T_h with T', α with $\alpha(T = T')$ and u_h with $u_{segmented}(T = T')$. If u were not constrained by equation *3.1*, its best performing value is the compatibility factor s. This would result in the efficiency $\eta_{u=s}$ as calculated from equation *3.3* with the replacement $T = T'$. The interface temperature is 524 K between $Bi_{0.6}Sb_{1.4}Te_3$ and $Ba_8Au_{5.3}Ge_{40.7}$ and 772 K between $Ba_8Au_{5.3}Ge_{40.7}$ and $MnSi_2$. **b**. Subjecting the segmented leg to a 300 – 900 K temperature span gives an efficiency, which is plotted as a function of the relative current density at the hot side, u (T = 900 K). The efficiency of each segment subjected to the appropriate temperature difference (e.g. 300 – 524 K for $Bi_{0.6}Sb_{1.4}Te_3$) is likewise shown at varying hot side relative current density. The relative current density that gives the maximum efficiency for the whole segmented leg is found from Figure 3-1 **a** and highlighted ((1), (2) and (3)). E.g. for the $Bi_{0.6}Sb_{1.4}Te_3$ segment

u (T = 524 K) = 2.61 V^{-1}, which produces an efficiency of 7.77% in the $Bi_{0.6}Sb_{1.4}Te_3$ segment as highlighted by point (3).

3.3.2 Materials in consideration and their TE efficiencies

In order to study the possible combinations of segmented TE couples, the state-of-the-art *n* and *p*-type TE materials have been considered. Thermal conductivity, Seebeck coefficient and resistivity as functions of temperature were collected from the literature. Note that these properties are not shown here. Figure 3- 2 shows the dimensionless figure of merit zT and the compatibility factors as functions of temperature for both *p*- and *n*-type materials. It is obvious from Figure 3- 2a and c, that below 500 K bismuth tellurides (both *n* and *p*-type) are hitherto the best performing materials. The majority of the materials such as PbTe, Zn_4Sb_3, TAGS, skutterudites, Cu_2Se, half-Heusler alloys show high zT at a medium-high temperature range of 500 – 1000 K. LAST is also a competitive material, with a reported zT of 2.2 at 800 K [147]. However, this high zT material so far has not yet been reproduced due to the difficulties in controlling its microstructure [155], [156]. To avoid a false impression, we do not include this reported data in the present calculation. At the higher temperature range (1000 – 1200 K) the zintl (*p*-type), lanthanum telluride (*n*-type) and silicon germanium (*p* and *n*-type) are the best available materials (without including some possible high temperature oxides such as ZnO:Al,Ga [157] and the $Ca_3Co_4O_9$ [158]).

Most of the collected materials are compatible with each other over a large temperature range. Both *p*-type and *n*-type bismuth tellurides, however, are not compatible with the other materials at the low temperature region (300 – 400 K) but become more compatible at higher temperatures (Figure 3- 2b-d).

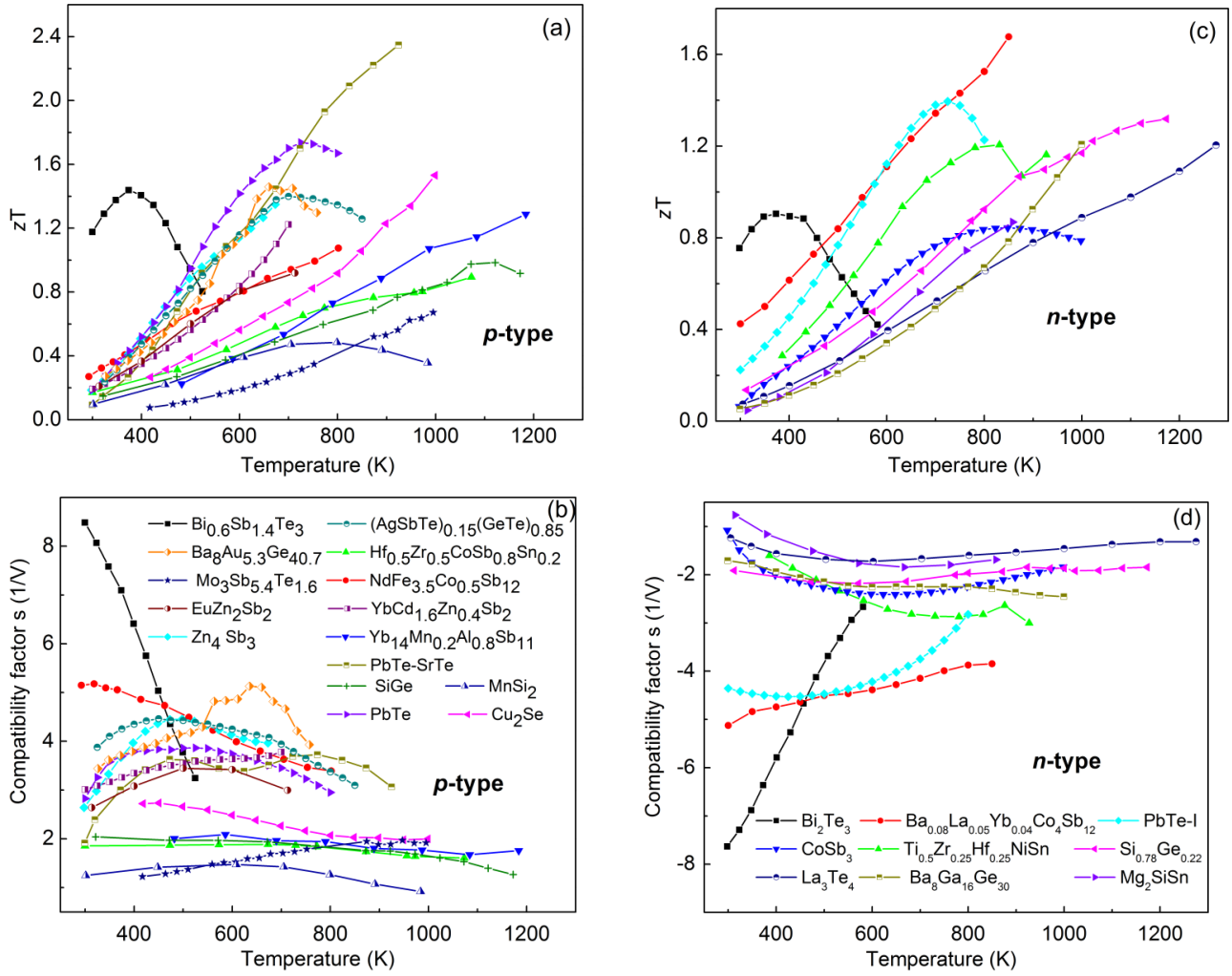

Figure 3-2 zT and compatibility factor s of the collected state-of-the-art p- (a,b) and n- (c,d) types thermoelectric materials. For each material, the references are shown in Table 3-1

The optimized efficiencies of the collected materials at different T_h = 700, 900 and 1100 K and T_c at 300 K were calculated using equation *3.1*, and the result is presented in Table 3-1. p- and n-type bismuth tellurides have efficiencies of 9.9% (300 – 525K) and 8.3% (300-580K), respectively. At 700 K, although PbTe-SrTe and PbTe have comparable zT values the efficiency of PbTe (11.1%) over the working temperature range of 300 – 700 K wins that of PbTe-SrTe (9.5%). This is due to the fact that over the entire temperature range of 300 – 700 K, the average zT of PbTe ($\overline{zT}$ = 1.18) is higher than that of PbTe-SrTe ($\overline{zT}$=0.97). However, PbTe-SrTe has been reported to stand at higher elevated temperatures, and achieves the highest efficiency of 15.3% among all the selected materials at the working temperature range of 300 – 900 K. For the n-type materials in this temperature range, the half Heusler alloy ($Ti_{0.5}(Zr_{0.5}Hf_{0.5})_{0.5}NiSn_{0.998}Sb_{0.002}$ [159]) shows the highest efficiency. Zintl, SiGe, $Si_{0.78}Ge_{0.22}$ and La_3Te_4 can be used at high temperature of 1100 K, where the Carnot efficiency is significantly increased, but their calculated efficiency values are just within 10 – 11% resulting from their good performance only at high temperatures (> 800 K). Therefore, if it is

not the case of segmentation one should use e.g. PbTe-SrTe joined with an insulator to bring down the hot side temperature, and reducing the capital cost of the TEGs.

3.3.3 Segmented legs

Figure 3 demonstrates the efficiencies of segmented *p*- and *n*- legs for non-segmented and 2- and 3-materials joined to a segmented TE legs with different hot side temperatures at T_h = 700, 900, and 1100 K. The listed TE materials given in Figure 3- 2 were paired with the bismuth tellurides to form segmented TE legs. For 3-segment legs, only the ones with the highest efficiencies are plotted. The gain in efficiency obtained by segmentation is also illustrated. In general, segmentation of most *p*-type materials gives a higher efficiency boost than *n*-type materials. Among *n*-legs, segmented *n*-clathrate leg with hot side at 700 K gives a significant improvement in efficiency of more than 50% compared to the non-segmented *n*-clathrate one. PbTe-I, *n*-HH (half-Heusler) and *n*-Skutt. (skutterudite) with their high *zT* are the three most efficient *n*-TE legs with efficiencies above 10% at 700 K (12% for segmented *n*-HH leg at 900 K). Among *p*-segmented legs, $Mo_3Sb_{5.4}Te_{1.6}$ exhibits the highest increment in efficiency i.e. from 2.1 % to 9.6 %. Strikingly, segmentation of PbSrTe to $Bi_{0.6}Sb_{1.4}Te_3$ provides an outstanding efficiency of over 19%. Yet, a better improved efficiency can also be obtained by segmentation of three materials of e.g. $Bi_{0.6}Sb_{1.4}Te_3$ [128] to $Ba_8Au_{5.3}Ge_{40.7}$[160] and PbSrTe [137]. Remarkably, an efficiency value of over 20% can be obtained for the segmented leg of $Bi_{0.6}Sb_{1.4}Te_3$/PbSrTe to zintl [131] or SiGe [139] for applications at temperature range of 300 - 1100 K, whereas the segmentation of zinlt or SiGe with $Bi_{0.6}Sb_{1.4}Te_3$ only results in an efficiency value of ~15%.

Table 3-1 Calculated efficiencies of collected TE materials working as single TE elements at 700, 900 and 1100 K. Missing data corresponds to temperatures where the TE material properties are not reported due to material instability or limitations of the measurement equipment

	Materials	Efficiency (%) T_h = 700 K	T_h = 900 K	T_h = 1100 K
p-type	$Bi_{0.6}Sb_{1.4}Te_3$ [128]	-	-	-
	$NdFe_{3.5}Co_{0.5}Sb_{12}$ [15]	8.9	-	-
	$Hf_{0.5}Zr_{0.5}CoSb_{0.8}Sn_{0.2}$ [16]	5.8	8.9	
	$Yb_{14}Mn_{0.2}Al_{0.8}Sb_{11}$ (zintl) [131]	4.5	7.6	10.8
	Zn_4Sb_3 [141]	10.4	-	-
	Cu_2Se [142]	6.2	9.8	-
	PbTe [136]	11.1	-	-
	PbTe-SrTe [137]	9.5	15.3	-
	$MoSb_{5.4}Te_{1.6}$ [161]	2.1	4.2	-
	$YbCd_{1.6}Zn_{0.4}Sb_2$ [162]	8.3	-	-
	$EuZn_2Sb_2$ [160]	8.1	-	-
	SiGe [139]	5	7.8	10.4
	$(AgSbTe)_{0.15}(GeTe)_{0.85}$ [147]	10.2	-	-
	$Ba_8Au_{5.3}Ge_{40.7}$ [160]	10	-	-
	$MnSi_2$ [163]	4.5	6.7	-

n-type	Bi_2Te_3 [54]	-	-	-
	$Ba_{0.08}La_{0.05}Yb_{0.04}Co_4Sb_{12}$ [15]	11.1	-	-
	$Ti_{0.5}(Zr_{0.5}Hf_{0.5})_{0.5}NiSn_{0.998}Sb_{0.002}$ [159]	7.7	13.8	-
	$CoSb_3$	6.2	9.6	-
	$PbTe_{1-x}I_x$ (x=0.0012) [138]	10.1	-	-
	$Si_{0.78}Ge_{0.22}$ [140]	5.8	9.5	-
	$Ba_8Ga_{16}Ge_{30}$ [164]	3.6	6.7	-
	Mg_2SiSn [163]	9.4	-	-
	La_3Te_4 [148]	4.3	7.2	10.0

3.3.4 Segmented unicouples

The *p*- and *n*- type segmented TE legs were then paired together to make TE unicouples whose efficiencies are calculated by using equation *3- 2* and the maximum values are presented in Table 3- 2. The legs were chosen in correspondence with their working temperature ranges (300 – 700, 900, or 1100 K). At hot side temperatures of 900 and 1100 K, besides 2-segment TE legs, only 3-segmented TE legs with the highest efficiencies were considered for unicouples. At T_h = 700 K, with the same *n*-leg, among the segmented *p*-legs, the unicouples with $Bi_{0.6}Sb_{1.4}Te_3$+TAGS *p*-legs give the highest efficiencies. Similarly, unicouples with Bi_2Te_3+PbTe *n*-segmented legs gives the best performance among the segmented *n*-legs. The unicouple paired from segmented $Bi_{0.6}Sb_{1.4}Te_3$+TAGS and Bi_2Te_3+PbTe legs has the efficiency of 13.5%, which is the top value computed in the 300 – 700 K range. For the same temperature range, the unicouple with non-segmented p-TAGS leg and *n*-PbTe leg gives an efficiency of 10.2% (not shown in Table 3- 2), which can be improved by about 30% by the segmentation of them with $Bi_{0.6}Sb_{1.4}Te_3$ and Bi_2Te_3 to form segmented legs. Increasing the hot side temperature up to 900 K, for most cases, although segmentations of 2 materials can enhance the performance of the unicouple, but the improvement is generally small. One example is: 2-segment unicouple of *p*-leg $Bi_{0.6}Sb_{1.4}Te_3$+PbSrTe and *n*-leg Bi_2Te_3+*n*-Clathrate possesses 15.2% efficiency, while the most efficient 3-segment unicouple of (*p*-leg $Bi_{0.6}Sb_{1.4}Te_3$+*p*-Clathrate+PbSrTe and *n*-leg Bi_2Te_3+PbTe+SiGe) gives 16.8%, that is, only a small enhancement. Increasing the hot side temperature up to 1100 K, designing unicouples with 3-material segments becomes more feasible. For example, the efficiency of 3-segmented unicouple comprising of *p*-leg $Bi_{0.6}Sb_{1.4}Te_3$+PbSrTe+SiGe and *n*-leg Bi_2Te_3+PbTe+SiGe reaches 18.2%, implying an improvement of 28% as compared to 2-segment unicouple (14.2%) of *p*-leg $Bi_{0.6}Sb_{1.4}Te_3$+SiGe and *n*-leg Bi_2Te_3+SiGe. The 3-segment unicouple with the highest calculated efficiency is found by segmenting $Bi_{0.6}Sb_{1.4}Te_3$+PbSrTe+SiGe as *p*-leg and either segmenting Bi_2Te_3+PbTe+$Si_{0.78}Ge_{0.22}$ or Bi_2Te_3+*n*-Skutt.+La_3Te_4 as *n*-leg. Bi_2Te_3+$CoSb_3$ and Bi_2Te_3+*n*-Clathrate can offer similar efficiencies for unicouples whose *p*-legs are the same and *n*-legs are segmentations from either one of these two materials with $Si_{0.78}Ge_{0.22}$ at the uppermost hot side.

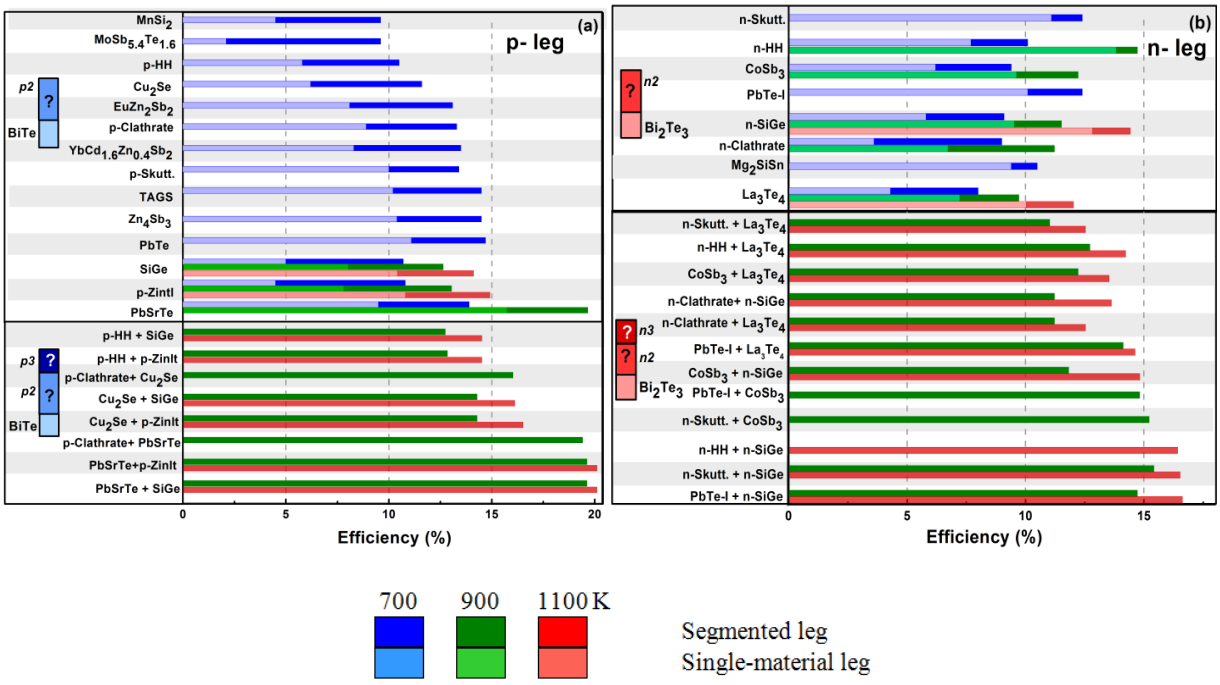

Figure 3-3 Efficiency of *p*- and *n*- segmented and non-segmented TE legs. (Note: for 3-segment legs, "single leg efficiency" is the efficiency of the whole segmented leg). **Abbreviations:** ***p*-HH:** $Hf_{0.5}Zr_{0.5}CoSb_{0.8}Sn_{0.2}$ **; *p*-Clathrate:** $Ba_8Au_{5.3}Ge_{40.7}$ **; p-Skutt.:** $NdFe_{3.5}Co_{0.5}Sb_{12}$ **; PbSrTe:** PbTe-SrTe**; TAGS:** $((AgSbTe)_{0.15}(GeTe)_{0.85}$ **; *p*-Zinlt:** $Yb_{14}Mn_{0.2}Al_{0.8}Sb_{11}$**; *n*-HH:** $Ti_{0.5}(Zr_{0.5}Hf_{0.5})_{0.5}NiSn_{0.998}Sb_{0.002}$ **; *n*-Clathrate:** $Ba_8Ga_{16}Ge_{30}$ **; *n*-Skutt.:** $Ba_{0.08}La_{0.05}Yb_{0.04}Co_4Sb_{12}$

Table 3-2 Efficiency of unicouples at T_h = 700 (blue), 900 (green) and 1100 K (red) made by legs of different *p*-type legs (rows) and *n*-type legs (columns). The legs are made by 2 segments (Table 3-2) or 3 segments (Table 3-3) with the segment at the cold side being fixed to be bismuth telluride. The red highlights mark the highest efficiencies

T_h = 700 K T_h = 900 K T_h = 1100 K

*p*2 ? / BiTe *p*-leg ↓ ; ? *n*2 / BiTe *n*-leg →	n-Skutt.	n-Clathrate	$CoSb_3$	La_3Te_4	PbTe	SiGe	n- HH	Mg_2SiSn
p-Clathrate	12.7	11.7	11.2	10.8	13.4	11.6	12	12.2
Cu_2Se	10.6 13.0	10.1 12	9.4 10.3	9.7 11.7	11.6	10 11.7	10.4	10.6
$EuZn_2Sb_2$	12.0	11.1	10.6	10.2	12.7	11	11.4	11.6
p-HH	11.1	9.8 11.7	9.8 12.2	8.8 9.4	11.3	9.8 11.9	10.3	10.5
$MoSb_{5.4}Te_{1.6}$	10.8	9.2 10.6	9.4 11.5	8.1 8.2	10.8	9.3 11	9.8	10
$MnSi_2$	9.9 10.7	9.3 10.7	8.9 10.2	8.8 9.6	10.6	9.2 10.8	9.7	9.9
PbTe	12.8	11.7	11.2	10.7	13.3	11.6	12	12.3
PbTe-SrTe	12.3	11.6 15.2	10.9 14	10.8 13.5	13.1	11.4 14.8	11.7	12
SiGe	11	9.9 11.7	9.7 11.8	9.0 9.7 11	11.4	9.9 11.9 14.2	9.8	10.6
p-Skutt.	12.8	11.0	11.1	9.6	12.8	11	11.5	11.7
TAGS	13.0	11.8	11.4	10.6	13.5	11.7	12.1	12.3
$YbCd_{0.6}Zn_{0.4}Sb_2$	12.2	11.2	10.7	10.4	12.9	11.1	11.5	11.8
ZinIt	9.8	9.5 10.9	8.7 9.2	9.3 11.1 13.5	10.9	9.4 10.6 12.5	9.8	10
Zn_4Sb_3	11.9	11.4	10.5	10.9	13	11.2	11.5	11.8

Table 3-3 Efficiency of unicouples at T_h = 700 (blue), 900 (green) and 1100 K (red) made by legs of different *p*-type legs (rows) and *n*-type legs (columns). The legs are made by 3 segments with the segment at the cold side being fixed to be bismuth telluride. The red highlights mark the highest efficiencies.

p-leg ↓ / *n*-leg →	n-Skutt. + SiGe	n-Skutt. + $CoSb_3$	n-Skutt. + La_3Te_4	PbTe + SiGe	PbTe + $CoSb_3$	PbTe+ La_3Te_4	n-Clathrate + La_3Te_4	n-Clathrate + SiGe	n- HH + La_3Te_4	n- HH + SiGe
p-Clathrate + Cu_2Se	13.6	13.4	13.4	14.9	14.5	14.8	13.2	13.2	13.5	13.7
p-Clathrate + PbTe-SrTe	15.8	15.7	15.6	16.6	16.5	13.7	15	15	15.2	15.6
PbTe-SrTe + Zinlt	16	15.9	11.9	16.8	16.7	16.6	15.2	15.2	15.4	15.8
	16.5		14.1	17.7		17.4	16.6	16.6	16.9	16.9
PbTe-SrTe + SiGe	16	15.9	15.7	16.8	16.7	16.6	15.2	15.2	15.4	15.8
	17.6		18.2	18.2		16.7	16.2	16.9	16.9	17.7
Cu_2Se + SiGe	12	11.8	11.2	13.6	13.0	13.7	12	12	12.2	12.3
	14.6		14.7	15.6		15.3	14.3	14.4	14.9	14.9
Cu_2Se+ Zinlt	12	11.8	11.9	13.6	13.0	13.7	12	12	12.2	12.3
	13.5		14.2	14.9		15.5	14.1	13.8	14.6	14
p-HH + Zinlt	11.7	13.8	11.7	13.3	13.7	12.7	11.7	11.7	12.6	13.1
	14.1		13.1	15.5		13.4	13.1	14.1	14.1	15.3
p-HH + SiGe	11.7	13.7	11.7	13.2	13.7	12.6	11.7	11.7	12.5	13.1
	13.9		12.6	15.3		12.7	12.6	13.9	13.7	15.3

Besides the requirement of high efficiency, consideration on the practical aspects of material choices is inevitable when designing segmented unicouples. The combinations that give the highest efficiencies are made from materials that are toxic (such as telluride and lead), expensive (gold and telluride) or facing the issue of low supply (tellurides) [165]. For this reason, other materials that are relatively inexpensive (e.g. half-Heusler alloys, silicides) [166] and environmental-friendly (e.g. silicides and oxides) [158] are becoming more and more important despite their lower efficiencies. Figure 3- 4 displays the most promising segmented unicouples with possible high efficiencies. From Figure 3- 4, it is clear that there exist many materials combinations resulting in an improved unicouple efficiency of over 10% upon the hot side temperature at 700, 900, and 1100 K. At T_h = 700 K, the unicouple with segmented *p*-leg $Bi_{0.6}Sb_{1.4}Te_3$+TAGS and *n*-leg Bi_2Te_3+PbTe yields the highest efficiency of 13.5%. Unicouples built based on segmenting silicides with bismuth tellurides can achieve a calculated efficency of 10.5%. With segmented half Heusler-based unicouples, the calculated efficiency is 11.5%. At a hot side temperature of 900 K, the highest calculated efficiency, 15.3%, belongs to the segmented unicouple from *p*-leg $Bi_{0.6}Sb_{1.4}Te_3$+PbSrTe+Zintl and *n*-leg Bi_2Te_3+PbTe+$Si_{0.78}Ge_{0.22}$. Increasing the hot side temperature to 1100 K, the efficiency can reach

the highest value of 18.2% for unicouples of *p*-leg $Bi_{0.6}Sb_{1.4}Te_3$+PbSrTe+SiGe and *n*-leg either of Bi_2Te_3+PbTe+SiGe or Bi_2Te_3+PbTe+La_3Te_4.

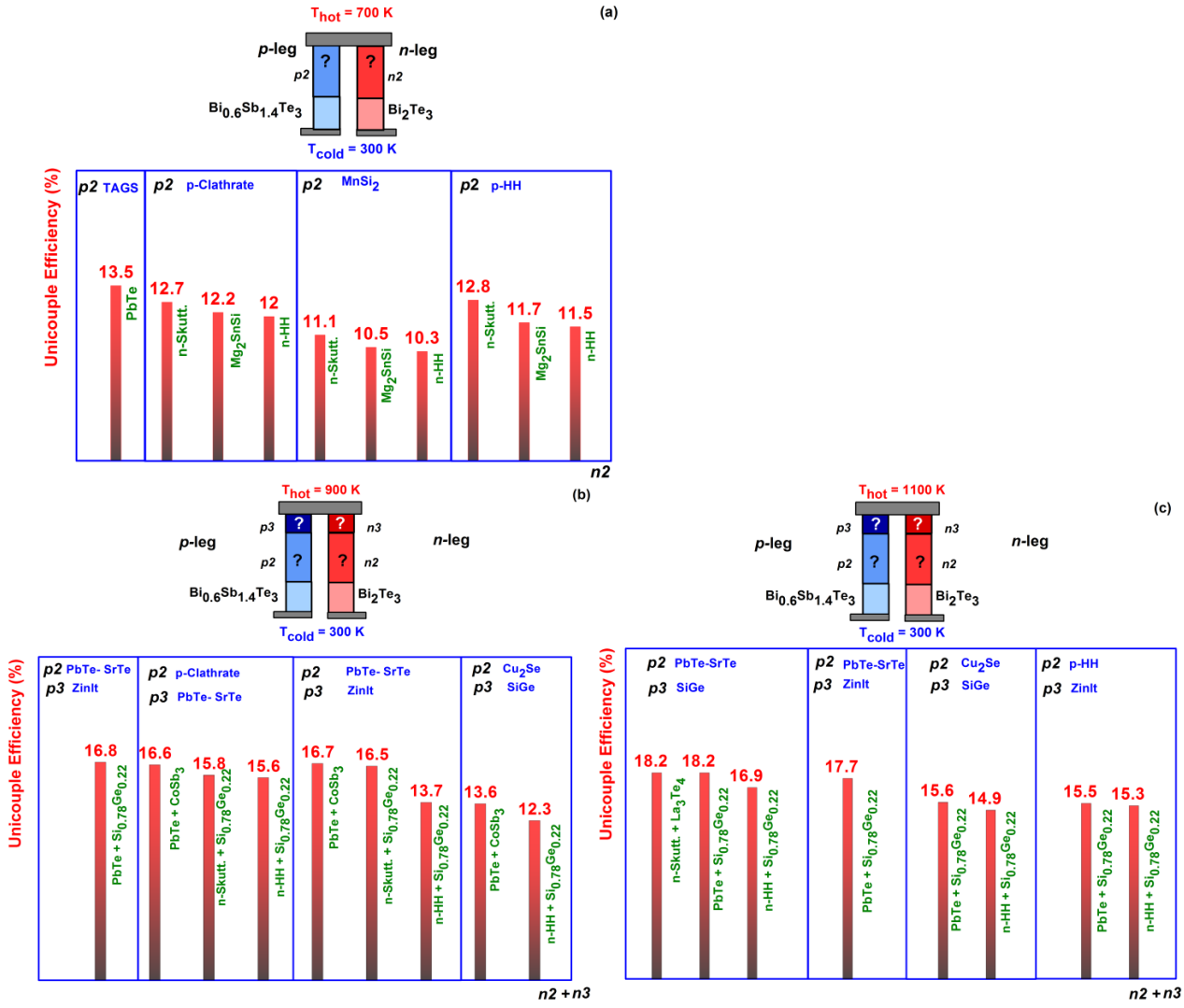

Figure 3-4 Selected segmented unicouples in working temperature ranges 300 – 700 (a), 900 (b), 1100 K (c)

3.4 Summary

The efficiency of different segmented thermoelectric single legs and unicouples comprising of two or three state-of-the-art materials for each leg was calculated. At T_c = 300 K and T_h = 700 K, the most efficient unicouple was found to be 13.5 % in which the unicouples were *n*-leg Bi_2Te_3+PbTe and *p*-leg $Bi_{0.6}Sb_{1.4}Te_3$+TAGS ($(AgSbTe)_{0.15}(GeTe)_{0.85}$). At T_c = 300 K and T_h = 900K the *p*-leg $Bi_{0.6}Sb_{1.4}Te_3$+Clathrate+PbTe-SrTe with *n*-leg Bi_2Te_3+PbTe+SiGe unicouple has the highest efficiency of 16.6 %. At 1100K, the highest calculated efficiency is 18.2% which belonged to *p*-leg $Bi_{0.6}Sb_{1.4}Te_3$+Clathrate+PbTe-SrTe+SiGe and *n*-leg of either Bi_2Te_3+PbTe+SiGe or Bi_2Te_3+Skutterudite+La_3Te_4 unicouples. Segmentation can provide significant improvements in

efficiency. However segmentation may also decrease the efficiency if incompatible materials are used.

4 Chapter 4 - On the challenges of reducing contact resistances in half-Heusler alloys-based thermoelectric generators

Abstract

As concluded from chapter 3, segmented thermoelectric generator based on half-Heusler and bismuth telluride could give a promising efficiency of 10.3 % under working temperature span 300 – 900 K. Thus, development of TEG from the materials is the focus of the thesis. It is acknowledged that contact resistance play a crucial role in realizing the performance of TEG from TE materials. Especially at high temperature of the hot side, a good and stable contact between TE materials and electrode is critical requirement. In this work, a method using fast hot pressing to join half-Heusler (HH) thermoelectric materials directly to an electrical current collector (Ag-electrode) without using a third filler material is introduced. The compositions of HH alloys are $Hf_{0.5}Zr_{0.5}CoSn_{0.2}Sb_{0.8}$ and $Ti_{0.6}Hf_{0.4}NiSn$ for the *p*- and *n*-type, respectively. With this method, the quality of contact between HH and electrode is improved resulting from their low electrical contact resistance and less reaction/diffusion layer at the interfaces. The microstructure and the chemical composition of the joints were examined using a scanning electron microscope (SEM) equipped with X-ray energy dispersion analysis (EDS). The electrical characteristics of the interfaces at the contacts were studied with electrical contact resistance and Seebeck scanning microprobe measurements. In this paper, we show that joining the HH to an Ag-electrode directly using fast hot pressing resulted in a lower contact resistance and better performance compared to the method of using active brazing filler alloy.

The work discussed in this chapter is submitted to Journal of Electronic materials. Pham Hoang Ngan, Ngo Van Nong, Le Thanh Hung, Benjamin Balke, Li Han, Ellen Marie Jensen Hedegaard, Søren Linderoth, and Nini Pryds.

4.1 Introduction

Energy conversion efficiency of a TEG is determined by two important factors: the thermoelectric properties of its TE materials and the temperature difference between the hot and cold side of the generator. The latter is directly related to the quality of the contact between TE elements and electrodes [96]. Criteria for a good contact are mechanical and chemical stability during operation and a low value of area specific electrical contact resistance (R_{ASC}) as well as the thermal resistance at the interface between the joint materials. The requirement for R_{ASC} is that it should be as low as possible so that the thermal and electrical losses across the contact interface are negligible. A quantified standard for an acceptable contact resistance varies depending on the type of specific materials used. For example, a $CoSb_3$/Cu system requires R_{ASC} of maximum 0.5×10^{-8} Ωm^2 [48], while SiGe-based TEGs require a typical R_{ASC} lower than 0.2×10^{-8} Ωm^2 [29]. Another requirement for a good contact is that the ratio between the total contact resistances and the resistance of the whole thermoelectric module should be around value of 0.1 [1], [167].

Thermoelectric generators working at low temperature ranges (below 473 K) have long been commercialized. However, the development of TEGs for use in higher temperature ranges (up to 973 K) is still limited [31], [167], [168]. Beside the challenge of developing high performance TE materials that can tolerate high temperature, another obstacle to overcome is to find a good contact material that forms a stable connection and has low contact resistance with the TE materials. Also, developing and improving the current joining techniques is needed.

HH alloys are promising TE materials for the medium-high temperature range, i.e. in the range of 473 to 973 K, both as *n*- and *p*-type materials. The materials are known for their high power factor due to their high electrical conductivity and Seebeck coefficient [169]. A drawback of these materials is their relatively high thermal conductivity compared to other TE materials. However, recent approaches which specifically target to scatter phonons by nanostructuring [170], [171], phase separating [172] increasing atomic mass and size differences [173] and multiple alloying [17], [174] can significantly reduce the intrinsic thermal conductivities of the HH alloys. Using these approaches, figure of merits, zT, higher than 1 at 973 K for these materials have already been reported [172], [173], [175]. In addition, these materials are environmentally friendly and have the advantages of moderate cost of the constituent elements [176].

Due to the above positive features, HH-based TEGs have recently drawn much research activities to improve their performances [31], [49], [58], [168], [169], [176]–[178]. Most of these reports, however, do not discuss the contacts between TE materials and electrodes and reports on investigating the joining between TE - HH and electrodes are rare [179]. Often, due to its low cost, Cu is used as an interconnect material [57], [58], [169], [176]–[178], with one exception in the work of Sascha Populoh et al. [176] where Ag was used as the electrode material. In fact, in atmospheric

environment, Cu starts to oxidize already at 623 K [180], [181]. This makes the Cu interconnector not suitable for high temperature applications or only suitable for systems where air-exposure is limited. Moreover, the oxidation of Cu degrades the output performance of a TEG already at 873 K has been reported [62]. Other types of inexpensive contact materials such as ferritic stainless steel have also been investigated [49], but with high R_{ASC} of ~ 66×10^{-8} Ωm^2. On the other hand, with the exceptions of gold and platinum, Ag has the highest electrical and thermal conductivity and stability at elevated temperature. Nevertheless, although Ag is more expensive than Cu, the performance of Ag makes it a reliable and potential candidate for applications in ambient condition at temperatures higher than 873 K.

A very common technique to join TE material in general and HH alloys in particular is using a soldering or brazing alloy such as Ti [62], Sn–37Pb and Sn–4Ag–0.5Cu [182], etc. [48], [183]–[187]. Stacked structures of electrode/solder or brazing alloy/TE material is pressed and heated until the solder or brazing alloy is melted and wets the electrode and the TE material to form a good connection between them. In this method, at the joining interface, the appearance of newly formed interphases consisting of elements in solder/brazing alloy, TE material and electrode, is inevitable. This interlayer, in many cases, e.g. the reaction layer between Ti and $CoSb_3$, interface between Ni/TE silicides [186], [187], causes high contact resistance which increase with time. Therefore, reducing the electrical contact resistance and avoiding the undesired influence of the interlayer become challenges to obtain high performance TEG.

In this work, Ag was selected as contact material with HH-TE elements and a new and simple joining technique by fast hot pressing is developed. To compare this approach with the conventional joining method, a joint structure of HH and Ag electrode was also made by using brazing filler alloy such as Incusil ® ABA ^{TM}. The microstructural and chemical stability of the contact made by these approaches were then evaluated and compared. Their electrical properties were also studied through the contact resistance measurement and the Seebeck coefficient scanning probe.

4.2 Experimental

4.2.1 Sample preparation

p- and *n*-type HH thermoelectric alloys, whose compositions were $Hf_{0.5}Zr_{0.5}CoSn_{0.2}Sb_{0.8}$ and $Ti_{0.6}Hf_{0.4}NiSn$, respectively, were prepared by arc melting, powderizing, then consolidating by spark plasma sintering. The detailed material processing is described in Chapter 2.

Pellets of *p*- and *n*- type HH obtained after sintering were cut into rectangular shaped samples, $5 \times 5 \times 8$ mm^3. The surfaces of the samples were polished and cleaned. Polished samples of *p*- and *n*-type HH were ultrasonicated in acetone, isopropanol and de-ionized water, followed by carbon

dioxide snow cleaning. After having surfaces cleaned, *p*- or *n*-type HH alloys were joined with the Ag electrode in two different ways: (1) HH/Ag(foil)/HH and (2) HH/(filler-Incusil)/Ag/(filler-Incusil)/HH (see Figure 4-1).

Figure 4-1 Schematic structure of prepared samples joined between *p*- and *n*- HH with Ag directly by fast hot pressing (left) and by brazing with Incusil® ABA TM as filler (right).

Since the HH alloys are expected to be used in applications with high hot side temperatures up to 973 K, joining materials must be sustainable under these conditions. At the same time, the processing temperature of the materials should be maintained below 1073 K to avoid detrimental changes in the TE properties, e.g. Sb, Sn sublimations or material oxidation. Bulk HH was joined directly to Ag foil by applying a pressure of 40 MPa at temperature of 1053 K and under vacuum.

In the second joining method, brazing filler alloy of Incusil®ABA™ (Wesgo) ($Ag_{59}Cu_{27.3}In_{12.5}Ti_{1.3}$) in the form of foil was used. The foil was sandwiched between the Ag foil and *p/n*-type HH bulk (shown in Figure 4-1a) and the whole structure was then put into a graphite holder and loaded into the spark plasma sintering chamber. The joining process was carried out under a pressure of 40 MPa in vacuum at a temperature of 1053 K using the modified SPS method described above.

4.2.2 Sample characterization

The electrical resistivity and the thermopower measurements of the as-prepared materials in the temperature range of 303 to 973 K have been studied using ZEM 3 while the thermal conductivity at the same temperature range have been measured using laser flash LFA 475 (results are not shown here). The TE measurements were done to confirm the quality of the TE samples after the preparation. Thermal expansion coefficients of the materials used for joining were measured using a Netzsch DIL 402 C dilatometer.

Microstructural and electrical properties of the joining interface have also been studied. The microstructure of the interfaces and the distributions of elements of the as-prepared joint were evaluated by scanning electron microscopy and energy dispersive X-ray spectroscopy (Zeiss Supra-35). Also, as-prepared sandwich samples were cross-cut into bars of 2 × 2 × 8 mm^3 for the measurements of the contact electrical resistivity. In order to understand the influences of the additional phases and identify their influences on thermopowers at the interfaces, the Potential

Seebeck microprobe (PSM by Panco Gmbh) was used to scan across the joining interface. The contact resistance measurements were done by a four-probe method described elsewhere [49].

4.3 Results and discussion

4.3.1 Thermal expansion coefficient

Mismatches in thermal expansion of layered structures are the primary reason for their delamination. The similarity in coefficients of thermal expansion is an important criterion to select suitable electrodes for TE materials [48], [49], [184]. In this work, the thermal expansion coefficients of *p*-type $Hf_{0.5}Zr_{0.5}CoSn_{0.2}Sb_{0.8}$ and *n*-type $Ti_{0.6}Hf_{0.4}NiSn$ were measured to be about $2 \times 10^{-5}\ K^{-1}$ and $1\times10^{-5}\ K^{-1}$, respectively at 373 K and increased by 25% at 973 K in the case of *p*-type HH (Figure 4-2). The thermal expansion coefficient of the *n*-type HH is about two times lower than those of *p*-type HH, as well as the silver and the active brazing alloy (Incusil), which are reported to be $1.9 \times10^{-5}\ K^{-1}$ [188] and $1.8 \times10^{-5}\ K^{-1}$[189], respectively. At room temperature, the elastic modulus of Incusil and Ag are 76 GPa [188] and 83 GPa, respectively and could be able to relax the strain caused by the thermal expansion coefficient mismatches between them and the TE materials [48].

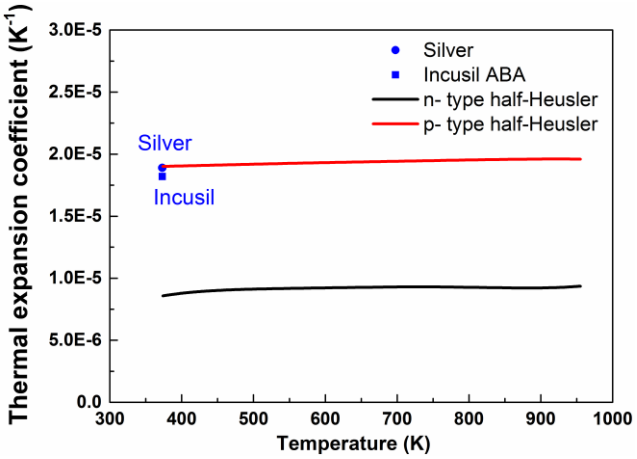

Figure 4-2 Thermal expansion coefficients of *p*- and *n*-type HH, Silver [188] and Incusil® ABA™ [189]

4.3.2 Microstructures, chemical distribution and Seebeck micro-scanning at the joining interface

5 Figure 4- 3 shows microstructures, EDS analysis and the joining interfaces between *p*-type HH with an Ag electrode, Incusil® ABA™ (B, D). In the process where HH was joining, the interface between the two materials shows good delamination (Figure 4-3A). From the EDS line scan image, the formation of an inter-diffusion layer with thickness of less than 1 µm is observed (Figure 4-3 B). The EDS line-scan analysis across the interface region shows regions rich in Ag, Hf and Zr. The element composition of the newly formed region at the interface is shown in Appendix

Table 7-1 (in the Appendix). The observed increase in concentrations of Zr and Hf can be attributed to the formation of an interphase containing these elements with Ag during the processing of the joining. Corresponding to their phase diagrams, Ag could react with Zr and Hf and forms the phases of AgZr and $AgHf_2$ at temperatures of 973 K [190] and 1073 K [191], respectively.

In the case of joining *p*-type HH and an Ag electrode by using Incusil, the joining interface between HH and Incusil showed clear air gap region between these materials whose width was ~ 1 µm (Figure 4-3 D). From the analysis of the SEM and the EDS line scan (Figure 4-3 E), it is worth noticing that a formation of a 5 µm-thick Ti region located at 20 µm from the HH region was also observed. Under joining conditions, temperature of 953 K, the Ag, Cu and In elements may have a tendency to form interphases according to their ternary phase diagram, i.e. an interphase containing

Ag, Cu_4In and a small amount of Ag_3In [192]. Ag and Ti are immiscible below 1023 K and do not form any phases in this range of temperatures [193]. Cu and Ti can form a Cu_4Ti phase above 473 K [194], while Cu and In can already form interphase at temperatures below 473 K [195]. Indium starts to react with Ti to form In_5Ti_2 from 429 K, while the reaction with Ag to form Ag-In happens at 417 K [196]. As a final consequence of these competing processes, the formation of interphases between Ag, Cu and In are faster than that of Ti-phases and thus Ti has a tendency to be separated to form pure elements as also observed in these experiments. The same phenomenon was observed in [184] and in order to prevent this phase separation, longer holding time of the brazing process is suggested. For more details, element composition analyses are shown in Table 8-2 in the Appendix.

Scanning images of the Seebeck coefficient at the interfaces are shown in Figure 4-3 C and F. A clear continuity between the TE material and the electrode indicated a good contact and no obvious inter-diffusion. The measured values for the HH segment were 80 – 100 μVK^{-1}, which is slightly lower than those values measured by ZEM 3 (not shown here). The difference is reasonable and within the error bars of the measurement. The observable changes of the interphases at the intermediate region between *p*-type HH/ Ag and Incusil from SEM image (Figure 4- 3 A-B), is not obvious in the Seebeck coefficient scanning images (Figure 4-3 C, F) due to the limited resolution of the probe size which is on the order of 50 μm. With this probe size resolution, within the area of 0.1 mm from the joining interface, it is reasonable to conclude that the thermopower of *p*-type HH were not detrimentally influenced by the process parameters.

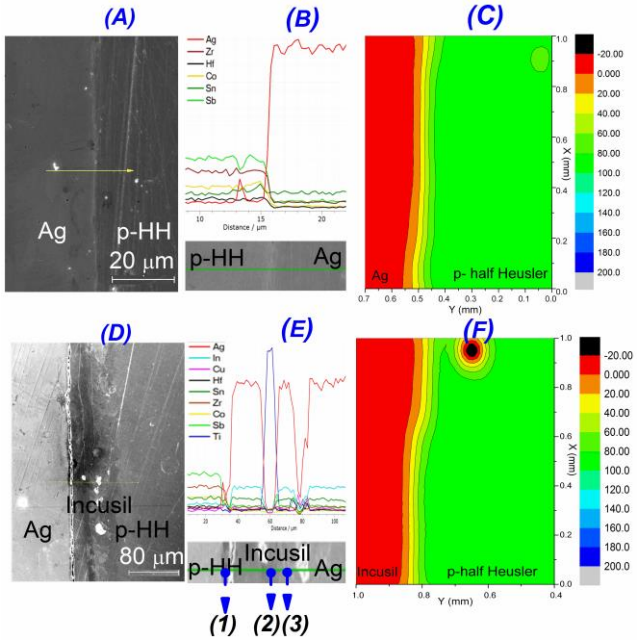

Figure 4-3 Microstructures, chemical analysis and Seebeck microprobe scanning at the joining interfaces between *p*-type HH with Ag electrode, joining without (*A*, *B* and *C*, respectively) and with filler Incusil® ABA ™ (*D*, *E* and *F*, respectively)

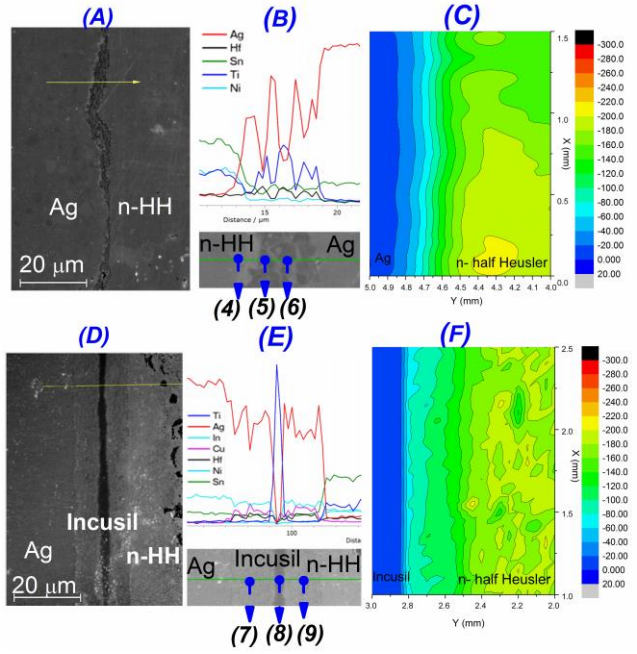

Figure 5-4 Microstructures, chemical analysis and Seebeck microprobe scanning at the joining interfaces between *n*-type HH with Ag electrode, joining without (*A*, *B* and *C*, respectively) and with filler Incusil® ABA ™ (*D*, *E* and *F*, respectively).

In the case of *n*-type HH, analyses on microstructures and element distribution at the joining interface and the Seebeck microprobe scanning results are shown in Figure 5-4. The direct joining process resulted in an intermediate region of 5 μm between *n*-type HH and Ag (Figure 5-4 A). From

the EDS line scan analysis (Figure 5-4 B), there was a distinct difference between the regions rich in Ti and Ag at the joining interface and the inhomogeneity of the Incusil layer. This separation may be due to the fact that at a temperature below 1473 K, there are no intermediate phases which can be formed by Ag and Ti [193]. The increase in Sn and Hf concentrations corresponds to the increase of Ag and Ti, respectively and can be correlated to the formation of TiHf and Ag_3Sn phases after the joining process takes place. The TiHf and Ag_3Sn phases formed at temperatures above 973 K and 493 K, respectively [197], [198]. In the case where the filler Incusil was used, there was no observation of cracks at the interface even after heat treatment. However, from the SEM images and EDS line-scan analysis (Figure 5-4 D and E), the inhomogeneity of the Incusil layer is obvious. Remarkably, a high concentration of Ti formed at a region of about 10-μm located inside the Incusil layer as well as along the joining interface was observed. On the scale of 50 μm, the influence of the thermopower inhomogeneity on materials' was not observed.

5.1.1 Electrical contact resistance

The quality of the joining process is also evaluated by the area specific contact resistance of the joints. Figure 5-5 A-B shows the specific contact resistance of HH/Ag and HH/Incusil. The measured area-specific contact resistance of the *p*-type HH/Ag junction is found to be stable and in the range of $0.38 \times 10^{-8}\ \Omega m^2$ at temperatures below 723 K. Above 723 K, this value increased to $0.89 \times 10^{-8}\ \Omega m^2$. For the *n*-type HH and Ag, however, the contact resistance was much higher at a value of $3.39 \times 10^{-8}\ \Omega m^2$ at 303 K and decreased to $0.91 \times 10^{-8}\ \Omega m^2$ at 773 K. These results for the *n*-type correspond well with the formation of secondary phases which increase the value of the contact resistance.

As for the *n*-type material, area-specific contact resistances of the joints are shown in Figure 5-5B. The measured R_{ASC} of an *n*-type HH/Incusil interface decreases from $10 \times 10^{-8}\ \Omega m^2$ at room temperature to $0.5 \times 10^{-8}\ \Omega m^2$ at 773 K. The R_{ASC} of *p*-type HH/Incusil, on the other hand started with a value of $0.25 \times 10^{-8}\ \Omega m^2$ and increased to $1.5 \times 10^{-8}\ \Omega m^2$ as the temperature increased to 773 K. In the cases of using Incusil, the resulting R_{ASC} values were higher than in the case without Incusil. Furthermore, the use of Incusil indicated the formation of a variety of interphases at the joining interface. The formation of these phases was probably the main reason for the high contact resistance measured in comparison with the case of joining without Incusil. The same explanation could be applied to the case of *n*-type HH, where more interphases were observed. For the *n*-type HH, when increasing the temperature, the carriers gained more thermodynamic energy to overcome these barriers, thus the contact resistance decreased with increasing temperature. However, in the case of *p*-type, the formation and expansion of the air gap causes an increase of the contact resistance with increasing temperature.

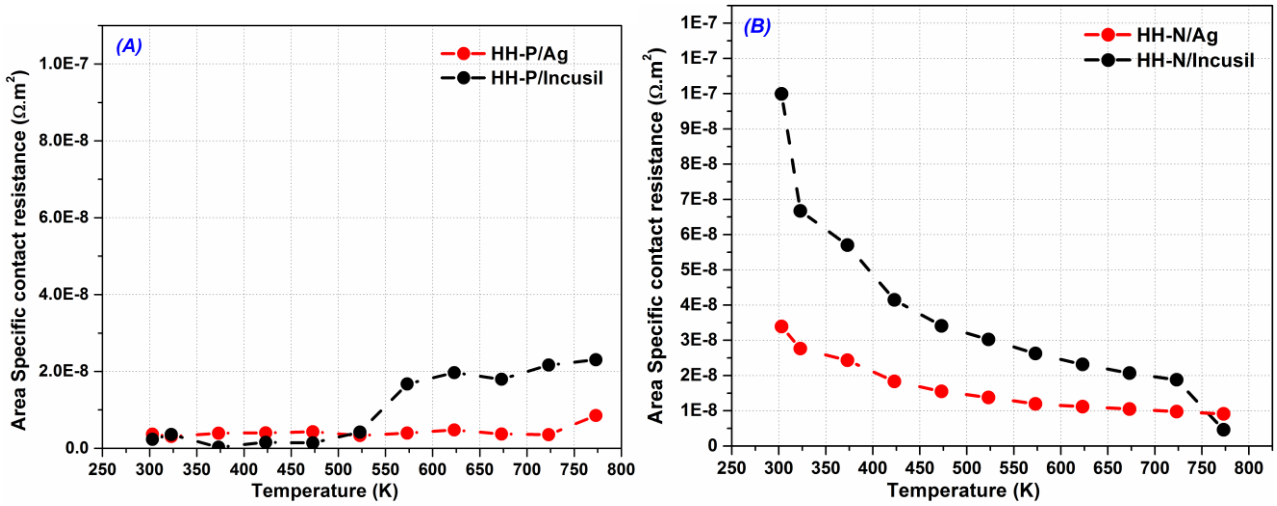

Figure 5-5 Area specific contact resistance as a function of temperature for *p*- (A) and *n*-type (B) HH alloys with Ag and Incusil.

5.1.2 Evaluation of the contact resistance's influence on thermal conversion efficiency

To evaluate how the obtained contact resistance could influence the performance of a TEG built from these *p*- and *n*-HH materials, we have calculated the conversion efficiency of a single-pair of *p*-*n* HH under different conditions: perfect contact (zero contact resistance) and with contact resistances as in the case of using Ag and Incusil as a filler. The details of the calculation model are described elsewhere [31], [167]. In this calculation, the modelled TEG was set to be 323 K at the cold side and 873 K at the hot side. Figure 5-6 shows the calculated maximum efficiency as a function of the resistance ratio (δ), which is the ratio between the resistance of the contact (R_c) and the total resistance of the unicouple. It is clear that the conversion efficiency decreases rapidly as the contribution of the contact resistance increases. Under ideal conditions i.e. $\delta = 0$, the maximum efficiency was about 5.5%. In our work, the ratio of contact resistance to total unicouple's resistance δ was 0.14 and 0.48, respectively, for the direct method using Ag and indirect method using Incusil filler. The joining process with Ag reduced maximum efficiency from 5.5% to ~4.7%, which is a relatively small decrease. The efficiency reduced to 2.5% when Incusil was used.

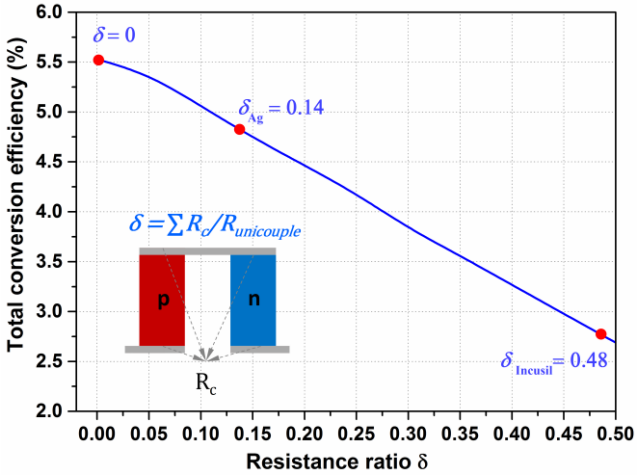

Figure 5-6 Calculated efficiency degraded by obtained contact resistance

In short, the joining process of HH with Ag without using Incusil resulted in the formation of fewer interphases at the interface and lower electrical contact resistance compared with the process using Incusil. The contact resistances obtained in both processes could be further reduced if a buffer layer of several micrometers thickness were carefully chosen and deposited on the TE material's surface prior to the joining step. The deposited buffer layer can fill up micro voids and smooth the surface fracture of elements to be joined, thus enhance the contact between joining materials, hence the reduction of R_{ASC} is possible. From the analyzed results, we suggest using Ag as a buffer layer. To the best of our knowledge, low contact resistance of less than 0.2×10^{-8} Ωm^2 has been obtained mostly in joining procedures including a thin metal layer deposition on TE materials surface before joining [183], [185], [199]. In some cases, e.g. where bismuth telluride was used as TE material, these buffer layers prevent diffusion and therefore the formation of unwanted phases [62], [200], [201]. When a buffer layer was excluded, extremely high contact resistances were obtained, for example, values of 110×10^{-8} Ωm^2 were measured [60]. The new method of joining directly HH with an Ag electrode allows us to avoid using a brazing filler alloy, simplifies the TEGs fabrication procedure and avoids the formation of unnecessary phases, which can deteriorate the performance of the contact.

5.2 Summary

In this study, a simple and direct method of joining a HH alloy with the electrode by fast hot pressing was successfully developed. Joining directly HH alloys with an Ag electrode resulted in minor formation of intermediate phases at the interface compared to joining by using Incusil as filler, and therefore lower contact resistance. Seebeck scanning microprobe measurements results at the junctions between TE materials and Ag or Incusil showed that both joining processes did not influence the thermopower of the HH alloy, at least not within the resolution of this technique. With the quality of the contacts obtained by the direct method, the efficiency of HH-based TEGs could

possibly reach a value of over 5% at the hot side and cold side temperatures of 873 and 323 K, respectively. In the future, further improvements to reduce R_{ASC} may be possible by making a thin metallic buffering layer on the TE materials' surfaces to reduce possible micro gaps caused by mismatch in surface as well as to minimize the reaction/diffusion layer.

6 Chapter 5 - On the joining of half-Heusler and Bismuth tellurides for segmented thermoelectric generators

Abstract

After developing a method to fabricate contact between TE material (half-Heusler) with electrode at hot side, the next step to develop segmented TEG is to join the TE materials together. The issue is addressed in this chapter. *p* - and *n*-type segmented legs based on bismuth tellurides and half-Heusler alloys were fabricated and characterized. Practical challenges to join these materials had been overcome and a two-step joining process was introduced. Half-Heusler was firstly joined with Ag by fast hot pressing, then with bismuth tellurides using solder alloy composed of 10 % Ag and 90% Sn (technical name $Ag_{10}Sn$ [202]), to form a segmented structure. The microstructural and thermoelectric properties of obtained segmented legs were investigated using SEM-EDS, Seebeck microprobe scanning and measurements of the contact resistance and thermoelectric properties as a function of temperature. Output power generating properties were characterized under various the hot side temperatures up to 873 K and the cold side kept at 323 K. The stability of the joints was also investigated under heat treatment and thermal cycling. The results obtained by experimental are compared with theoretical calculation using numerical modeling, and the source of the influence is discussed.

Part of this work is going to be submitted as manuscript with title ***Fabrication and characterization of n-type segmented leg of half-Heusler alloy and Bismuth telluride,*** Le Thanh Hung, Pham Hoang Ngan, Ngo Van Nong, and Nini Pryds.

6.1 Introduction

Although thermoelectric power generation has many advantages its conversion efficiency so far is still rather low. In order to improve the thermal conversion efficiency of TEG, segmentation of TE materials suitable for different working temperature interval has been demonstrated as an effective solutions [1], [30], [31], [203]. From the modeling result in chapter 3, it is predicted that the segmented leg of bismuth telluride and half-Heusler could reach a maximum efficiency of more than 10% at the hot side and the cold side temperatures of 900 K and 300 K, respectively. Bismuth tellurides are known as the best TE material in low temperature range (up to 473 K) [1], [2], [90], while half-Heusler alloys are very competitive materials suitable for medium-high temperature range up to about 873 K [6], [22].

Due to the fact that different TE materials often have different physical and chemical characteristics, joining them is considered as the most challenging part in segmented TEG fabrication [1], [107], [203]. As discussed in Chapter 1, joining process should result in high contact quality between the materials, which requires strong adhesion, good chemical stability and low contact resistance [107], [109], [203], [204]. With segmented TEG as in this work comprises of half-Heusler and bismuth telluride, joining between these segments has certain major challenges. Bismuth telluride is suitable to work at temperature until 523 K and cannot stand temperature above 773 K due to its volatile constituents: tellurides and antimony [90], [205]–[209]. Half-Heusler, however, is thermally stable materials with low wettability [210] melting point above 1773 K. According to D'Angelo and Börner et al. [184], [211], in order to directly join the materials, the temperature at their interface should be elevated to the range from 50 to 80% of the lowest melting point. Thus, in principle, bulks of half-Heusler and bismuth telluride cannot be joined directly together.

In this work, for the first time, segmentation of bismuth telluride to half-Heusler materials is investigated in details. This study addresses the mentioned practical challenges and introduces a two-step process to successfully join half-Heusler and Bismuth telluride materials. Segmented legs of half-Heusler (HH) and bismuth telluride (BiTe) in both *p* and *n*-type were prepared and characterized. The properties of the joining interface were first characterized. Interfacial microstructure of the join parts were studied using a scanning electron microscopy with energy dispersive X-ray analysis. The electrical properties of the samples were investigated through the contact resistance measurement and Seebeck scanning microprobe. Then, the thermoelectric properties of the segmented leg were measured by ZEM 3 to study the legs' resistivities and thermopower as a function of temperature. The next step was testing the thermoelectric output, including voltage, current and power, of obtained segmented legs with temperature span 873 – 323

K and cycling hot side temperature. Numerical calculation model was used to evaluate and analyses obtained results.

6.2 Experimental

6.2.1 Material preparation

p- and *n*-type half-Heusler (HH) thermoelectric alloys with nominal compositions $Hf_{0.5}Zr_{0.5}CoSn_{0.2}Sb_{0.8}$ and $Ti_{0.6}Hf_{0.4}NiSn$, respectively, were prepared following the process described in Chapter 2.

Bismuth tellurides (BiTe) ingots *p*- and *n*-types were purchased commercially and their TE properties were verified. The electrical resistivity and Seebeck coefficient of the materials were measured using ZEM 3 (ULVAC). The thermal conductivity measurement was done by laser flash LFA 475.

6.2.2 Segmentation of BiTe and HH

From the obtained ingots, BiTe and HH were cut into rectangular pieces to assemble into segmented TE leg with cross sectional area of 4 x 4 mm^2 and total length of 8 mm (Figure 5-1). The cross sectional area was limited by the graphite die size of the SPS 515S. The length of 8 mm was chosen to maintain the temperature gradient ~ 843 K subjected to the obtained segmented leg and suitable for further characterization steps. The surfaces of the samples were polished with sandpaper grit 200 for HH and 500 for BiTe and then cleaned before joining. Polished samples of *p*- and *n*-type HH were ultrasonicated in acetone, isopropanol and de-ionized water, following by carbon dioxide snow cleaning.

Half-Heusler alloys and bismuth tellurides were joined by using fast hot pressing technique. Details of the technique are described in Chapter 4 or reference [212]. As mentioned previously, the thermal stabilities of HH and BiTe are very different. We have made efforts to join HH to the BiTe in a single-step-process by using various joining materials chosen based on the requirement to minimize mismatch of thermal expansion coefficients. The thermal expansion coefficients (CTE) of BiTe is ~16.4 (Table 1-2, Chapter 1) and that of HH is ~13 (Chapter 4). Thus, the tried joining materials are solder alloys $Ag_{10}Sn_{90}$ (CTE = 22) or Cu (CTE = 16.5), Ni (CTE = 13), and Al (CTE = 22) [213], [214]. However the joining was not successful mainly due to the poor wettability of half-Heusler, which also encountered in ref. [215]. Thus, we introduce a two-step procedure to join HH and BiTe (Figure 5-1 a). First, HH was joined to Ag by hot pressing at 1053 K under pressure of 40 MPa and in vacuum (following the joining process described in Chapter 4). Then, the Ag surface on the joined HH/Ag structured was thoroughly cleaned. A foil of $Ag_{10}Sn_{90}$ solder alloy was placed on top of the cleaned Ag surface, followed by placing the BiTe element. In order to

minimize the influence of the solder material on the overall thermoelectric properties of the segmented leg but still maintain the function of the solder layer, the thickness of the solder foil was chosen to be 0.3 μm. The whole structure was loaded into a spark plasma sintering (SPS) chamber and processed at temperature of 493 K, under pressure of 30 MPa and in vacuum. These joining conditions were optimized based on the melting temperature of the solder alloy and the maximum load that BiTe can stand without being cracked. A costume alumina structure was design and used to prevent the current in the SPS to flow through the TE materials, which might be equally considered as a thermal treatment process that affects the TE properties of materials (see Chapter 2). For abbreviation, from now on solder $Ag_{10}Sn_{90}$ will be called with its technical name $Ag_{10}Sn$.

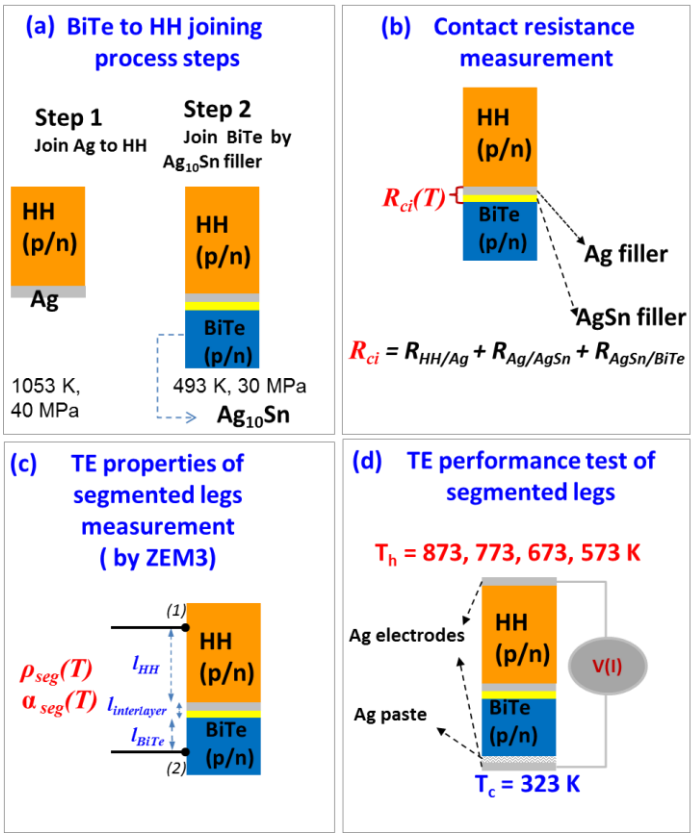

Figure 6-1 (a) Process to fabricate *p*- and *n*-type BiTe/HH segmented legs. (b) Illustration of contact resistance measurement of fabricated segmented legs. (c) Illustration of measurement to determine the total electrical resistivity and thermopower of obtained segmented legs. (d) Schematic of the thermoelectric output test of segmented legs.

6.2.3 Characterization of the as-joined interface.

The obtained joined sample was then cut into different pieces in cross sectional direction to analyze the microstructural and electrical properties across the joined layers. Microstructures and chemical distribution of elements at the joint was analysed by scanning electron microscopy and energy dispersive X-ray spectroscopy (Zeiss Supra-35). Thermopower of adjacent materials at the

joined interfaces was scanned by Seebeck scanning microprobe (Panco) as described in Chapter 2. The contact resistances of the joined samples were measured (Figure 5- 1 b) by using a 4-probe scanning method described also in Chapter 2. Characteristic techniques of the obtained BiTe/HH were carried out with increasing temperature from room temperature to 473 K due to the melting limitation of solder $Ag_{10}Sn$. In order to study the stability of the joint, the segmented legs were heat treated at 473 K for 48 hours in flowing nitrogen environment to prevent possible oxidation of BiTe and sublimation of tellurium and antimony (in *p*-type BiTe) (Chapter 1). After the heat treatment, the joined interface was characterized again.

6.2.4 Characterization of *p*- and *n*- BiTe/HH segmented legs

The electrical resistivity and Seebeck coefficient of the segmented leg, including the interface layer (Figure 5- 1 c), have been measured by using ZEM 3 (ULVAC). Finally, the legs were subjects to thermoelectric output test to investigate their voltage-current characteristics. The setup of the test is illustrated in Figure 5-1 d. Details of the test system is described in Chapter 2. Numerical calculation model was applied to calculate the thermoelectric outputs: voltage, current and the power of the fabricated segmented HH-BiTe legs. The calculated results were compared with measured data to evaluate the influence of the obtained contact resistance on the leg's performance. In this calculation, heat loss to the surroundings and the thermal contact at the interfaces were assumed to be zero. The hot and cold side temperatures for the legs are 873 K and 323 K. The measured thermoelectric properties of the *p*- and *n*-type BiTe and HH legs, electrical contact resistance at HH/BiTe interface as a function of temperature were used as the input parameters. First, the calculation was made for with zero electrical contact resistance. Then, the calculation was done with contact resistances measured at the hot side and the interface between BiTe and HH included.

6.3 Results and discussions

6.3.1 Thermoelectric properties of bismuth tellurides and half-Heusler materials

The electrical resistivity, Seebeck coefficient and thermal conductivity as a function of temperature for BiTe and HH *p*- and *n*- materials are shown in Figure 5- 2. As measuring temperature increasing, both *p*- and *n*-type BiTe show a metallic-like behavior of the electrical resistivity, similar to that of *p*-type HH. As for *n*-type HH, the electrical resistivity curve exhibits a semiconductor - like behavior. The absolute values of the Seebeck coefficient of both types of BiTe peaked at ~220 μVK^{-1} at a temperatures of ~ 373 K and ~ 423 K for *n*-type and at for *p*-type respectively. The Seebeck coefficient of *p*-type HH increased over the whole measured temperature range to a maximum value of 220 μVK^{-1} at 873 K. Meanwhile, the Seebeck coefficient of *n*-type HH increased to a value of 260 μVK^{-1} at 623 K it then decreased to 190 μVK^{-1} at 873 K. By

combining BiTe and HH, the average *zT* of *p*- and *n*-type segmented legs were calculated to be 0.4 and 0.5, respectively within the temperature range of 300 – 873 K.

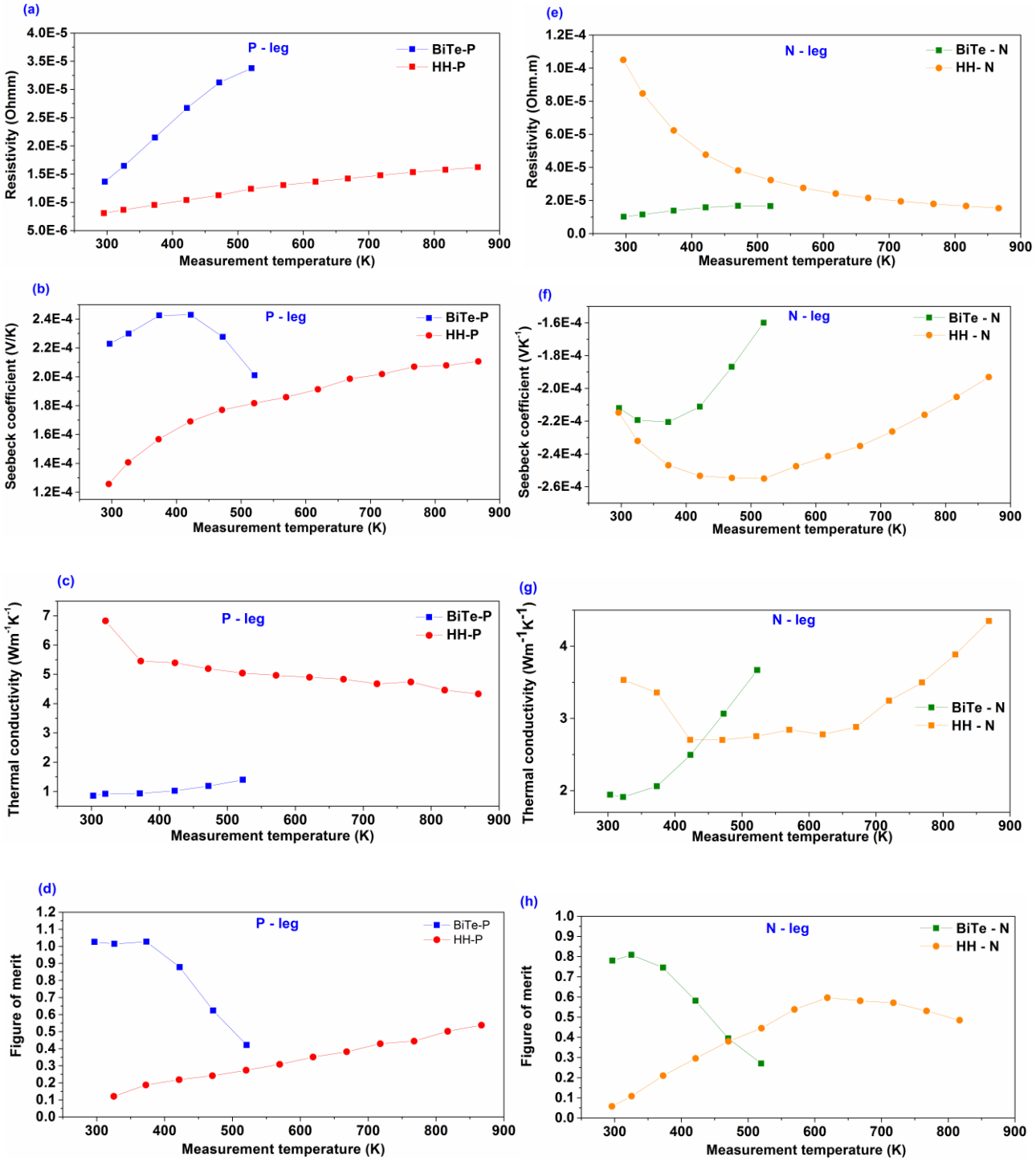

Figure 6-2 Thermoelectric properties of BiTe and HH in *p*- segmented leg (a-d) and *n*-segmented leg (e-h).

6.3.2 Interfacial microstructural and thermoelectric analyses

Microstructure and chemical analysis at the joining interface of the *p*- and the *n*-type segmented TE elements are shown in Figure 5-3. For both *p*- and *n*-type no sign of delamination and crack

between joining layers were observed. Inhomogeneities observed only inside the $Ag_{10}Sn$ solder layer. In both *p*- and *n*- type cases, EDS analysis shown that in the solder layer, there are regions of Sn- and Ag-rich phases (points (3) and (4) in Figure 5- 2(b) and 2(f)). Besides, a small amount of Sb was also detected in the solder layer, which might be the consequence of diffusion from bismuth tellurides to form an interphase with Sn in the solder. Towards the bismuth telluride parts, there was formation of intermediate region rich in Sn with thickness of ~10 μm, indicated the diffusion of Sn into BiTe, which was also observed in some other works [216]–[218]. The compositions of these interface regions were quantified in Table 5-1 (See Appendix).

After heat treatment, the expansion of interdiffusion layer between BiTe and solder alloy $Ag_{10}Sn$ is observable for the *n*-type leg. The total thickness of the interlayer, including $Ag_{10}Sn$/interdiffusion layers, increased from 40 μm before heat treatment to 60 μm after the heat treatment. EDS analysis of the interdiffusion layer showed that there is an tendency of Sn to diffuse into BiTe and form SnTe-rich phases. After 48 hours of heat treatment, the diffusion layer between BiTe and solder alloy had been expanded by 30 μm (from 10 to 40 μm). The diffusion coefficient D of Sn into BiTe can be estimated by applying the following simple relation $X = (Dt)^{½}$ [219], with X is the expansion of the interdiffusion layer and t is the heat treatment time. In the case of *n*-type segmented leg, $X \sim 30$ μm, $t = 48$ hours, thus $D \sim 5.2 \times 10^{-9}$ m^2s^{-1}. *p*-type segmented leg however, delaminated after the heat treatment. The delamination could be due to the fast diffusion of Sn into *p*-type BiTe that destroyed the solder layer [200], [220], [221]. Efforts to effectively resist the diffusion of the solder into BiTe have been made recently [221].

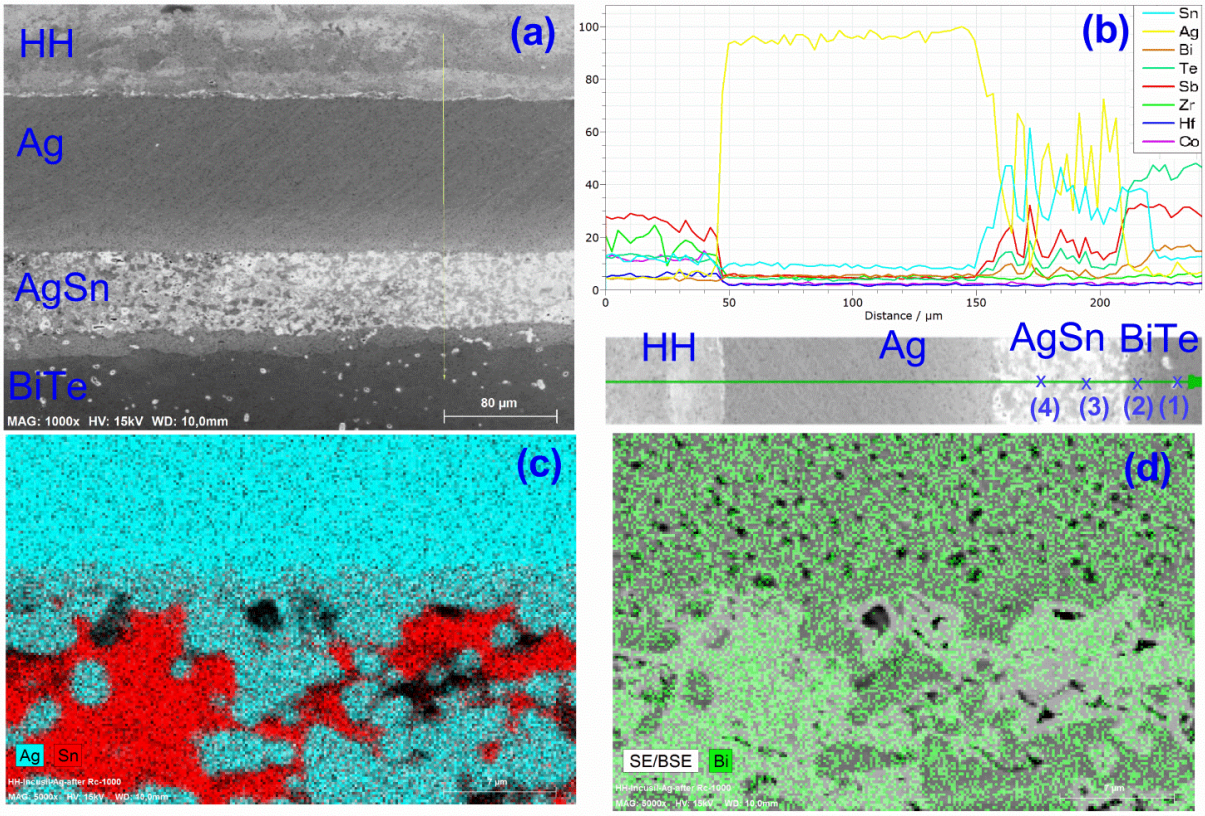

Figure 6-3 Microstructures and chemical analysis at the joint interface of *p*-type segmented leg before heat treatment: (a) SEM image of the interface, (b) EDS line scan across the interface, (c) Zoom-in image of Ag and Sn distributions, and (d) Zoom-in image of Bi distribution. After heat treatment, the leg delaminated, so no further microstructural analysis had been conducted.

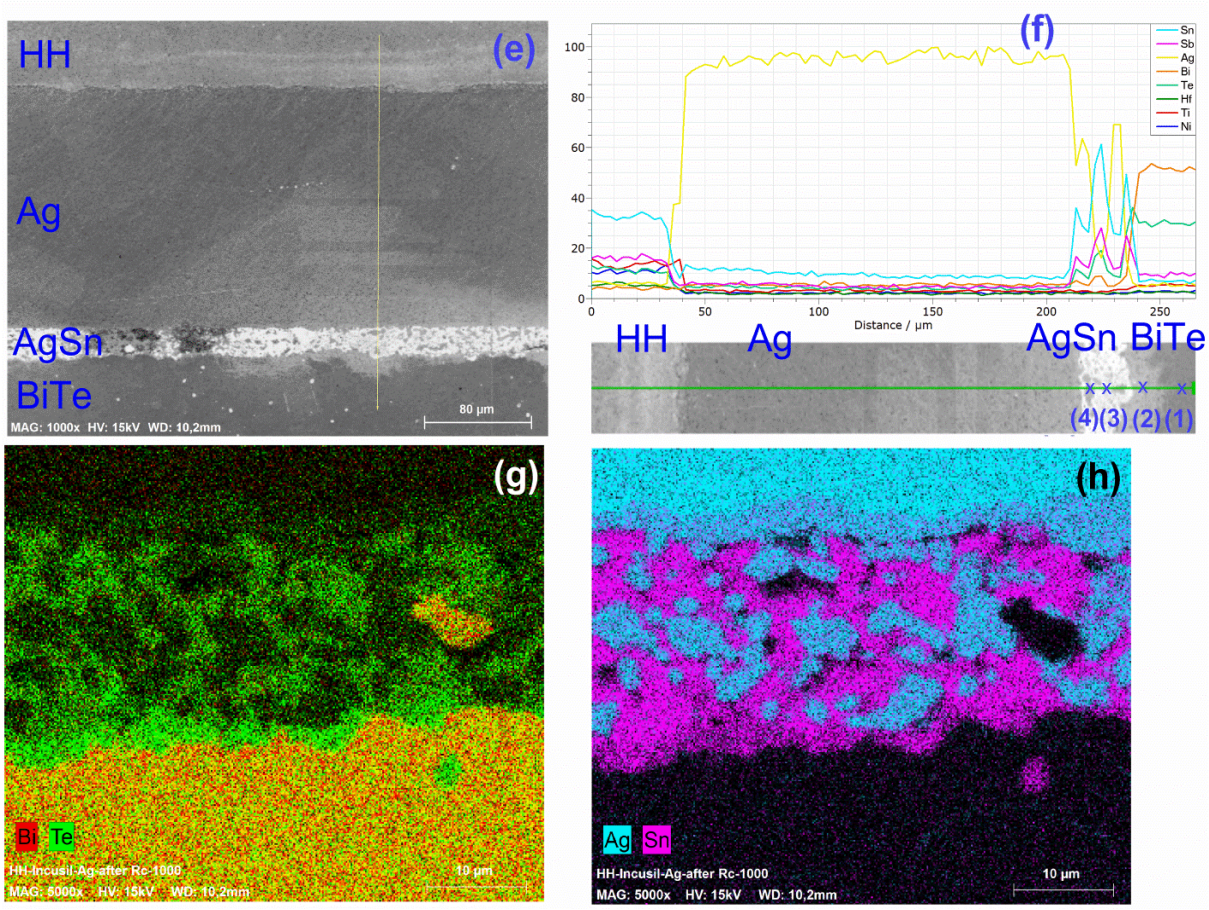

Figure 5- 3 (continue) (e-h). Microstructures and chemical analysis at the joint interface of *n*-type segmented leg before heat treatment: (e) SEM image of the interface, (f) EDS line scan across the interface, (g) Zoom-in image of Bi and Te distributions, and (h) Zoom-in image of Ag and Sn distribution.

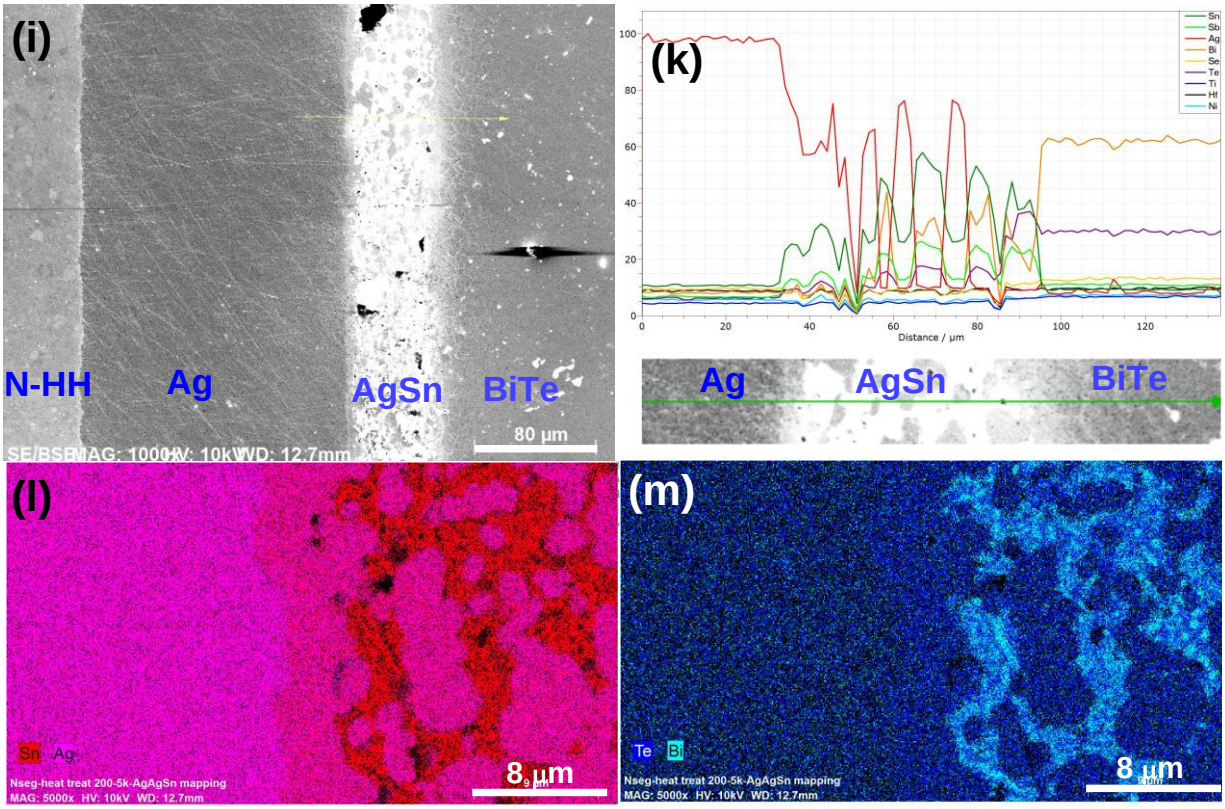

Figure 5- 3 (continue) (i-m). Microstructures and chemical analysis at the joint interface of *n*-type segmented leg after heat treatment: (i) SEM image of the interface, (k) EDS line scan across the interface, (l) Zoom-in image of Ag and Sn distributions, and (m) Zoom-in image of Bi and Te distribution.

The Seebeck coefficient profile of the joined interfaces for *p*- and *n*-segmented leg is shown in Figure 5-4. The ~200 µm thickness of Ag filler corresponded well with the region with low absolute Seebeck coefficients on the scanned area. With the scanning probe resolution of 50 µm (Chapter 2), the intermediate region between BiTe and solder $Ag_{10}Sn$ was observed in the case of *p*-segmented leg. As reflected from the SEM and EDS analysis, this intermediate region is likely to be due to the newly formed diffusion layer composed of (Sn, Sb) and (Sn, Te) - rich phases between BiTe and solder observed from the EDS analysis. It can be interpreted from the Seebeck coefficient mapping results that this intermetallic layer has the thermopower of ~110 μVK^{-1}. Towards the HH part, change in thermopower of the TE material after joining was not observable. In case of *n*-type segmented leg, the Ag and solder layer between BiTe and HH after joining was seen as the region with low Seebeck coefficient < 20 μVK^{-1}. This value corresponds well with the Seebeck coefficients of silver (~ 1.5 μVK^{-1} [222]) tin (-1.5 μVK^{-1} [223]) and SnTe (~ 25 μVK^{-1} [224]), which were main components observed from EDS analysis. The interdiffusion layer between BiTe and HH became more visible after heat treatment (Figure 5-3 f and k). Before heat treatment, the total thickness of the intermediate layer, composed of Ag, $Ag_{10}Sn$ and interdiffusion layers was ~ 100 µm (Figure 5-3 f). Finally, the total thickness expanded to ~ 200 µm (Figure 5-3

k). The Seebeck coefficient of the intermediate layer remained in the range of < 20 μVK^{-1}.

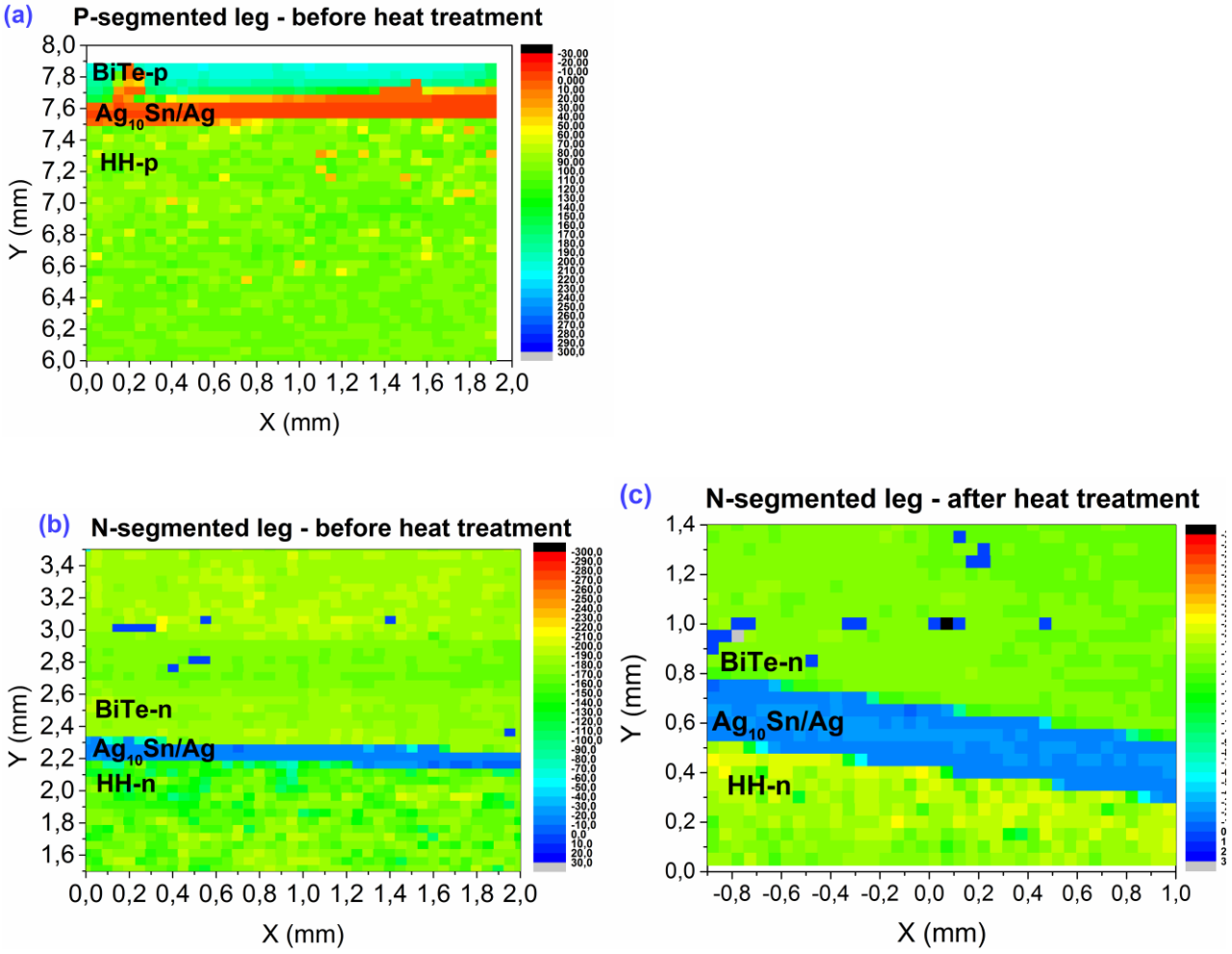

Figure 6-4 Seebeck scanning analysis at the joint interface of *p*- (a) and *n*- (b, c) segmented legs

6.3.2.1 Electrical contact resistances

One of the most important practical features of a joined TE element is its area specific contact resistance. At room temperature, the area specific contact resistances of the *p*- and *n*- obtained segmented elements are 0.5 and 0.4 × 10^{-8} Ωm^2, respectively (Figure 5- 4). This overall specific contact resistance (denoted as R_{ci}) contains resistances of three interfaces: HH/Ag, Ag/$Ag_{10}Sn$ and $Ag_{10}Sn/Bi_2Te_3$. In the whole measured temperature range, the contact resistance of *p*-segmented element was found to be higher than that of *n*-segmented element. As it was detected, there was presence of SnTe in the interfacial layer between BiTe and $Ag_{10}Sn$ solder. SnTe is commonly known as *p*-type semiconductor because of its high Sn- vacancies characteristic, results in high concentrations of hole [200], [224]. Thus, the *p*-type BiTe/SnTe contact is more likely to have higher contact resistance compared to the *n*-type BiTe/SnTe interface. Still, beside SnTe, Ag and Sn also existed in the interfacial layer and their effect to the contact resistance should be explained.

Observation of high contact resistance for *p*-type TE material and metal interface have been studied and reported by O. Yamashita [225], [226]. The study suggests that the formation of Schottky type barrier between *p*-type semiconductor and metal led to the high contact resistance between them. A Schottky contact formed between a metal and a semiconductor in the condition when the work function of metal is smaller than that of *p*-type semiconductor or larger than that of *n*-type semiconductor [227]. The work function of $Ag_{10}Sn$ ~ 4.42 eV, mainly determined by Sn - the dominant component [228]. The work function of Bi_2Te_3 is 5.3 eV [229], by doping with Sb whose work function is 4.55 [228], BiTe becomes *p*-type semiconductor with work function larger than 4.42 eV. Thus, the contact between *p*-type BiTe and solder $Ag_{10}Sn$ in principle is Schottky type. On the contrary, Bi_2Te_3 becomes *n*-type when being doped with Se (work function of Se is 5.9 eV [228]). The resultant work function of *n*-type BiTe should be higher than 4.42 eV. An Ohmic contact between *n*-type BiTe and $Ag_{10}Sn$ is thus expected.

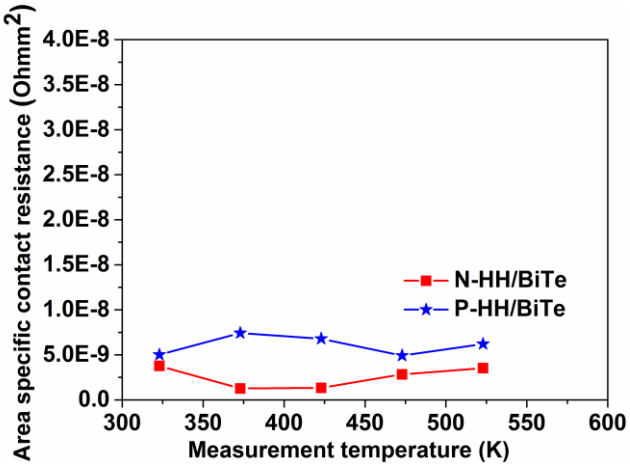

Figure 6-5. Temperature - dependences of area specific contact resistance of the *p*- and *n*- segmented legs

6.3.3 Thermoelectric characteristics of segmented leg

Thermoelectric properties of the as-prepared segmented legs are shown in Figure 5-5. The measured values were also compared with the results from calculation suggested in reference [230]. Detail of the calculation is provided below. The calculation has the assumption that the any interfacial effects are not taken into account. The electrical conductivity of the segmented leg can be calculated by the equation *5-1* below:

$$\frac{\rho_{seg}.l_{total}}{A} = \frac{\rho_{BiTe}.l_{BiTe}+\rho_{HH}.l_{HH}+ ASRc}{A} \qquad (5.1)$$

Where *A*: cross sectional area of segmented leg which is in this case similar both to *n*- and *p*-type legs, *ASRc*: measured area specific contact resistance (Figure 5-1 b); l_{BiTe}, $l_{interlayer}$, and l_{HH} are distances described in Figure 5-1 c, $l_{total} = l_{BiTe} + l_{interlayer} + l_{HH}$. The factors ρ_{BiTe}, ρ_{HH} are the

resistivities of the *p/n*- BiTe and the *p/n* HH and have been measured by using ZEM 3 (Figure 5-2 a, e), ρ_{seg} of both *p*- and *n*- type can then be calculated.

The thermopower of the segmented leg can be calculated from the intrinsic thermopower of the component materials as the following equation [230]:

$$\alpha_{seg} = \frac{\Delta V}{\Delta T} = \frac{\kappa_{HH}\alpha_{BiTe} + \kappa_{BiTe}\alpha_{HH}}{\kappa_{HH} + \kappa_{BiTe}} \qquad (5.2)$$

with κ_{BiTe}, κ_{HH} are the thermal conductivities of the BiTe and the HH (Figure 5-2 c, g) and α_{BiTe}, α_{HH} are Seebeck coefficients of the materials, given in (Figure 5-2 b, f).

The tendencies of the measured and calculated ρ_{seg} of both *p*- and *n*- segmented legs (denoted as $\rho_{p\text{-}seg}$ and $\rho_{n\text{-}seg}$, respectively) are in good agreement with each other (Figure 5- 6 a, c). As it can be seen from Figure 5-6 c, for the *n*-type segmented leg, the $\rho_{n\text{-}seg}$ shown semiconductor behavior with the value of 4×10^{-5} Ωm at 323 K and decreased to 2×10^{-6} Ωm at 473 K. *p*-type segmented leg, on the other hand, shown metallic behavior: $\rho_{p\text{-}seg}$ increased from 0.8 to 1.4×10^{-5} Ωm as temperature increased from 323 to 473 K (see Figure 5-6 a). The measured values were actually smaller than the calculated ones. Notice that the contact resistance measurement was carried out in flowing nitrogen environment, while the resistivity measurement of TE materials and segmented legs have been done in helium gas by using ZEM 3. Thus, it is possible that there is difference of the contact resistance measured by the different equipment. The source of variance is also due to the accurate determination of the thickness of the intermediate layer by using SEM image [231]. All the factors could add up to the discrepancy between measurement and calculation.

The thermopower of *n*-type segmented leg obtained from the measurements are in good agreement with calculations as seen in Figure 5- 6 c. Below 373 K it was slightly smaller than calculated : $\alpha_{n\text{-}seg}$ = 220 μVK^{-1} instead of 240 μVK^{-1} as computed. The uncertainty of the electrical resistivity measurement was 2-5% [30] thus could partly contribute to the difference. Another reason is the contribution of thermal contact resistances that needs further thermal contact resistance measurements to determine. *p*-segmented leg, however, had $\alpha_{p\text{-}seg}$ significantly higher than computed. Computed $\alpha_{p\text{-}seg}$ was estimated to be from 150 to 180 μVK^{-1}, while $\alpha_{p\text{-}seg}$ obtained from experimental was 320 to 230 μVK^{-1} from 323 to 473 K. The reason for the fluctuations between measurement and computation is likely originated from the fact that the thermal contact resistance and the Seebeck coefficient of the intermediate layer (between HH and BiTe) were not included in the calculation. Besides, the Schottky contact between *p*-type semiconductor and metal interlayer was proofed to increase significantly the resultant thermopower of the whole layered structure [226].

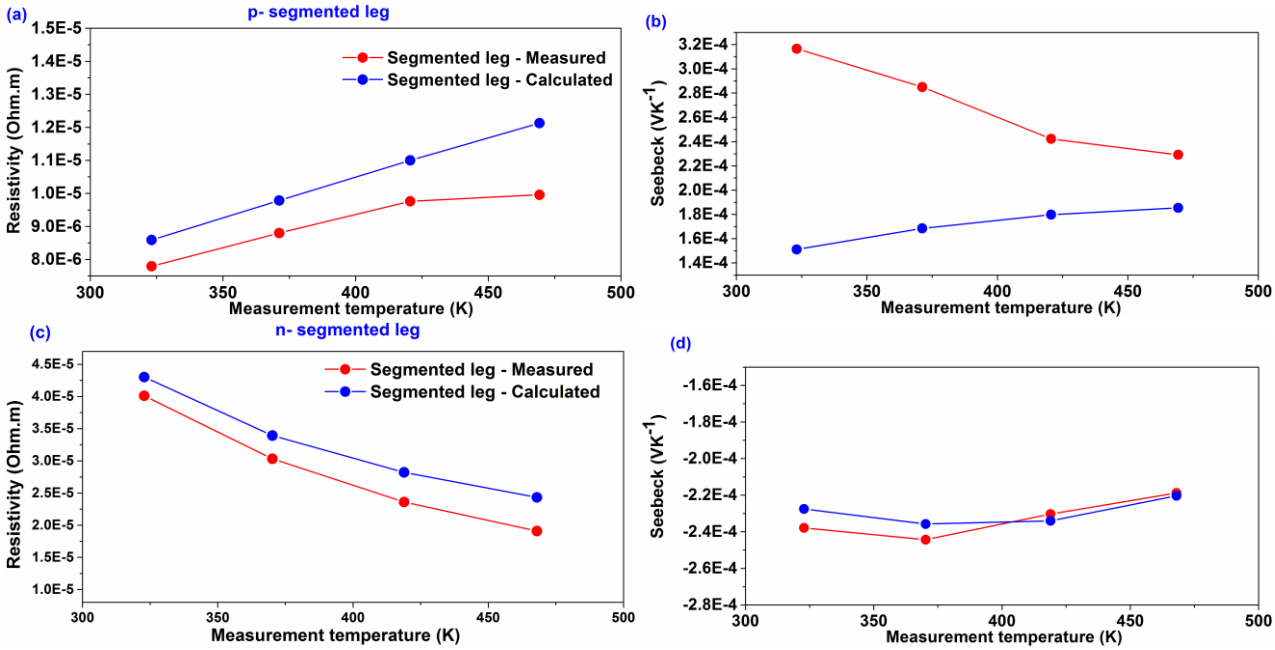

Figure 6-6 Resistivity and Seebeck coefficient *p*- segmented legs (a, b) and *n*- segmented leg (c, d) measured by ZEM 3 according to the configuration illustrated in Figure 5- 1 c.

6.3.4 Output power generating characteristics of segmented legs

The output power characteristics of the obtained segmented legs at different hot side and cold side temperatures are shown in Figure 5.7 a and b. At ΔT = 550 K, the *p*-segmented legs generated a maximum open circuit voltage of 115 mV and maximum current of 1.8 A, giving a power density of 0.3 Wcm^{-2}. The open voltage and maximum current of the *n*-segmented leg were respectively 102 mV and 1.6 A under the hot side/cold side temperatures of 873 and 323 K, corresponding to a power density of 0.25 Wcm^{-2}.

The stability of the segmented legs, evaluated by recording the change of thermoelectric outputs with cycling time, is presented in Figure 5.8. In the case of *p*-segmented leg, after the 6th cycle, the maximum voltage and power density decreased by 4.8 % and 5.5 %, respectively compared with those obtained from the first cycle. As for *n*-segmented leg, the resulted maximum power density reduced by 5.4 % at the end of test, and the highest voltage delivered dropped by 3.9%. The degradation of the output thermoelectric performance can be attributed to several sources. The first reason could be attributed to the expansion of the interlayer between BiTe and $Ag_{10}Sn$, as observed from the microstructural analysis (see Figure 5.3 e, f and l, k). As for the *p*-leg, the solder layer became more porous, thus should influence the generated current (Figure 5.3 a and b). The measured contact resistance at the joining interface showed an increasing trend at temperature of 525 K (Figure 5.5). The second reason may be due to the increase of total TE leg resistance by the

oxidation on the surface of the TE materials in air testing environment and the sublimation of highly volatile elements, especially Sb in HH and BiTe [152], [232]. The reduction of the maximum output voltage might be resulted from the increase in thermal contact resistance between the TE elements and the alumina substrate during cycling. Besides, the effect of uneven deformation of alumina ceramic substrate as a result of high thermal gradient in the thickness direction (which is known as Mayer-Marschall effect) also increases the thermal contact resistance of the tested TE leg [206].

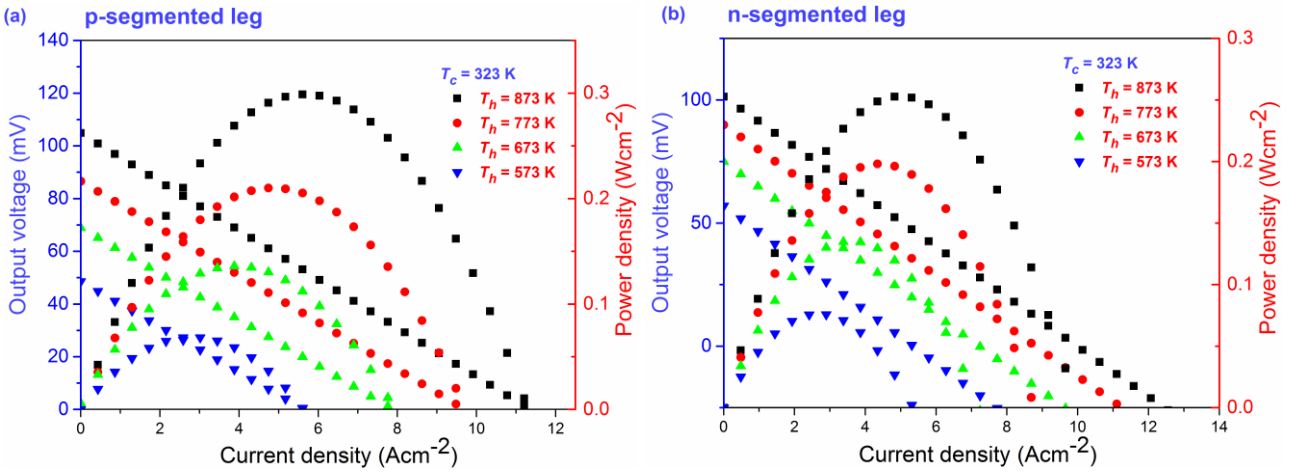

Figure 6-7 Output voltage vs. current density characteristics of obtained segmented *p*- leg (a) and *n*- leg (b).

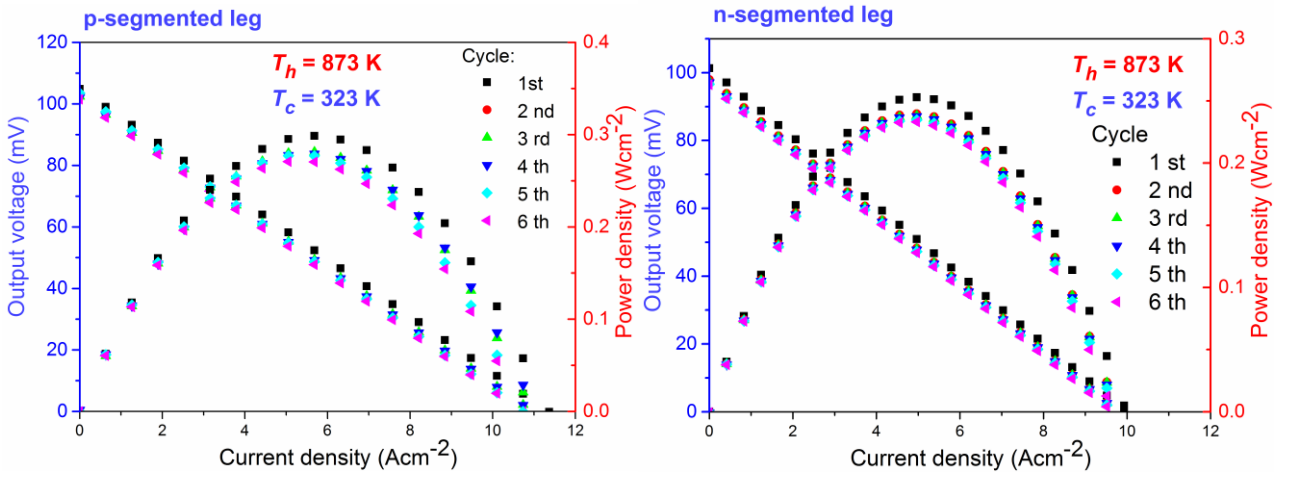

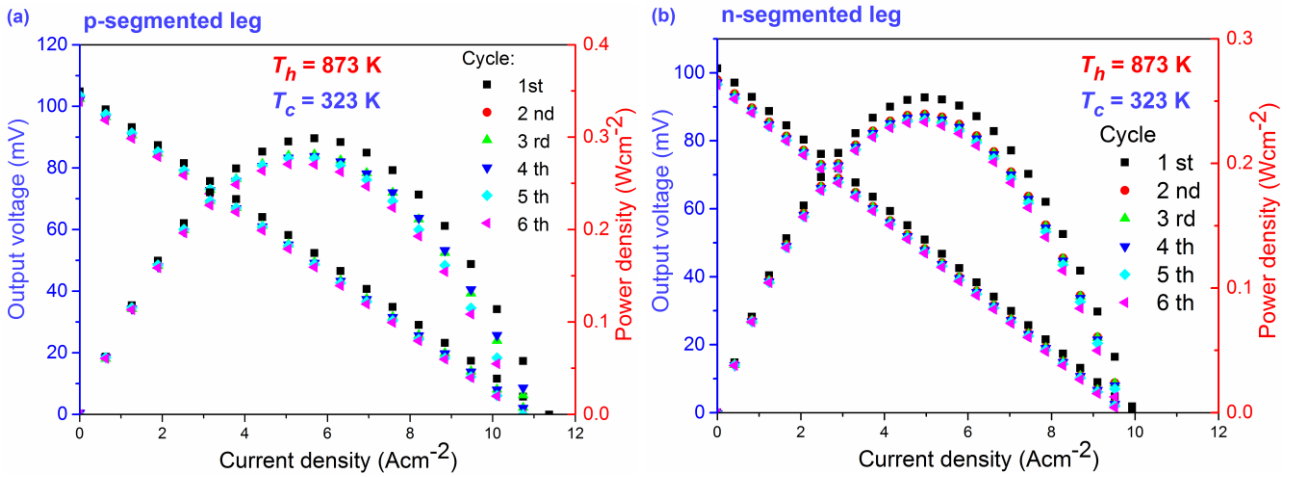

Figure 6-8 Stability test of obtained segmented *p*- segmented leg (a) and *n*- segmented leg (b).

Evaluation

As can be seen from the Figure 5-9, for both *p*- and *n*-segmented legs, there are significant discrepancy between measurement and calculation. The difference in measured and calculated output voltage was 70 % for *p*- leg and 80 % for *n*-leg, indicating non zero thermal loss at interfaces (HH/Ag at the hot end, HH/Ag/$Ag_{10}Sn$/BiTe in the intermediate junction and BiTe/Ag at the cold end). The most noticeable difference was the current, indicating high contact resistance of the tested legs. The overall contact resistance of each leg R_c is the sum of contact at hot side electrode R_{ch}, at the BiTe/HH interface R_{ci} and at the cold side electrode R_{cc}. In the initial setup of the measurement, the cold side electrode was made merely by using silver paste to join BiTe to Ag foil, while the hot side one and the joint between two TE materials were done by fast hot pressing and soldering. Moreover, the R_{ch} and R_{ci} were determined. Calculation of TE output with R_{ch} and R_{ci} show that they degrade the overall output in ideal case by only 5% percent. Thus, the contact resistance at the cold side R_{cc} is strongly suspected to be the main reason for the detrimental reduction of the obtained thermoelectric outputs. By fitting the data from measurement and calculation, the contact resistance at the cold side was computed to be 95 × 10^{-8} and 60 × 10^{-8} Ωm^2 for *p*- and *n*- legs, respectively. The values are substantially high compared with the measured contact resistances at the hot side and at the BiTe/HH interface. Reducing this cold side contact resistance is thus necessary to reveal the full potential of segmenting BiTe with HH.

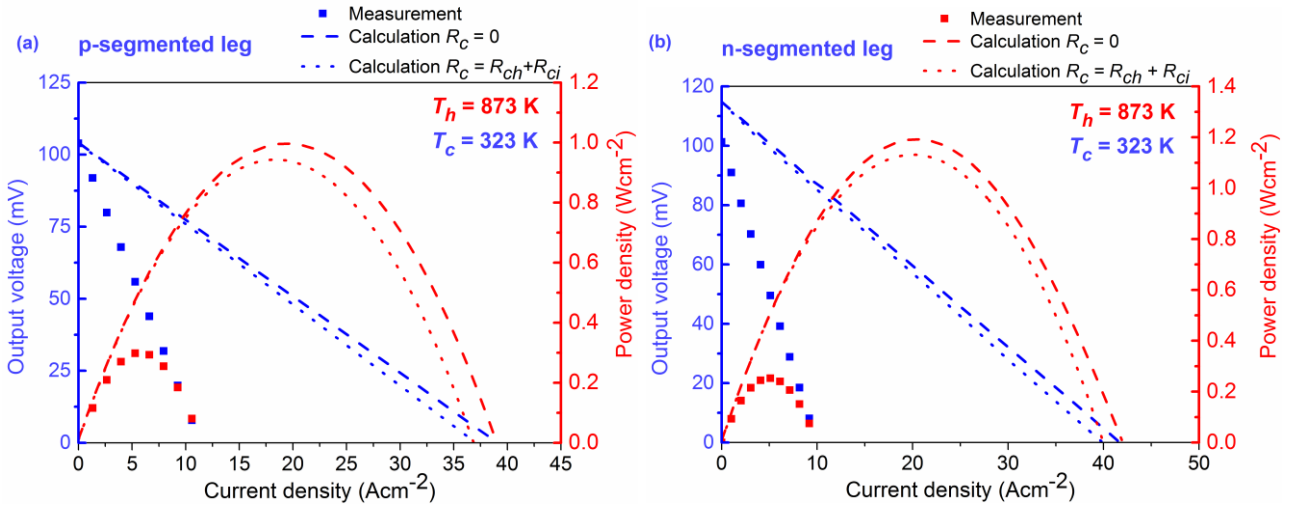

Figure 6-9 Measured and calculated TE performance of the *p*-segmented (a) and *n*-segmented (b) legs. R_{ch}, R_{ci} are contact resistance at hot side and the BiTe/HH interface, respectively.

n-type segmented leg with improved cold side contact

The contact between BiTe and Ag electrode at the cold end after being improved is shown in Figure 5-10. The corresponded contact resistance was measured to be 0.08 × 10^{-8} Ωm^2 at room temperature and increased to 0.17 × 10^{-8} Ωm^2. From the SEM image in Figure 5-10 inset, it could be observed that the connection between layers was good and the inter-diffusion at the interface is minor.

The output performances of the segmented leg with improved cold side electrode is presented and compared with calculation results in Figure 5-10. The obtained open circuit voltage was 98 mV, 6.7% smaller than calculations under ideal condition. The obtained current density and output power reached values of 32.5 Acm^{-2} and 0.8 Wcm^{-2}, respectively. Although these values are still different from the computation data, which is 88 Acm^{-2} for the current density and 2.3 Wcm^{-2} for the power density, the difference between experimental and measurement was reduced by 50 percent compared with the case of the cold side contact. One should notice that the calculated performance of the new *n*-segmented leg is higher than that of the old one due to the modification of the geometry. The new leg has the dimension 10 × 10 × 8 mm^3, while the old one was 4 × 4 × 11 mm^3. A shorter length is known as the reason to increase generated current, thus the thermoelectric power. The resultant measured efficiency was 4.5 %, which was 56% of the expectation in ideal condition.

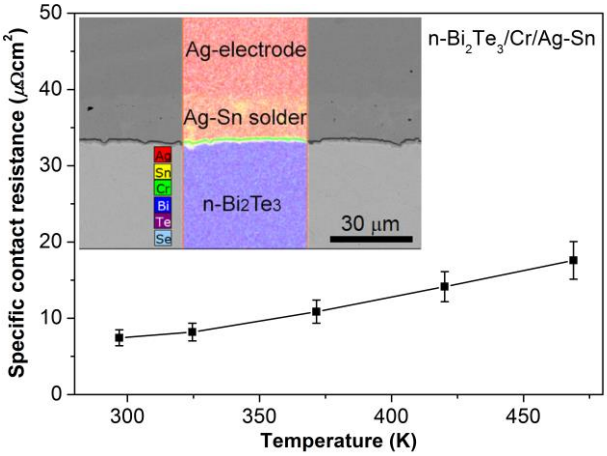

Figure 6-10 Microstructural analysis image (inset figure) and the measured contact resistance of the cold side BiTe/Ag after being improved

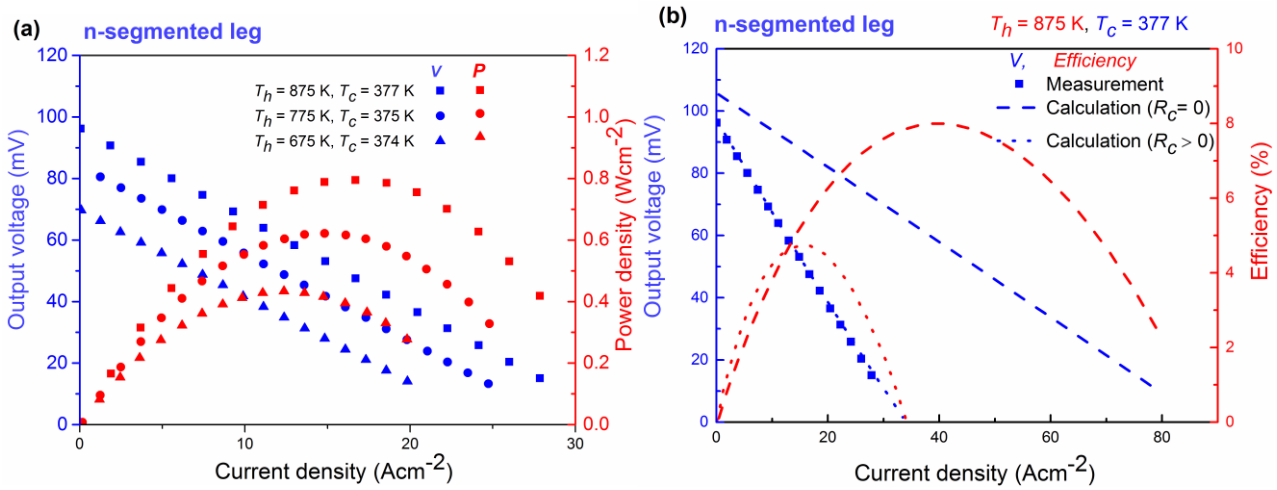

Figure 6-11 (a) Voltage-current characteristic of *n*-segmented leg with improved cold side contact and (b) comparison with calculation.

6.4 Summary

For the first time, the segmentation of *p*- and *n*-type BiTe and HH have been successfully fabricated and characterized using a two-step fast hot pressing process. Microstructural and chemical elements analyses of the joint interfaces showed good contact and no sign of cracks at the joining between the materials. However, the diffusion of tin from the solder alloy into BiTe was observed with a penetration depth of 10 μm. Thermopower microprobe scanning in the vicinity of the joining interface shows no detrimental change of the Seebeck coefficient of the BiTe and HH of the segmented leg after joining, at least within the scale of 50 μm. The contact resistance of the *p*-type BiTe/$Ag_{10}Sn$/Ag/HH structure was measured to be 50×10^{-8} Ωm^2 at room temperature and

increased to 75×10^{-8} Ωm^2 at 523 K. For the *n*-type leg, the contact resistance was found to be 50×10^{-8} Ωm^2 at room temperature and slightly decreased to 35×10^{-8} Ωm^2 at 523 K. The electrical resistivity and thermopower of the developed segmented legs were in good agreement with calculation, although, the Seebeck coefficient of the p-type segmented leg was double as high as the calculated value. The differences are possibly due to the assumption in the calculation's that there are no interfacial effects at the materials' interfaces and the formation of Schottky contact in the case of *p*-type segmented leg.

The thermoelectric outputs of the obtained segmented legs were significantly different from calculation without any contact resistance. Calculation for the segmented legs with contact resistance at hot side R_{ch} and BiTe/HH interface R_{ci} indicate a power output difference of ~ 5 % compared with ideal situation. The main reason for the difference is due to the large contact resistance at the cold side interface between BiTe and electrode. By improving the contact at the cold side, the difference between measurement and calculation in ideal condition was 50 % less. The obtained contact resistance at BiTe/Ag interface was $0.08 – 0.17 \times 10^{-8}$ Ωm^2. Under T_h = 875 K and T_c = 325 K, the improved *n*-segmented leg could deliver a power density of 0.8 Wcm^{-2} and open circuit voltage of 98 mV, with the resultant overall conversion efficiency of 4.5%.

7 Chapter 6 - Conclusion and outlook

In summary, the following main points can be concluded from the thesis:

- One-dimensional numerical model for segmentation was successfully applied considering the most state-of-the-art TE materials to date. With this model, different TE materials were selected and combined in segmentation based on their compatibility factors and TE performance. From this modeling work, various combinations of segmented *p*- and *n*-legs as well as their unicouples with improved conversion efficiency were proposed. It was found that in working temperature range of 300 – 700 K, segmented unicouple composed of *p*-leg $Bi_{0.6}Sb_{1.4}Te_3$+TAGS $((AgSbTe)_{0.15}(GeTe)_{0.85})$ and *n*-leg Bi_2Te_3+PbTe would give the highest efficiency of 13.5%. In medium-high temperature range of 300 – 900 K, a maximum efficiency of 16.6 % is obtainable for the combination of segmented *p*-leg $Bi_{0.6}Sb_{1.4}Te_3$+$Ba_8Au_{5.3}Ge_{40.7}$+PbTe-SrTe with *n*-leg Bi_2Te_3+PbTe+SiGe. For higher temperature up to 1100 K, a combination with the highest efficiency of 18.2% could be possible for the unicouple of segmented $Bi_{0.6}Sb_{1.4}Te_3$+$Ba_8Au_{5.3}Ge_{40.7}$+PbTe-SrTe+SiGe as p-leg and either *segmented* Bi_2Te_3+PbTe+SiGe or Bi_2Te_3+$Ba_{0.08}La_{0.05}Yb_{0.04}Co_4Sb_{12}$ +La_3Te_4 as *n*-leg.
- The critical issue of choosing suitable electrode material and finding a joining technique to obtain good quality contact with thermoelectric *p*- and *n*-type half-Heusler has been addressed. Silver was selected as an electrode for half-Heusler because of its high stability at temperature up to 873 K, which is a feasible hot side temperature for half-Heusler-based TEG. Fast hot pressing method was introduced to join *p*- and *n*-type half-Heusler thermoelectric material with silver electrode. Direct joining of the half-Heusler with silver has found to result in better contact quality than the conventional indirect joining method where a third material (in this work, Incusil^{TM}ABA ®) was used as filler. The comparison between the two methods was based on the measured contact resistances, microprobe thermopower scanning profile, and microstructure analysis of the joining interface. Contact resistances resulted from the direct joining method were significantly lower than that resulted from the indirect one. Direct joining method reduced the contact resistance by at least 50 % compared to that resultant form indirect joining. In the temperature range between 323 – 773 K, contact resistance between *p*- type half-Heusler and silver showed increasing from 0.38 to 0.89×10^{-8} Ωm^2. The contact resistance between *n*-type half-Heusler and silver, meanwhile, decreased from 3.39 to 0.91×10^{-8} Ωm^2. The calculated efficiency of a uncouple built from the prepared half-Heusler *p*- and *n*- type thermoelectric materials was 5%, which is about 85% of the efficiency calculated in the ideal condition. No influence of joining process on the thermopower of half-Heusler materials has been observed, at least within the scale of 50 μm resolution of the Seebeck scanning probe measurement. Microstructures at the half-

Heusler/Ag interface joined directly without filler showed good adherence without delamination and formation of interphases. On the contrary, problems of delamination and interphases appearance between thermoelectric and electrode materials were observed clearly in the joining with filler material.

- For the first time, segmentation of half-Heusler and bismuth tellurides materials has been studied and focused on the challenge in joining issue. Half-Heusler was joined to BiTe by a two-step method: first half-Heusler was joined to silver foil, then, BiTe was joined to the HH/Ag structure by soldering method using $Ag_{10}Sn$ alloy. After joining, microstructure analysis of the obtained *p*- and *n*- segmented legs indicated good contact between the layers, no observable delamination and cracks. In case of segmented *p*-leg, a 10 μm-think interdiffusion layer between BiTe and $Ag_{10}Sn$ was observed, while no interdiffusion was observed in segmented *n*-leg. The joining process had no observable influence on the thermopower of HH and BiTe. The obtained area specific contact resistances were 50 $\mu\Omega cm^2$ and 40 $\mu\Omega cm^2$ for *p*- and *n*- segmeneted legs, respectively. The contact resistances of the *p*-type segmented leg reached 0.75×10^{-8} Ωm^2 at 523 K, while that of *n*-type segmented leg was 0.35×10^{-8} Ωm^2. Heat treatment the segmented samples caused broadening of interdiffusion layer (thickeness upto 100 μm) between $Ag_{10}Sn$ solder alloy and BiTe for *n*-leg, and delamination of *p*-leg. The electrical resistivity, thermopower and the resulted power factor of the whole segmented legs characterized by ZEM 3 shows a good agreement with calculation. With the obtained contact resistance, by applying a numerical calculation model, it is concluded that the maximum efficiency of the segmented leg is minorly decreased by 5 % for both legs. However, thermoelectric output measurement data was detrimentally smaller than calculation. Suspecting the reason was due to the contact at the cold side electrode, which was established using silver paste, *n*-segmented leg with improved cold side contact was fabricated. The improved segmented leg possessed the contact resistance at the cold side of $0.8 – 0.17 \times 10^{-8}$ Ωm^2. Under working temperature of 875 K at the hot side and 325 K at the cold side, the new segmented leg could deliver a maximum power density 0.8 Wcm^{-2} and thermoelectric voltage 95 mV. The calculated data with R_c and losses excluded are 2.3 Wcm^{-2} and 108 mV, respectively. The resulted efficiency was 4.5% from experimental and 8 % from calculated data. Although the variance between reality and calculation was still noticeable, significant improvement was achieved.

Outlook for the future works

- Improving the joining between thermoelectric and electrode materials by depositing a thin metallic layer (for example, silver) on joining surfaces to fill micro-gaps possibly existed and minimize possible reaction or diffusion between thermoelectric and electrode materials. The

metallic layer could be the same material as the electrode. Better contact between surfaces of TE materials and electrode at micrometer scale is possibly decrease contact resistances.

- A diffusion barrier should be fabricated on BiTe surface before joining to prevent the interdiffusion between BiTe and solder alloy. This layer could be nickel or chromium [216], [221], [233], [234].
- Develop 3-segment-legs to increasing the total efficiency due to possibility to expand the working temperature range to 300 – 1100 K. The third segment is high performance material that is stable at elevated temperature such as thermoelectric oxide [75].

8 Appendix

Table 7-1 Element compositions at joining interface of *p*- and *n*- type HH with Ag.

Figure	Point	Element composition (at%)					
		Zr	Hf	Co	Sn	Sb	Ag
Figure 4-3 A	*p*-type HH	16.7	16.7	33	6.67	26.67	-
		Ti	Hf	Ni	Sn		Ag
Figure 5-4 A	*n*-type HH	22.3	13.3	35.2	29.2	-	-
	3	7	26.8	0	5.5	-	60.7
	4	27.4	45.8	4.3	1.96	-	20.6
	5	21	8	0	3.5	-	67.5

Table 8-2 Element compositions at joining interface of *p*- and *n*- type HH with Incusil

Figure	Point	Element composition (at%)								
		Zr	Hf	Co	Sn	Sb	Ag	Cu	In	Ti
Figure 4-3B	10	15.2	14.2	36.7	3.8	27	-	-	3.2	-
	11	17.1	17.1	16.4	14.5	5.3	24.3	14.5	0.1	-
	12		1.94	-	2.5	-	86.6	7	2	
	13	0.12	0.12					0.5	0.1	97.8
	14		1	5.3	1.4	7.9	48.9	21.2	1.9	12.4
Figure	Point	Element composition (at%)								
			Hf	Ni	Sn		Ag	Cu	In	Ti
Figure 5-4 B	22		1.1	-	0.5		93.9	2.4	1.9	0.23
	23		7.8	3.4	-		33.4	53.6	1.7	0.1
	24		0.2	-	-		0	1.7	0	97
	25		0.2	4.6	-		41	44.2	1.1	0.2
	26		9.6	33.4	31.4		1.4	-	3.1	21.1

Table 8-3 Chemical composition of interdiffusion layer between BiTe and solder alloy $Ag_{10}Sn_{90}$

Figure 5- 2	Point	Element composition (at.%)				
		Bi	Te	Sb/Se	Ag	Sn
F	(1) *n*-type BiTe part	37.2	49.5	3.5/2.9	2.2	4.9
	(2) Inter alloy 1	35.5	53.5	3.9/1.8	0.3	5
	(3) Inter alloy 2	2.8	0	5.3/0	14.2	77.7
	(4) Inter alloy 3	0.8	0	2.7/0.2	66	30.4
B	(1) *p*-type BiTe part	6.9	47.6	30.3/0.3	7.6	7.3
	(2) Inter alloy 1	2.1	35.8	15.9/0	3.3	43.1
	(3) Inter alloy 2	0.5	0.4	1.44/0	64.6	33.1
	(4) Inter alloy 3	4	0	12.8/0.6	6.1	76.5

9 References

[1] D. M. Rowe, *CRC handbook of thermoelectrics*. CRC press, 1995.

[2] H. J. Goldsmid, *Introduction to Thermoelectricity*, vol. 3, no. 6. Springer series in Materials Science, 2001.

[3] E. J. Winder, A. B. Ellis, and G. C. Lisensky, "Thermoelectric Devices: Solid-State Refrigerators and Electrical Generators in the Classroom," *J. Chem. Educ.*, vol. 73, no. 10, p. 940, 1996.

[4] H. Alam and S. Ramakrishna, "A review on the enhancement of figure of merit from bulk to nano-thermoelectric materials," *Nano Energy*, vol. 2, no. 2, pp. 190–212, 2013.

[5] D. T. Dat, "Thermoelectric effects-animation," 2013. [Online]. Available: https://www.msu.edu/~dodat/.

[6] E. D. M. Rowe, D. Ph, D. Sc, and F. Group, *Thermoelectrics Handbook: Macro to Nano*. CRC press, Taylor & Francis Group, 2006.

[7] G. J. Snyder and E. S. Toberer, "Complex thermoelectric materials.," *Nat. Mater.*, vol. 7, no. 2, pp. 105–114, 2008.

[8] M. S. Dresselhaus, "Overview of thermoelectrics for thermal to electrical energy conversion," *AIP Conf. Proc.*, vol. 1519, pp. 36–39, 2013.

[9] H. Goldsmid, "Bismuth Telluride and Its Alloys as Materials for Thermoelectric Generation," *Materials (Basel).*, vol. 7, no. 4, pp. 2577–2592, 2014.

[10] C. J. Vineis, A. Shakouri, A. Majumdar, and M. G. Kanatzidis, "Nanostructured thermoelectrics: Big efficiency gains from small features," *Adv. Mater.*, vol. 22, no. 36, pp. 3970–3980, 2010.

[11] J. P. Heremans, V. Jovovic, E. S. Toberer, A. Saramat, Ken Kurosaki, A. Charoenphakdee, S. Yamanaka, and G. J. Snyder, "Enhancement of thermoelectric efficiency in PbTe by distortion of the electronic density of states," *Science (80-.).*, vol. 321, pp. 554–557, 2008.

[12] Y. Pei, X. Shi, A. LaLonde, H. Wang, L. Chen, and G. J. Snyder, "Convergence of electronic bands for high performance bulk thermoelectrics.," *Nature*, vol. 473, no. 7345, pp. 66–69, 2011.

[13] J. Androulakis, C. H. Lin, H. J. Kong, C. Uher, C. I. Wu, T. Hogan, B. a. Cook, T. Caillat, K. M. Paraskevopoulos, and M. G. Kanatzidis, "Spinodal decomposition and nucleation and growth as a means to bulk nanostructured thermoelectrics: Enhanced performance in Pb1-xSnxTe-PbS," *J. Am. Chem. Soc.*, vol. 129, no. 31, pp. 9780–9788, 2007.

[14] S. Q. Bai, Y. Z. Pei, L. D. Chen, W. Q. Zhang, X. Y. Zhao, and J. Yang, "Enhanced thermoelectric performance of dual-element-filled skutterudites BaxCeyCo4Sb12," *Acta Mater.*, vol. 57, no. 11, pp. 3135–3139, 2009.

[15] X. Shi, J. J. Yang, J. R. Salvador, M. Chi, J. Y. Cho, H. Wang, S. Bai, J. J. Yang, W. Zhang, and L. Chen, "Multiple-filled skutterudites: High thermoelectric figure of merit through separately optimizing electrical and thermal transports," *J. Am. Chem. Soc.*, vol. 133, no. 20, pp. 7837–7846, 2011.

[16] X. Yan, G. Joshi, W. Liu, Y. Lan, H. Wang, S. Lee, J. W. Simonson, S. J. Poon, T. M. Tritt, G. Chen, and Z. F. Ren, "Enhanced Thermoelectric Figure of Merit of p-Type Half-Heuslers," *Nano Lett.*, vol. 11, no. 2, pp. 556–560, 2011.

[17] H. Xie, H. Wang, Y. Pei, C. Fu, X. Liu, G. J. Snyder, X. Zhao, and T. Zhu, "Beneficial Contribution of Alloy Disorder to Electron and Phonon Transport in Half-Heusler Thermoelectric Materials," *Adv. Funct. Mater.*, vol. 23, no. 41, pp. 5123–5130, 2013.

[18] E. Rausch, "High thermoelectric figure of merit in p-type Half-Heuslers by intrinsic phase separation," pp. 1–13, 2015.

[19] E. S. Toberer, A. F. May, and G. J. Snyder, "Zintl chemistry for designing high efficiency thermoelectric materials," *Chem. Mater.*, vol. 22, no. 3, pp. 624–634, 2010.

[20] E. S. Toberer, S. R. Brown, T. Ikeda, S. M. Kauzlarich, and G. J. Snyder, "High

thermoelectric efficiency in lanthanum doped Yb14 Mn Sb11," *Appl. Phys. Lett.*, vol. 93, no. 6, pp. 11–14, 2008.

[21] P. Sundarraj, D. Maity, S. S. Roy, and R. a. Taylor, "Recent advances in thermoelectric materials and solar thermoelectric generators – a critical review," *RSC Adv.*, vol. 4, no. 87, pp. 46860–46874, 2014.

[22] W. Liu, Q. Jie, H. S. Kim, and Z. Ren, "Current progress and future challenges in thermoelectric power generation : From materials to devices," *Acta Mater.*, vol. 87, no. 155, pp. 357–376, 2015.

[23] X. F. Zheng, C. X. Liu, Y. Y. Yan, and Q. Wang, "A review of thermoelectrics research - Recent developments and potentials for sustainable and renewable energy applications," *Renew. Sustain. Energy Rev.*, vol. 32, pp. 486–503, 2014.

[24] X. Jia and Y. Gao, "Estimation of thermoelectric and mechanical performances of segmented thermoelectric generators under optimal operating conditions," *Appl. Therm. Eng.*, vol. 73, no. 1, pp. 335–342, 2014.

[25] G. J. Snyder and T. S. Ursell, "Thermoelectric Efficiency and Compatibility," *Phys. Rev. Lett.*, vol. 91, no. 14, 2003.

[26] H. Schock, E. Case, T. Caillat, C. Cauchy, J. D'Angelo, J.-P. Fleurial, T. Hogan, M. Kanatzidis, N. Matchnov, J. Ni, J. Novak, F. Peng, T. Ruckle, J. Sakamoto, R. Schnidt, C. Nelson, T. Shih, E. Timm, and C.-I. Wu, "Thermoelectric conversion of waste heat to electricity in an IC engine powered vehicle: An engine modeling approach," 2009.

[27] A. Vargas-Almeida, M. A. Olivares-Robles, and P. Camacho-Medina, "Thermoelectric system in different thermal and electrical configurations: Its impact in the figure of merit," *Entropy*, vol. 15, no. 6, pp. 2162–2180, 2013.

[28] G. D. Mahan, "Inhomogeneous thermoelectrics," *J. Appl. Phys.*, vol. 70, no. 8, pp. 4551–4554, 1991.

[29] J.-P. F. T. Caillat G. J. Snyder, A. Zoltan, D. Zoltan, and A. Borshchevsky, "A New High Efficiency Segmented Thermoelectric unicouple," in *34th Intersociety Energy Conversion Engineering Conference*, 1999, p. 2567.

[30] L. T. Hung, N. Van Nong, G. J. Snyder, B. Balke, L. Han, R. Bjørk, P. H. Ngan, T. C. Holgate, S. Linderoth, and N. Pryds, "Segmented thermoelectric oxide-based module," *Energy Technol.*, no. September, 2014.

[31] P. H. Ngan, D. V. Christensen, G. J. Snyder, L. T. Hung, S. Linderoth, N. Van Nong, and N. Pryds, "Towards high efficiency segmented thermoelectric unicouples," *Phys. Status Solidi*, vol. 211, no. 1, pp. 9–17, 2014.

[32] T. Caillat, J.-P. Fleurial, G. J. Snyder, and a. Borshchevsky, "Development of high efficiency segmented thermoelectric unicouples," *Proc. ICT2001. 20 Int. Conf. Thermoelectr. (Cat. No.01TH8589)*, pp. 1107–1112, 2001.

[33] W. Seifert, E. Müller, G. J. Snyder, and S. Walczak, "Compatibility factor for the power output of a thermogenerator," *Phys. Status Solidi - Rapid Res. Lett.*, vol. 1, no. 6, pp. 250–252, 2007.

[34] W. Seifert, E. Müller, and S. Walczak, "Generalized analytic one-dimensional description of non-homogeneous TE cooler and generator elements based on the compatibility approach," *Int. Conf. Thermoelectr. ICT, Proc.*, pp. 714–719, 2006.

[35] G. Fraisse, M. Lazard, C. Goupil, and J. Y. Serrat, "Study of a thermoelement's behaviour through a modelling based on electrical analogy," *Int. J. Heat Mass Transf.*, vol. 53, no. 17–18, pp. 3503–3512, 2010.

[36] M. Lazard, "Heat Transfer in Thermoelectricity: Modelling, Optimization and Design," *7th IASME / WSEAS Int. Int. Conf. HEAT Transf. Therm. Eng. Environ.*, pp. 129–134, 2009.

[37] N. A. Matchanov, M. Farhan, E. J. Timm, T. P. Hogan, H. Schock, E. D. Case, and M. G. Kanatzidis, "Investigation of the Hot Side Contacts to Nanostructured LASTt (T) Material. Part I," *Appl. Sol. energy*, vol. 47, no. 2, pp. 90–97, 2011.

[38] J. J. D'Angelo, E. J. Timm, F. Ren, B. D. Hall, E. Case, H. Schock, M. Kanatzidis, D. Y. Chung, T. P. Hogan, J. J. D. Angelo, E. J. Timm, F. Ren, B. D. Hall, E. Case, M. Kanatzidis, D. Y. Chung, T. P. Hogan, J. J. D'Angelo, E. J. Timm, F. Ren, B. D. Hall, E. Case, H. Schock, M. Kanatzidis, D. Y. Chung, and T. P. Hogan, "Electrical Contact Fabrication and Measurements of Metals and Alloys to Thermoelectric Materials," *MRS Proc.*, vol. 1044, pp. 2–8, 2007.

[39] A. A. Shirzadi, H. Assadi, and E. R. Wallach, "Interface evolution and bond strength when diffusion bonding materials with stable oxide films," *Surf. Interface Anal.*, vol. 31, no. 7, pp. 609–618, 2001.

[40] N. Masahashi and S. Hanada, "Effect of Pressure Application by HIP on Microstructure Evolution during Diffusion Bonding," *Mater. Trans.*, vol. 46, no. 7, pp. 1651–1655, 2005.

[41] *Diffusion Bonding of Materials*. Elsevier, 1985.

[42] G. Humpston and D. M. Jacobson, *Principles of Soldering*. ASM International, 2004.

[43] D. M. Jacobson and G. Humpston, *Principles of Brazing*. ASM International, 2005.

[44] J. J. D'Angelo, E. J. Timm, F. Ren, B. D. Hall, E. Case, H. Schock, M. Kanatzidis, D. Y. Chung, T. P. Hogan, J. J. D. Angelo, E. J. Timm, F. Ren, B. D. Hall, E. Case, M. Kanatzidis, D. Y. Chung, and T. P. Hogan, "Electrical Contact Fabrication and Measurements of Metals and Alloys to Thermoelectric Materials," in *MRS Online Proceedings Library*, 2008, vol. 1044, pp. 2–8.

[45] J.-P. Fleurial, T. Caillat, and S. C. Chi, "Electrical contacts for skutterudite thermoelectric materials," Pub. No.: US 2012/0006376 A1, 2012.

[46] A. Singh, S. Bhattascharya, C. Thinaharan, D. K. Aswal, S. K. Gupta, J. V Yakhmi, and K. Bhanumurthy, "Development of low resistance electrical contacts for thermoelectric devices based on n-type PbTe and p-type TAGS-85," *J. Phys. D. Appl. Phys.*, vol. 42, 2009.

[47] C. H. Lim, S. M. Choi, W. S. Seo, M. H. Lee, K. H. Lee, and H. H. Park, "A study of electrodes for thermoelectric oxides," *Electron. Mater. Lett.*, vol. 9, no. 4, pp. 445–449, 2013.

[48] K. T. Wojciechowski, R. Zybala, and R. Mania, "High temperature CoSb3–Cu junctions," *Microelectron. Reliab.*, vol. 51, no. 7, pp. 1198–1202, 2011.

[49] T. C. Holgate, L. Han, N. Wu, E. D. Bøjesen, M. Christensen, B. B. Iversen, N. Van Nong, and N. Pryds, "Characterization of the interface between an Fe–Cr alloy and the p-type thermoelectric oxide Ca3Co4O9," *J. Alloys Compd.*, vol. 582, no. 0, pp. 827–833, 2014.

[50] D. Zhao, H. Geng, and L. Chen, "Microstructure contact studies for skutterudite thermoelectric devices," *Int. J. Appl. Ceram. Technol.*, vol. 9, no. 4, pp. 733–741, 2012.

[51] J. a Fernie, R. a L. Drew, and K. M. Knowles, "Joining of engineering ceramics," *Int. Mater. Rev.*, vol. 54, no. 5, pp. 283–331, 2009.

[52] H. Xia, F. Drymiotis, C.-L. L. Chen, A. Wu, and G. J. Snyder, "Bonding and interfacial reaction between Ni foil and n-type PbTe thermoelectric materials for thermoelectric module applications," *J. Mater. Sci.*, vol. 49, no. 4, pp. 1716–1723, 2014.

[53] M. Mikami, K. Kobayashi, and S. Tanaka, "Power Generation Performance of Thermoelectric Module Consisting of Sb-Doped Heusler Fe₂VAl Sintered Alloy," *Mater. Trans.*, vol. 52, no. 8, pp. 1546–1548, 2011.

[54] A. Muto, J. Yang, B. Poudel, Z. Ren, and G. Chen, "Skutterudite unicouple characterization for energy harvesting applications," *Adv. Energy Mater.*, vol. 3, no. 2, pp. 245–251, 2013.

[55] M. El Genk, H. H. Saber, T. Caillat, and J. Sakamoto, "Test results and performance comparisons of coated and uncoated skutterudite based segmented unicouples," *Energy Convers. Manegement*, vol. 47, pp. 174–200, 2006.

[56] C. R. Koripella, L. E. Bell, D. Crane, B. Llc, and I. Ave, "Portable Power Thermoelectric Generator- Design and Characterization," in *Mater. Res. Soc. Symp. Proc.*, 2010, vol. 1267, pp. 14–17.

[57] M. Masashi, K. Keizo, K. Tetsuya, K. Kazuya, and U. Naoki, “Development and Evaluation of High-Strength Fe 2 VAl Thermoelectric Module,” *Jpn. J. Appl. Phys.*, vol. 47, no. 3R, p. 1512, 2008.

[58] M. Mikami, K. Kobayashi, T. Kawada, K. Kubo, and N. Uchiyama, “Development of a Thermoelectric Module Using the Heusler Alloy Fe2VAl,” *J. Electron. Mater.*, vol. 38, no. 7, pp. 1121–1126, 2009.

[59] S. Populoh, O. C. Brunko, K. Gałłązka, W. Xie, and A. Weidenkaff, “Half-heusler (TiZrHf)NiSn unileg module with high powder density,” *Materials (Basel).*, vol. 6, no. 4, pp. 1326–1332, 2013.

[60] M. Mikami, M. Mizoshiri, K. Ozaki, H. Takazawa, A. Yamamoto, Y. Terazawa, and T. Takeuchi, “Evaluation of the Thermoelectric Module Consisting of W-Doped Heusler Fe 2 VAl Alloy,” *J. Electron. Mater.*, vol. 43, no. 6, pp. 1922–1926, 2014.

[61] D. Zhao, X. Li, Y. Cai, W. Jiang, and L. Chen, “Fabrication and evaluation of CoSb 3 / electrode thermoelectric joints,” *Mater. Sci. Forum*, vol. 631–632, pp. 313–318, 2010.

[62] S.-M. Choi, K.-H. Kim, S.-M. Jeong, H.-S. Choi, Y. Lim, W.-S. Seo, and I.-H. Kim, “A Resistance Ratio Analysis for CoSb3-Based Thermoelectric Unicouples,” *J. Electron. Mater.*, vol. 41, no. 6, pp. 1004–1010, 2012.

[63] J. Q. Guo, H. Y. Geng, T. Ochi, S. Suzuki, M. Kikuchi, Y. Yamaguchi, and S. Ito, “Development of skutterudite thermoelectric materials and modules,” *J. Electron. Mater.*, vol. 41, no. 6, pp. 1036–1042, 2012.

[64] J. García-Cañadas, A. V. Powell, A. Kaltzoglou, P. Vaqueiro, and G. Min, “Fabrication and evaluation of a skutterudite-based thermoelectric module for high-temperature applications,” *J. Electron. Mater.*, vol. 42, no. 7, pp. 1369–1374, 2013.

[65] J. R. Salvador, J. Y. Cho, Z. Ye, J. E. Moczygemba, A. J. Thompson, J. W. Sharp, J. D. König, R. Maloney, T. Thompson, J. Sakamoto, H. Wang, A. a. Wereszczak, and G. P. Meisner, “Thermal to electrical energy conversion of skutterudite-based thermoelectric modules,” *J. Electron. Mater.*, vol. 42, no. 7, pp. 1389–1399, 2013.

[66] T. Ochi, G. Nie, S. Suzuki, M. Kikuchi, S. Ito, and J. Q. Guo, “Power-generation performance and durability of a skutterudite thermoelectric generator,” *J. Electron. Mater.*, vol. 43, no. 6, pp. 2344–2347, 2014.

[67] N. a. Matchanov, M. Farhan, J. D’Angelo, E. J. Timm, T. P. Hogan, H. Schock, E. D. Case, and M. G. Kanatzidis, “Output parameters for thermoelectric modules based on metal/Last(T) hot side contacts. Part II,” *Appl. Sol. Energy*, vol. 48, no. 1, pp. 5–9, 2012.

[68] E. GroB, M. Riffel, and U. Stohrer, “Thermoelectric generators made of FeSi2 and HMS: Fabrication and measurement,” *J. Mater. Res.*, vol. 10, no. 1, pp. 34–40, 1995.

[69] W. S. Cho, K. Park, S. W. Choi, and Y. S. Yoon, “Thermoelectric properties of thermoelectric modules consisted of porous FeSi2 based compounds fabricated by pressureless sintering,” *Mater. Sci. Eng. B Solid-State Mater. Adv. Technol.*, vol. 76, no. 3, pp. 200–205, 2000.

[70] T. Nemoto, I. Iida, J. Sato, T. Sakamoto, T. Nakajima, and Y. Takanashi, “Power generation characteristics of Mg2Si uni-leg thermoelectric generator,” *J. Electron. Mater.*, vol. 41, no. 6, pp. 1312–1316, 2012.

[71] T. Nemoto, T. Iida, J. Sato, T. Sakamoto, N. Hirayama, T. Nakajima, and Y. Takanashi, “Development of an Mg2Si unileg thermoelectric module using durable Sb-doped Mg2Si leg,” *J. Electron. Mater.*, vol. 42, no. 7, pp. 2192–2196, 2013.

[72] I. Matsubara, R. Funahashi, T. Takeuchi, S. Sodeoka, T. Shimizu, and K. Ueno, “Fabrication of an all-oxide thermoelectric power generator,” *Appl. Phys. Lett.*, vol. 78, no. 23, pp. 3627–3629, 2001.

[73] S. Urata, R. Funahashi, and T. Mihara, “Power generation of p-type Ca3Co4O9/n-type CaMnO3 module,” *Int. Conf. Thermoelectr. ICT, Proc.*, pp. 501–504, 2006.

[74] R. Funahashi and S. Urata, “Fabrication and application of an oxide thermoelectric system,” *Int. J. Appl. Ceram. Technol.*, vol. 4, no. 4, pp.

297–307, 2007.

[75] L. T. Hung, N. Van Nong, G. J. Snyder, L. Han, E. Stamate, M. H. Viet, B. Balke, S. Linderoth, and N. Pryds, "High performance p-type segmented leg of misfit-layered cobaltite and half-Heusler alloy," *Energy Convers. Manag.*, vol. 99, pp. 20–27, 2014.

[76] M. S. El-Genk and H. H. Saber, "High efficiency segmented thermoelectric unicouple for operation between 973 and 300 K," *Energy Convers. Manag.*, vol. 44, no. 7, pp. 1069–1088, 2003.

[77] G. Zeng, "Power generator modules of segmented Bi2Te3 and ErAs:(InGaAs)1-x(InAlAs)x," *J. Electron. Mater.*, 2008.

[78] J. D. Angelo, E. D. Case, N. Matchanov, C. Wu, T. P. Hogan, J. Barnard, C. Cauchy, T. Hendricks, and M. G. Kanatzidis, "Electrical , Thermal , and Mechanical Characterization of Novel Segmented-Leg Thermoelectric Modules," vol. 40, no. 10, pp. 2051–2062, 2011.

[79] K. T. Wojciechowski, R. Zybala, J. Leszczynski, P. Nieroda, M. Schmidt, R. Gajerski, and E. Aleksandrova, "Performance characterization of high-efficiency segmented Bi2Te3/CoSb3 unicouples for thermoelectric generators," in *9th European Conference on Thermoelectrics*, 2012, pp. 467–470.

[80] H. S. Kim, K. Kikuchi, T. Itoh, T. Iida, and M. Taya, "Design of segmented thermoelectric generator based on cost-effective and light-weight thermoelectric alloys," *Mater. Sci. Eng. B Solid-State Mater. Adv. Technol.*, vol. 185, no. 1, pp. 45–52, 2014.

[81] J. Yang and T. Caillat, "Thermoelectric Materials for Space and Automotive Power Generation," *MRS Bull.*, vol. 31, no. 03, pp. 224–229, 2006.

[82] M. Hamid Elsheikh, D. A. Shnawah, M. F. M. Sabri, S. B. M. Said, M. Haji Hassan, M. B. Ali Bashir, and M. Mohamad, "A review on thermoelectric renewable energy: Principle parameters that affect their performance," *Renew. Sustain. Energy Rev.*, vol. 30, pp. 337–355, 2014.

[83] T. Caillat, J.-P. Fleurial, and A. Borshchevsky, "Preparation and thermoelectric properties of semiconducting Zn4Sb3," *J. Phys. Chem. Solids*, vol. 58, pp. 1119–1125, 1997.

[84] E. S. Toberer, P. Rauwel, S. Gariel, J. Taftø, and G. Jeffrey Snyder, "Composition and the thermoelectric performance of β-Zn4Sb3," *J. Mater. Chem.*, vol. 20, no. 44, p. 9877, 2010.

[85] L. T. Hung, N. Van Nong, D.-T. Ngo, L. Han, B. B. Iversen, H. Yin, and N. Pryds, "A study of thermoelectric β-Zn4Sb3 under thermal cycling and large temperature gradients," in *Proceeding of International conference on Thermoelectrics*, 2015.

[86] S. Chen and Z. Ren, "Recent progress of half-Heusler for moderate temperature thermoelectric applications," *Mater. Today*, vol. 16, no. 10, pp. 387–395, 2013.

[87] E. A. Skrabek and D. S. Trimmer, "Chapter 22: Properties of the General TAGS System," in *CRC Handbook of Thermoelectrics*, CRC Press LLC, 1995.

[88] J. I. Tani, M. Takahashi, and H. Kido, "Fabrication of oxidation-resistant FeSi2 film on Mg2Si by RF magnetron-sputtering deposition," *J. Alloys Compd.*, vol. 488, no. 1, pp. 346–349, 2009.

[89] S. Battiston, S. Boldrini, S. Fiameni, A. Famengo, M. Fabrizio, and S. Barison, "Multilayered thin films for oxidation protection of Mg2Si thermoelectric material at middle – high temperatures," *Thin Solid Films*, vol. 526, pp. 150–154, 2012.

[90] L. Han, N. Van Nong, L. T. Hung, H. N. Pham, S. H. Spangsdorf, A. Roch, L. Stepien, and N. Pryds, "Optimization of Spark Plasma Sintering conditions for Antimony-doped Bismuth Telluride," in *Proceeding of International conference on thermoelectrics*, 2015.

[91] D. Zhao, X. Li, L. He, W. Jiang, and L. Chen, "High temperature reliability evaluation of CoSb3/electrode thermoelectric joints," *Intermetallics*, vol. 17, no. 3, pp. 136–141, 2009.

[92] E. Godlewska and K. Zawadzka, "Protective coating to suppress degradation of CoSb3 thermoelectric at elevated temperatures,"

Ceram. Mater., vol. 62, no. 4, pp. 490–495, 2010.

[93] J. Leszczynski, K. T. Wojciechowski, and A. L. Malecki, "Studies on thermal decomposition and oxidation of CoSb3," *J. Therm. Anal. Calorim.*, vol. 105, no. 1, pp. 211–222, 2011.

[94] S. K. Bux, J. Fleurial, T. Caillat, B. C. Y. Li, K. Star, S. Firdosy, C. Huang, B. Cheng, P. Gogna, J. Ma, P. Von Allmen, and T. Vo, "Engineering of Novel Thermoelectric Materials and Devices for Next Generation, Long Life, 20% Efficient Space Power Systems," *Proc. 11th Int. Energy Convers. Eng. Conf.*, pp. 1–6, 2013.

[95] S. J. and J.-A. P. Jeff Sakamoto, Thierry Caillat, Jean-Pierre Fleurial, "Improving thermoelectric device performance and durability through the integration of advanced, aerogel-based ceramics," *Electroceramic Mater. Appl.*, pp. 275–290, 2006.

[96] N. Sarhadi, A., Rasmus, B., and Pryds, "Optimization of the mechanical and electrical performance of a thermoelectric module," *J. Electron. Mater.*, p. (In press), 2015.

[97] J. Germond, "Structural Characterization and Thermoelectric Performance of ZrNiSn Half-Heusler Compound Synthesized by Mechanical Alloying," 2010.

[98] Y. Gelbstein, J. Tunbridge, R. Dixon, M. J. Reece, H. Ning, R. Gilchrist, R. Summers, I. Agote, M. a. Lagos, K. Simpson, C. Rouaud, P. Feulner, S. Rivera, R. Torrecillas, M. Husband, J. Crossley, and I. Robinson, "Physical, Mechanical, and Structural Properties of Highly Efficient Nanostructured n- and p-Silicides for Practical Thermoelectric Applications," *J. Electron. Mater.*, vol. 43, no. 6, pp. 1703–1711, 2013.

[99] A. K. Osuga, S. U. Rata, K. K. Urosaki, S. Y. Amanaka, and R. F. Unahashi, "Mechanical Properties of Ca0 . 9Yb0 . 1MnO3 / Ag Composites for n-Type Legs of Thermoelectric Oxide Devices for n-Type Legs of Thermoelectric Oxide Devices," vol. 6399.

[100] F. Ren, B. D. Hall, J. E. Ni, E. D. Case, J. Sootsman, M. G. Kanatzidis, E. Lara-Curzio, R. M. Trejo, and E. J. Timm, "Mechanical Characterization of PbTe-based Thermoelectric Materials," *MRS Proc.*, vol. 1044, 2007.

[101] B. Duan, P. Zhai, S. Ding, C. Xu, G. Li, L. Liu, P. Li, and Q. Zhang, "Effects of nanoparticle size on the thermoelectric and mechanical properties of skutterudite nanocomposites," *J. Electron. Mater.*, vol. 43, no. 6, pp. 2115–2120, 2014.

[102] Y. Gelbstein, G. Gotesman, Y. Lishzinker, Z. Dashevsky, and M. P. Dariel, "Mechanical properties of PbTe-based thermoelectric semiconductors," *Scr. Mater.*, vol. 58, no. 4, pp. 251–254, 2008.

[103] S. Bathula, B. Gahtori, M. Jayasimhadri, S. K. Tripathy, K. Tyagi, a. K. Srivastava, and A. Dhar, "Microstructure and mechanical properties of thermoelectric nanostructured n-type silicon-germanium alloys synthesized employing spark plasma sintering," *Appl. Phys. Lett.*, vol. 105, no. 6, 2014.

[104] R. D. Schmidt, E. D. Case, Z. Lobo, T. R. Thompson, J. S. Sakamoto, X. Y. Zhou, and C. Uher, "Influence of silver nanoparticle addition, porosity, and processing technique on the mechanical properties of Ba0.3Co4Sb 12 skutterudites," *J. Mater. Sci.*, vol. 49, no. 20, pp. 7192–7212, 2014.

[105] Y. Zheng, H. Xie, S. Shu, Y. Yan, H. Li, and X. Tang, "High-Temperature Mechanical and Thermoelectric Properties of p-Type Bi0.5Sb1.5Te3 Commercial Zone Melting Ingots," *J. Electron. Mater.*, vol. 43, no. 6, pp. 1–6, 2013.

[106] Y. Gelbstein, Z. Dashevsky, and M. P. Dariel, "The search for mechanically stable PbTe based thermoelectric materials," *J. Appl. Phys.*, vol. 104, no. 3, 2008.

[107] R. Bjørk, "The universal influence of contact resistance on the efficiency of a thermoelectric generator," *J. Electron. Mater.*, vol. 44, no. 8, pp. 2869–2876, 2015.

[108] M. Science and I. Chemistry, "Junctions and Diffusion Barriers for High Temperature Thermoelectric Modules," pp. 481–485, 2010.

[109] D. Zhao, H. Geng, and L. Chen, "Microstructure Contact Studies for Skutterudite Thermoelectric Devices," *Appl.*

Ceram. Technol., vol. 9, pp. 1–9, 2011.

[110] F. Li, X. Huang, W. Jiang, and L. Chen, "Microstructure and contact resistivity of (Bi, Sb)2Te 3/Sb interface," *AIP Conf. Proc.*, vol. 1449, no. 2012, pp. 458–462, 2012.

[111] L. B. Kong, T. Li, H. H. Hng, F. Boey, T. Zhang, and S. Li, "Chapter 4. Waste Energy Harvesting," in *Lecture notes in Energy*, vol. 24, no. I, 2014.

[112] R. Food and Agriculture Organization of the United Nations, *Energy supply and demand : trends and prospects*. Rome, 2008.

[113] R. Funahashi, C. Wan, F. Dang, H. Anno, R. O. Suzuki, T. Fujisaka, and K. Koumoto, "Development of Thermoelectric Technology from Materials to Generators," in *Advanced materials for clean energy*, Q. Xu and T. Kobayashi, Eds. CRC Press, 2015, pp. 83–142.

[114] "Energy annual outlook." [Online]. Available: http://instituteforenergyresearch.org/wp-content/uploads/2012/12/EIA-annual-outlook-2011-2040.png.

[115] X. Liu, C. Li, Y. D. Deng, and C. Q. Su, "An energy-harvesting system using thermoelectric power generation for automotive application," *Electr. Power Energy Syst.*, vol. 67, pp. 510–516, 2015.

[116] J. Baxter, Z. Bian, G. Chen, D. Danielson, M. S. Dresselhaus, A. G. Fedorov, T. S. Fisher, C. W. Jones, E. Maginn, U. Kortshagen, A. Manthiram, A. Nozik, D. R. Rolison, T. Sands, L. Shi, D. Sholl, and Y. Wu, "Nanoscale design to enable the revolution in renewable energy," *Energy Environ. Sci.*, vol. 2, no. 6, p. 559, 2009.

[117] "Waste Heat Recovery: Technology and Opportunities in U. S. Industry," 2008.

[118] "Energy paths in a combustion engine," *Thermoelectric Systems for Greener Vehicles*, 2004. [Online]. Available: http://www.greencarcongress.com/2004/11/thermoelectric_.html.

[119] S. Leblanc, S. K. Yee, M. L. Scullin, C. Dames, and K. E. Goodson, "Material and manufacturing cost considerations for thermoelectrics," *Renew. Sustain. Energy Rev.*, vol. 32, pp. 313–327, 2014.

[120] J. Yang, "Potential applications of thermoelectric waste heat recovery in the automotive industry," *ICT 2005. 24th Int. Conf. Thermoelectr. 2005.*, pp. 1–5, 2005.

[121] A. Shakouri, "Recent Developments in Semiconductor Thermoelectric Physics and Materials," *Annu. Rev. Mater. Res.*, vol. 41, no. 1, pp. 399–431, 2011.

[122] A. R. Moss, "Arc-melting processes for the refractory metals," *J. less-common Met.*, vol. 1, pp. 60–72, 1959.

[123] "Edmun Buhler Arc melter." [Online]. Available: http://www.edmund-buehler.de/index.php?lan=2&nav=9&sub=21&sel=146. [Accessed: 16-May-2015].

[124] M. Suárez, a Fernández, and J. Menéndez, "Challenges and Opportunities for Spark Plasma Sintering: A Key Technology for a New Generation of Materials," *Sinter. Appl.*, 2013.

[125] "PSM Potential-Seebeck Microprobe." [Online]. Available: http://www.panco.de/downloads/flyerSMPpanco0707.pdf.

[126] L. T. Hung, "Segmented thermoelectric oxide-based module," Technical University of Denmark, 2014.

[127] H. L. Ni, X. B. Zhao, T. J. Zhu, X. H. Ji, and J. P. Tu, "Synthesis and thermoelectric properties of Bi2Te3 based nanocomposites," *J. Alloys Compd.*, vol. 397, no. 1–2, pp. 317–321, 2005.

[128] Y. Ma, Q. Hao, B. Poudel, Y. Lan, B. Yu, D. Wang, G. Chen, and Z. Ren, "Enhanced thermoelectric figure-of-merit in p-type nanostructured bismuth antimony tellurium alloys made from elemental chunks," *Nano Lett.*, vol. 8, no. 8, pp. 2580–2584, 2008.

[129] G. Rogl, A. Grytsiv, P. Rogl, E. Bauer, M. B. Kerber, M. Zehetbauer, and S. Puchegger, "Multifilled nanocrystalline p-type didymium – Skutterudites with ZT>1.2," *Intermetallics*, vol. 18, no. 12, pp. 2435–2444, Dec. 2010.

[130] A. Zevalkink, W. G. Zeier, G. Pomrehn, E. Schechtel, W. Tremel, and G. J. Snyder,

"Thermoelectric properties of Sr3GaSb3 – a chain-forming Zintl compound," *Energy Environ. Sci.*, vol. 5, no. 10, p. 9121, Oct. 2012.

[131] E. S. Toberer, C. A. Cox, S. R. Brown, T. Ikeda, A. F. May, S. M. Kauzlarich, and G. J. Snyder, "Traversing the Metal-Insulator Transition in a Zintl Phase: Rational Enhancement of Thermoelectric Efficiency in Yb 14 Mn 1− x Al x Sb 11," *Adv. Funct. Mater.*, vol. 18, no. 18, pp. 2795–2800, Sep. 2008.

[132] M. Authors, "Nuclear & Emerging Technologies for Space Albuquerque , New Mexico Sponsored by The American Nuclear Society The American Institute of Aeronautics and Astronautics," in *Nuclear & Emerging Technologies for Space 2011*, 2011.

[133] A. Zevalkink, E. S. Toberer, W. G. Zeier, E. Flage-Larsen, and G. J. Snyder, "Ca3AlSb3: an inexpensive, non-toxic thermoelectric material for waste heat recovery," *Energy Environ. Sci.*, vol. 4, no. 2, p. 510, 2011.

[134] E. S. Toberer, A. Zevalkink, N. Crisosto, and G. J. Snyder, "The Zintl compound Ca5Al2Sb6 for low-cost thermoelectric power generation," *Adv. Funct. Mater.*, vol. 20, no. 24, pp. 4375–4380, 2010.

[135] H. Zhang, L. Fang, M.-B. Tang, Z. Y. Man, H. H. Chen, X. X. Yang, M. Baitinger, Y. Grin, and J.-T. Zhao, "Thermoelectric properties of Yb(x)Eu(1-x)Cd2Sb2.," *J. Chem. Phys.*, vol. 133, no. 19, p. 194701, 2010.

[136] Y. Pei, A. D. Lalonde, N. a. Heinz, X. Shi, S. Iwanaga, H. Wang, L. Chen, and G. J. Snyder, "Stabilizing the optimal carrier concentration for high thermoelectric efficiency," *Adv. Mater.*, vol. 23, no. 47, pp. 5674–5678, 2011.

[137] K. Biswas, J. He, I. D. Blum, C.-I. Wu, T. P. Hogan, D. N. Seidman, V. P. Dravid, and M. G. Kanatzidis, "High-performance bulk thermoelectrics with all-scale hierarchical architectures.," *Nature*, vol. 489, no. 7416, pp. 414–8, Sep. 2012.

[138] A. D. LaLonde, Y. Pei, and G. J. Snyder, "Reevaluation of PbTe1−xIx as high performance n-type thermoelectric material," *Energy Environ. Sci.*, vol. 4, no. 6, p. 2090, 2011.

[139] G. Joshi, H. Lee, Y. Lan, X. Wang, G. Zhu, D. Wang, R. W. Gould, D. C. Cuff, M. Y. Tang, M. S. Dresselhaus, G. Chen, and Z. Ren, "Enhanced thermoelectric figure-of-merit in nanostructured p-type silicon germanium bulk alloys.," *Nano Lett.*, vol. 8, no. 12, pp. 4670–4, Dec. 2008.

[140] X. W. Wang, H. Lee, Y. C. Lan, G. H. Zhu, G. Joshi, D. Z. Wang, J. Yang, a. J. Muto, M. Y. Tang, J. Klatsky, S. Song, M. S. Dresselhaus, G. Chen, and Z. F. Ren, "Enhanced thermoelectric figure of merit in nanostructured n-type silicon germanium bulk alloy," *Appl. Phys. Lett.*, vol. 93, no. 19, p. 193121, 2008.

[141] M. Chitroub, F. Besse, and H. Scherrer, "Thermoelectric properties of semi-conducting compound Zn4Sb3," *J. Alloys Compd.*, vol. 460, no. 1–2, pp. 90–93, 2008.

[142] H. Liu, X. Shi, F. Xu, L. Zhang, W. Zhang, L. Chen, Q. Li, C. Uher, T. Day, and G. J. Snyder, "Copper ion liquid-like thermoelectrics," *Nat. Mater.*, vol. 11, no. 5, pp. 422–425, 2012.

[143] M. L. Liu, I. W. Chen, F. Q. Huang, and L. D. Chen, "Improved thermoelectric properties of cu-doped quaternary chalcogenides of Cu2CdSnSe4," *Adv. Mater.*, vol. 21, no. 37, pp. 3808–3812, 2009.

[144] M. L. Liu, F. Q. Huang, L. D. Chen, and I. W. Chen, "A wide-band-gap p -type thermoelectric material based on quaternary chalcogenides of Cu2ZnSnQ4 (Q=S,Se)," *Appl. Phys. Lett.*, vol. 94, no. 20, 2009.

[145] X. Y. Shi, F. Q. Huang, M. L. Liu, and L. D. Chen, "Thermoelectric properties of tetrahedrally bonded wide-gap stannite compounds Cu2 ZnSn1-x Inx Se4," *Appl. Phys. Lett.*, vol. 94, no. 12, pp. 2–5, 2009.

[146] M. Ibáñez, R. Zamani, A. Lalonde, D. Cadavid, W. Li, and A. Shavel, "Cu 2 ZnGeSe 4 Nanocrystals : Synthesis and Thermoelectric Properties Supporting Information," *Rev. Lit. Arts Am.*, no. I, pp. 1–6, 2012.

[147] K. F. Hsu, S. Loo, F. Guo, W. Chen, J. S. Dyck, C. Uher, T. Hogan, E. K. Polychroniadis, and M. G. Kanatzidis, "Cubic AgPb(m)SbTe(2+m): bulk thermoelectric

materials with high figure of merit.," *Science*, vol. 303, no. 5659, pp. 818–821, 2004.

[148] A. F. May, J. P. Fleurial, and G. J. Snyder, "Optimizing thermoelectric efficiency in La3-xTe4 via Yb substitution," *Chem. Mater.*, vol. 22, no. 9, pp. 2995–2999, 2010.

[149] T. Plirdpring, K. Kurosaki, A. Kosuga, T. Day, S. Firdosy, V. Ravi, G. J. Snyder, A. Harnwunggmoung, T. Sugahara, Y. Ohishi, H. Muta, and S. Yamanaka, "Chalcopyrite CuGaTe 2: A high-efficiency bulk thermoelectric material," *Adv. Mater.*, vol. 24, no. 27, pp. 3622–3626, 2012.

[150] R. Funahashi, M. Mikami, T. Mihara, S. Urata, and N. Ando, "A portable thermoelectric-power-generating module composed of oxide devices," *J. Appl. Phys.*, vol. 99, no. 6, pp. 1–4, 2006.

[151] M. S. El-Genk, H. H. Saber, and T. Caillat, "A performance comparison of SiGe and skutterudite based segmented thermoelectric devices.," *Aip Conf. Proc.*, vol. 608, no. 1, p. 1007, 2002.

[152] H. H. Saber and M. S. El-Genk, "A three-dimensional, performance model of segmented thermoelectric converters," *AIP Conf. Proc.*, vol. 608, no. 1, p. 998, 2002.

[153] W. Seifert, V. Pluschke, C. Goupil, K. Zabrocki, and G. J. Snyder, "Maximum performance in self-compatible thermoelectric elements," *j. mater. res.*, vol. 26, no. 15, pp. 1933–1939, 2011.

[154] G. J. Snyder, "Application of the compatibility factor to the design of segmented and cascaded thermoelectric generators," *Appl. Phys. Lett.*, vol. 84, no. 13, pp. 2436–2438, 2004.

[155] T. Ikeda, S. Iwanaga, H. Wu, N. J. Marolf, S. Chen, and G. J. Snyder, "A combinatorial approach to microstructure and thermopower of bulk thermoelectric materials: the pseudo-ternary PbTe–Ag2Te–Sb2Te3 system," *J. Mater. Chem.*, pp. 24335–24347, 2012.

[156] N. Chen, F. Gascoin, G. J. Snyder, E. Müller, G. Karpinski, and C. Stiewe, "Macroscopic thermoelectric inhomogeneities in (AgSbTe 2) x (PbTe) 1-x," *Appl. Phys. Lett.*, vol. 87, no. 17, pp. 1–3, 2005.

[157] M. Ohtaki, K. Araki, and K. Yamamoto, "High thermoelectric performance of dually doped ZnO ceramics," *J. Electron. Mater.*, vol. 38, no. 7, pp. 1234–1238, 2009.

[158] N. Van Nong, N. Pryds, S. Linderoth, and M. Ohtaki, "Enhancement of the thermoelectric performance of p-type layered oxide Ca3Co4O9+δ through heavy doping and metallic nanoinclusions," *Adv. Mater.*, vol. 23, no. 21, pp. 2484–2490, 2011.

[159] N. Shutoh and S. Sakurada, "Thermoelectric Properties of the Tix(Zro.5Hf0.5)1-xNiSn Half-Heusler Compounds," *2003 Ieee*, p. 312, 2003.

[160] H. Zhang, H. Borrmann, N. Oeschler, C. Candolfi, W. Schnelle, M. Schmidt, U. Burkhardt, M. Baitinger, J. T. Zhao, and Y. Grin, "Atomic interactions in the p-type clathrate i Ba8Au 5.3Ge40.7," *Inorg. Chem.*, vol. 50, no. 4, pp. 1250–1257, 2011.

[161] F. Gascoin, J. Rasmussen, and G. J. Snyder, "High temperature thermoelectric properties of Mo3Sb7-xTex for x = 1.6 and 1.5," *J. Alloys Compd.*, vol. 427, no. 1–2, pp. 324–329, 2007.

[162] X. J. Wang, M. B. Tang, H. H. Chen, X. X. Yang, J. T. Zhao, U. Burkhardt, and Y. Grin, "Synthesis and high thermoelectric efficiency of Zintl phase Yb Cd 2-xZnxSb2," *Appl. Phys. Lett.*, vol. 94, no. 9, 2009.

[163] Q. Zhang, J. He, T. J. Zhu, S. N. Zhang, X. B. Zhao, and T. M. Tritt, "High figures of merit and natural nanostructures in Mg2Si 0.4Sn0.6 based thermoelectric materials," *Appl. Phys. Lett.*, vol. 93, no. 10, pp. 4–7, 2008.

[164] X. Shi, J. Yang, S. Bai, J. Yang, H. Wang, M. Chi, J. R. Salvador, W. Zhang, L. Chen, and W. Wong-Ng, "On the design of high-efficiency thermoelectric clathrates through a systematic cross-substitution of framework elements," *Adv. Funct. Mater.*, vol. 20, no. 5, pp. 755–763, 2010.

[165] W. Liu, X. Yan, G. Chen, and Z. Ren, "Recent advances in thermoelectric nanocomposites," *Nano Energy*, vol. 1, no. 1, pp. 42–56, 2012.

[166] Y. Gelbstein, N. Tal, A. Yarmek, Y.

Rosenberg, M. P. Dariel, S. Ouardi, B. Balke, C. Felser, and M. Köhne, "Thermoelectric properties of spark plasma sintered composites based on TiNiSn half-Heusler alloys," *J. Mater. Res.*, vol. 26, no. 15, pp. 1919–1924, Jun. 2011.

[167] L. T. Hung, N. Van Nong, S. Linderoth, and N. Pryds, "Segmentation of low-cost high efficiency oxide-based thermoelectric materials," *Phys. Status Solidi*, vol. 8, p. n/a–n/a, 2015.

[168] T. H. Le, L. Han, E. Stamate, H. N. Pham, B. Balke, S. Linderoth, N. Van Nong, and N. Pryds, "Preparation and characterization of segmented p-type Ti0.3Zr0.35Hf0.35CoSb0.8Sn0.2/Ca3Co4O9," *Energy (submitted)*, 2014.

[169] K. Bartholomé, B. Balke, D. Zuckermann, M. Köhne, M. Müller, K. Tarantik, and J. König, "Thermoelectric Modules Based on Half-Heusler Materials Produced in Large Quantities," *J. Electron. Mater.*, vol. 43, no. 6, pp. 1775–1781, 2014.

[170] G. Joshi, X. Yan, H. Wang, W. Liu, G. Chen, and Z. Ren, "Enhancement in Thermoelectric Figure-Of-Merit of an N-Type Half-Heusler Compound by the Nanocomposite Approach," *Adv. Energy Mater.*, vol. 1, pp. 643–647, 2011.

[171] X. Yan, G. Joshi, W. Liu, Y. Lan, H. Wang, S. Lee, J. W. Simonson, S. J. Poon, T. M. Tritt, G. Chen, and Z. F. Ren, "Enhanced Thermoelectric Figure of Merit of p-Type Half-Heuslers," *Nano Lett.*, vol. 11, no. 2, pp. 556–560, 2010.

[172] M. Schwall and B. Balke, "Phase separation as a key to a thermoelectric high efficiency," *Phys. Chem. Chem. Phys.*, vol. 15, no. 6, pp. 1868–1872, 2013.

[173] X. Yan, W. Liu, H. Wang, S. Chen, J. Shiomi, K. Esfarjani, H. Wang, D. Wang, G. Chen, and Z. Ren, "Stronger phonon scattering by larger differences in atomic mass and size in p-type half-Heuslers Hf1-xTixCoSb0.8Sn0.2," *Energy Environ. Sci.*, vol. 5, no. 6, pp. 7543–7548, 2012.

[174] P. Qiu, X. Huang, X. Chen, and L. Chen, "Enhanced thermoelectric performance by the combination of alloying and doping in TiCoSb-based half-Heusler compounds," *J. Appl. Phys.*, vol. 106, no. 10, p. 103703, 2009.

[175] S. Sakurada and N. Shutoh, "Effect of Ti substitution on the thermoelectric properties of (Zr,Hf)NiSn half-Heusler compounds," *Appl. Phys. Lett.*, vol. 86, p. 82105, 2005.

[176] S. Populoh, O. Brunko, K. Gałązka, W. Xie, and A. Weidenkaff, "Half-Heusler (TiZrHf)NiSn Unileg Module with High Powder Density," *Materials (Basel).*, vol. 6, no. 4, pp. 1326–1332, 2013.

[177] M. Mikami, K. Kobayashi, and S. Tanaka, "Power Generation Performance of Thermoelectric Module Consisting of Sb-Doped Heusler Fe2VAl Sintered Alloy," *Mater. Trans.*, vol. 52, no. 8, pp. 1546–1548, 2011.

[178] S. J. Poon, D. Wu, S. Zhu, W. Xie, T. M. Tritt, P. Thomas, and R. Venkatasubramanian, "Half-Heusler phases and nanocomposites as emerging high-ZT thermoelectric materials," *J. Mater. Res.*, vol. 26, pp. 2795–2802, 2011.

[179] J. García-Cañadas and G. Min, "Preparation and characterisation of contacts for high temperature thermoelectric modules," *AIP Conf. Proc.*, vol. 1449, no. 1, pp. 454–457, 2012.

[180] Y. Zhu, K. Mimura, J. W. Lim, M. Isshiki, and Q. Jiang, "Brief review of oxidation kinetics of copper at 350 °C to 1050 °C," *Metall. Mater. Trans. A Phys. Metall. Mater. Sci.*, vol. 37, no. 4, pp. 1231–1237, 2006.

[181] Y. Zhu, K. Mimura, and M. Isshiki, "Oxidation Mechanism of Copper at 623-1073 K," *Mater. Trans.*, vol. 43, no. 9, pp. 2173–2176, 2002.

[182] C. N. Liao, C. H. Lee, and W. J. Chen, "Effect of interfacial compound formation on contact resistivity of soldered junctions between bismuth telluride-based thermoelements and copper," *Electrochem. solid-state Lett.*, vol. 10, no. 9, pp. 23–25, 2007.

[183] R. Gupta, R. McCarty, and J. Sharp, "Practical Contact Resistance Measurement Method for Bulk Bi2Te3-Based Thermoelectric Devices," *J. Electron. Mater.*, vol. 43, no. 6, pp. 1608–1612, 2014.

[184] F.-D. Börner, M. Schreier, B. Feng, W. Lippmann, H.-P. Martin, A. Michaelis, and A. Hurtado, "Development of laser-based joining technology for the fabrication of ceramic thermoelectric modules," *J. Mater. Res.*, vol. 29, no. 16, pp. 1771–1780, 2014.

[185] D. Zhao, C. Tian, S. Tang, Y. Liu, L. Jiang, and L. Chen, "Fabrication of a CoSb3-based thermoelectric module," *Mater. Sci. Semicond. Process.*, vol. 13, no. 3, pp. 221–224, 2010.

[186] H. Xia, F. Drymiotis, C.-L. Chen, A. Wu, and G. J. Snyder, "Bonding and interfacial reaction between Ni foil and n-type PbTe thermoelectric materials for thermoelectric module applications," *J. Mater. Sci.*, vol. 49, no. 4, pp. 1716–1723, 2014.

[187] Y. Thimont, Q. Lognoné, C. Goupil, F. Gascoin, and E. Guilmeau, "Design of Apparatus for Ni/Mg2Si and Ni/MnSi1.75 Contact Resistance Determination for Thermoelectric Legs," *J. Electron. Mater.*, vol. 43, no. 6, pp. 2023–2028, 2014.

[188] F. C. Nix and D. MacNair, "The Thermal Expansion of Pure Metals. II: Molybdenum, Palladium, Silver, Tantalum, Tungsten, Platinum, and Lead," *Phys. Rev.*, vol. 61, no. 1–2, pp. 74–78, 1942.

[189] M. advanced materials, "Datasheet Wesgo metals Incusil ABA." 2009.

[190] I. Karakaya and W. T. Thompson, "The Ag-Zr (silver-zirconium) system," *J. phase equilibria*, vol. 13, no. 2, pp. 143–146, 1992.

[191] O. Madelung, Ed., *Ag – Hf (Silver – Hafnium) Ag-Hf*. Landolt-Börnstein, 1991.

[192] Z. Bahari, M. Elgadi, J. Rivet, and J. Dugué, "Experimental study of the ternary Ag–Cu–In phase diagram," *J. Alloys Compd.*, vol. 477, no. 1–2, pp. 152–165, 2009.

[193] X. Fu, C. Li, F. Wang, M. Li, and W. Zhang, "Experimental study on the phase equilibria of the Ag–Ti system," *Mater. Sci. Eng. A*, vol. 408, no. 1–2, pp. 190–194, 2005.

[194] H. Okamoto, "Cu-Ti (copper-titanium)," *J. phase equilibria*, vol. 23, no. 6, pp. 549–550, 2002.

[195] P. J. R. Subramanian and L. DE, "The Cu-ln (Copper-Indium) System," *Bull. Alloy Phase Diagrams Vol*, vol. 10, no. 5, p. 655, 1989.

[196] Y. Y. Wu, W. P. Lin, and C. C. Lee, "A study of chemical reactions of silver and indium at 180 °c," *J. Mater. Sci. Mater. Electron.*, vol. 23, no. 12, pp. 2235–2244, 2012.

[197] H. Okamoto, "Hf-Ti (hafnium-titanium)," *J. phase equilibria*, vol. 18, no. 6, p. 672, 1997.

[198] I. Karakaya and W. T. Thompson, "The Ag-Sn (Silver-Tin) system," *Bull. Alloy Phase Diagrams*, vol. 8, no. 4, pp. 340–347, 1987.

[199] W. Z. Zhu and S. C. Deevi, "Opportunity of metallic interconnects for solid oxide fuel cells: A status on contact resistance," *Mater. Res. Bull.*, vol. 38, no. 6, pp. 957–972, 2003.

[200] C. N. Liao, C. H. Lee, and W. J. Chen, "Effect of interfacial compound formation on contact resistivity of soldered junctions between bismuth telluride-based thermoelements and copper," *Electrochem. Solid-State Lett.*, vol. 10, no. 9, pp. 23–25, 2007.

[201] N. Bae, S. Han, K. Eun, B. Kim, and S. Kim, "Diffusion at interfaces of micro thermoelectric devices," *Curr. Appl. Phys.*, vol. 11, pp. S40–S44, 2011.

[202] S. S. Alloy, "Tehcnical sheet Ag10Sn." Spring welding alloys.

[203] T. H. Le, L. Han, E. Stamate, H. N. Pham, B. Balke, S. Linderoth, N. Van Nong, N. Pryds, T. H. Le, L. Han, E. Stamate, H. N. Pham, B. Balke, S. Linderoth, N. Van Nong, and N. Pryds, "Preparation and characterization of segmented p-type $Ti_{0.3}Zr_{0.35}Hf_{0.35}CoSb_{0.8}Sn_{0.2}/Ca_3Co_4O_9$," 2013.

[204] D. G. Zhao, X. Y. Li, Y. H. Cai, W. Jiang, and L. D. Chen, "Fabrication and Evaluation of $CoSb_3$/Electrode Thermoelectric Joints," *Mater. Sci. Forum*, vol. 631–632, pp. 313–318, 2009.

[205] W. Brostow, T. Datashvili, H. E. Hagg Lobland, T. Hilbig, L. Su, C. Vinado, and J. White, "Bismuth telluride-based thermoelectric materials: Coatings as protection against thermal cycling effects," *J. Mater. Res.*, pp. 1–

7, 2012.

[206] M. Kambe, T. Jinushi, and Z. Ishijima, “Encapsulated Thermoelectric Modules for Advanced Thermoelectric Systems,” vol. 43, no. 6, pp. 1959–1965, 2014.

[207] M. Zebarjadi, K. Esfarjani, M. S. Dresselhaus, Z. F. Ren, and G. Chen, “Perspectives on thermoelectrics: from fundamentals to device applications,” *Energy Environ. Sci.*, vol. 5, no. 1, p. 5147, 2012.

[208] J. J. Shen, S. N. Zhang, S. H. Yang, Z. Z. Yin, T. J. Zhu, and X. B. Zhao, “Thermoelectric and thermomechanical properties of the hot pressed polycrystalline Bi0.5Sb1.5Te3 alloys,” *J. Alloys Compd.*, vol. 509, no. 1, pp. 161–164, 2011.

[209] T. S. Kim and B. S. Chun, “Microstructure and thermoelectric properties of n- and p-type Bi2Te3 alloys by rapid solidification processes,” *J. Alloys Compd.*, vol. 437, no. 1–2, pp. 225–230, 2007.

[210] E. Maciá, *Thermoelectric Materials: Advances and Applications*. Pan Stanford, 2015.

[211] J. J. D’Angelo, E. J. Timm, F. Ren, B. D. Hall, E. Case, H. Schock, M. Kanatzidis, D. Y. Chung, and T. P. Hogan, “Electrical Contact Fabrication and Measurements of Metals and Alloys to Thermoelectric Materials,” *MRS Online Proc. Libr.*, vol. 1044, p. null–null, 2007.

[212] P. H. Ngan, N. Van Nong, L. T. Hung, B. Balke, L. Han, E. M. J. Hedegaard, S. Linderoth, and N. Pryds, “On the challenges of reducing contact resistances in half-Heusler alloys-based thermoelectric generators,” *Submitt. to J. Electron. Mater.*, 2015.

[213] Y. Kraftmakher, “Thermal expansion of metals.”

[214] F. C. Nix and D. MacNair, “The thermal expansion of pure metals: copper, gold, aluminum, nickel, and iron,” *Phys. Rev.*, vol. 60, no. 8, p. 597, 1941.

[215] H. Shinsuke, N. Takayuki, and O. Masami, “Thermoelectric conversion module, heat exchanger using same, and thermoelectric power generating system,” EP 1 835 551 A1, 2004.

[216] Y. C. Lan, D. Z. Wang, G. Chen, and Z. F. Ren, “Diffusion of nickel and tin in p -type (Bi,Sb)2Te3 and n -type Bi2(Sb,Te)3 thermoelectric materials,” *Appl. Phys. Lett.*, vol. 92, no. 101910, pp. 10–12, 2008.

[217] K. T. Wojciechowski, R. Zybala, J. Leszczynski, P. Nieroda, M. Schmidt, R. Gajerski, and E. Aleksandrova, “Performance characterization of high-efficiency segmented Bi2Te3/CoSb3 unicouples for thermoelectric generators,” vol. 467, no. 2012, pp. 467–470, 2012.

[218] W. P. Lin, P. J. Wang, and C. C. Lee, “Bonding / Barrier Layers on Bismuth Telluride (Bi2Te3) for High Temperature Applications,” in *Electronic components and technology conference*, 2010, pp. 447–450.

[219] C. Valette, M. F. Devismes, R. Voytovych, and N. Eustathopoulos, “Interfacial reactions in alumina/CuAgTi braze/CuNi system,” *Scr. Mater.*, vol. 52, no. 1, pp. 1–6, 2005.

[220] T. Y. Lin, C. N. Liao, and A. T. Wu, “Evaluation of Diffusion Barrier Between Lead-Free Solder Systems and Thermoelectric Materials,” *J. Electron. Mater.*, vol. 41, no. 1, pp. 153–158, 2012.

[221] N. V. Nong, L. T. Hung, L. Han, P. H. Ngan, and N. Pryds, “Characterization of the contact between Bi2Te3-based materials and lead-free solder alloy under thermal cycling,” in *34th Annual International Conference on Thermoelectrics and 13th European conference on Thermoelectrics*, 2015, p. 15C.5.

[222] S. Kasap, “Thermoelectric effects in metals : Thermocouples,” in *Thermoelectric effects in metals: Thermocouple*, 2001, pp. 1–11.

[223] P. Fiflis, L. Kirsch, D. Andruczyk, D. Curreli, and D. N. Ruzic, “Seebeck coefficient measurements on Li, Sn, Ta, Mo, and W,” *J. Nucl. Mater.*, vol. 438, no. 1–3, pp. 224–227, 2013.

[224] Q. Zhang, B. Liao, Y. Lan, K. Lukas, W. Liu, K. Esfarjani, C. Opeil, D. Broido, G. Chen, and Z. Ren, “High thermoelectric performance by resonant dopant indium in nanostructured SnTe.,” *Proc. Natl. Acad. Sci. U. S. A.*, vol.

110, no. 33, pp. 13261–6, 2013.

[225] O. Yamashita, “Effect of metal electrode on Seebeck coefficient of p- and n-type,” vol. 178, 2004.

[226] W. A. Harrison, *Electronic Structure and the Properties of Solids: The Physics of the Chemical Bond*. Dover Publications, 2012.

[227] C. Kittel, *Introduction to Solid State Physics*. Wiley, 2004.

[228] J. Holzl and F. K. Schulte, “Work function of metals,” in *Solid surface physics*, 1979.

[229] D. Haneman, “Adsorption and bonding properties of cleavage surfaces of bismuth telluride,” *Phys. Rev.*, vol. 119, no. 2, pp. 567–569, 1960.

[230] Y. Apertet, H. Ouerdane, and C. Goupil, “Equivalent parameters for series thermoelectrics,” pp. 1–7, 2015.

[231] J. De Boor, C. Gloanec, H. Kolb, R. Sottong, P. Ziolkowski, and E. Müller, “Fabrication and Characterization of Nickel Contacts for Magnesium Silicide Based Thermoelectric Generators,” *J. Alloys Compd.*, vol. 632, pp. 348–353, 2015.

[232] H. S. Kim, “Design of thermoelectric (TE) modules based on TE materials of higher specific figure-of-merit and low-cost materials,” University of Washington, 2013.

[233] O. D. Iyore, T. H. Lee, R. P. Gupta, J. B. White, H. N. Alshareef, M. J. Kim, and B. E. Gnade, “Interface characterization of nickel contacts to bulk bismuth tellurium selenide,” *Surf. Interface Anal.*, vol. 41, no. 5, pp. 440–444, May 2009.

[234] W. P. Lin, D. E. Wesolowski, and C. C. Lee, “Barrier/bonding layers on bismuth telluride (Bi2Te3) for high temperature thermoelectric modules,” *J. Mater. Sci. Mater. Electron.*, vol. 22, no. 9, pp. 1313–1320, 2011.